Diss. ETH No. 12676

A Measurement of the Beauty and Charm Production Cross Sections at the ep Collider HERA

A dissertation submitted to the
Swiss Federal Institute of Technology Zurich
for the degree of
Doctor of Natural Sciences

presented by
Urs Langenegger
dipl. phys. ETH
born May 14, 1968
citizen of Bühler (AR)

accepted on the recommendation of
Prof. Dr. R. A. Eichler, examiner
Prof. Dr. F. Pauss, co-examiner

April 1998

A Measurement of the Beauty and Charm Production Cross Sections at the ep Collider HERA

A dissertation submitted to the
Swiss Federal Institute of Technology Zurich
for the degree of
Doctor of Natural Sciences

presented by
Urs Langenegger
dipl. phys. ETH
born May 14, 1968
citizen of Bühler (AR)

accepted on the recommendation of
Prof. Dr. R. A. Eichler, examiner
Prof. Dr. F. Pauss, co-examiner

April 1998

Charm is deceptive, and beauty is fleeting.
(Proverbs 31:30, RSV)

Abstract

Heavy flavor production at HERA is dominated by photoproduction, where a quasi-real photon scatters off a gluon in the proton. While open ($D^{*\pm}$) and hidden (J/ψ) charm have been measured since 1994, the first real evidence of hidden beauty (Υ) was seen only in 1997.

The present analysis measures *open* beauty (and charm) photoproduction in the kinematic range $Q^2 < 1\,\mathrm{GeV}^2$ and $0.1 < y_{JB} < 0.8$ and uses data taken with the H1 detector in the years 1995 – 1996, corresponding to an integrated luminosity of $\mathcal{L} = 8.31\,\mathrm{pb}^{-1}$.

The beauty contribution in the event sample is enhanced by requiring at least two jets with $E_T > 6\,\mathrm{GeV}$ and at least one muon in the central region of the detector with a transverse momentum $p^{\mu}_{\perp} > 2\,\mathrm{GeV}/c$. The muon has to be found within one of the jets. Beauty and charm events are separated on a statistical basis using the transverse momentum of the muon $p^{\mu}_{\perp,rel}$ relative to its jet axis. The measured $p^{\mu}_{\perp,rel}$ distribution is fitted with a beauty and charm component in addition to a background from light quarks. The shapes of the b- and c-contributions are obtained from the AROMA 2.2 Monte Carlo simulation. The normalization and shape of the background is extracted directly from data using a detailed parameterization of the muon misidentification probability.

The visible open beauty and charm production cross sections are measured in the kinematic range ($Q^2 < 1\,\mathrm{GeV}^2,\ 0.1 < \mathrm{y_{JB}} < 0.8,\ \mathrm{p}^{\mu}_{\perp} > 2\,\mathrm{GeV}/c,\ 35^\circ < \theta^{\mu} < 130^\circ$) to be

$$\sigma_{vis}(ep \to b\bar{b}X) = 0.93 \pm 0.08\,^{+0.21}_{-0.12}\,\mathrm{nb}$$
$$\sigma_{vis}(ep \to c\bar{c}X) = 1.20 \pm 0.23\,^{+0.30}_{-0.38}\,\mathrm{nb},$$

where the first uncertainty is statistical and the second systematic.

The visible beauty cross section is significantly higher than the expectation of a leading-order QCD event generator with parton showers (AROMA 2.2), which amounts to $\sigma^{MC}_{vis}(ep \to b\bar{b}X) = 0.19\,\mathrm{nb}$. The visible charm cross section agrees well with the prediction of AROMA 2.2. An extrapolation of the visible charm cross section to the full kinematic range results in a total charm production cross section consistent with a measurement based on the reconstruction of $D^{*\pm}$ mesons.

Zusammenfassung

Bei HERA findet die Produktion schwerer Quarks vor allem in der Photoproduktion statt, bei der ein quasi-reelles Photon an einem Gluon im Proton gestreut wird. Während offener Charm ($D^{*\pm}$) und verborgener Charm (J/ψ) schon seit 1994 gemessen werden, sah man die ersten überzeugenden Anzeichen für verborgene Beauty (Υ) erst 1997.

Die vorliegende Arbeit misst die Photoproduktion von offener Beauty (und Charm) im kinematischen Bereich $Q^2 < 1\,\mathrm{GeV}^2$ and $0.1 < y_{JB} < 0.8$, wobei Daten benutzt werden, die 1995 – 1996 vom H1 Detektor gemessen wurden und einer integrierten Luminosität von $\mathcal{L} = 8.31\,\mathrm{pb}^{-1}$ entsprechen.

Der Beauty-Anteil in der Datenmenge wird erhöht, indem (mindestens) zwei Jets mit $E_T > 6\,\mathrm{GeV}$ und (mindestens) ein Myon im zentralen Bereich des Detektors mit einem Transversalimpuls von $p^{\mu}_{\perp} > 2\,\mathrm{GeV}/c$ verlangt werden. Das Myon muss dabei Teil eines Jets sein. Beauty und Charm Ereignisse werden mit Hilfe des Transversalimpulses $p^{\mu}_{\perp,rel}$ des Myons relativ zu seiner Jetachse getrennt. Die gemessene $p^{\mu}_{\perp,rel}$ Verteilung wird mit Komponenten von Beauty und Charm sowie leichten Quarks angepasst. Die Form der b- und c-Verteilung wird aus der AROMA 2.2 Monte Carlo Simulation gewonnen. Der Untergrund wird mit Hilfe einer detaillierten Parametrisierung der Muon-Falschidentifikation direkt aus den Daten gewonnen.

Der sichtbare Produktions-Wirkungsquerschnitt für Beauty und Charm ist im kinematischen Bereich ($Q^2 < 1\,\mathrm{GeV}^2,\ 0.1 < \mathrm{y_{JB}} < 0.8,\ \mathrm{p}^{\mu}_{\perp} > 2\,\mathrm{GeV}/c,\ 35^\circ < \theta^{\mu} < 130^\circ$):

$$\sigma_{vis}(ep \to b\bar{b}X) = 0.93 \pm 0.08\,^{+0.21}_{-0.12}\,\mathrm{nb}$$
$$\sigma_{vis}(ep \to c\bar{c}X) = 1.20 \pm 0.23\,^{+0.30}_{-0.38}\,\mathrm{nb},$$

wobei die erste Unsicherheit statistisch und die zweite systematisch ist.

Der sichtbare Beauty Wirkungsquerschnitt ist signifikant grösser als die Erwartung des Ereignisgenerators AROMA 2.2, der auf einer Rechnung in führender Ordnung sowie Partonen-Schauern beruht. Dessen Vorhersage beträgt $\sigma^{MC}_{vis}(ep \to b\bar{b}X) = 0.19\,\mathrm{nb}$. Der sichtbare Charm Wirkungsquerschnitt stimmt gut mit der Vorhersage von AROMA 2.2 überein. Eine Extrapolation des sichtbaren Charm-Wirkungsquerschnittes auf den gesamten kinematischen Bereich führt zu einem totalen Charm Wirkungsquerschnitt, der konsistent ist mit den Werten, die mit der Rekonstruktion von $D^{*\pm}$ Mesonen gemessen wurden.

Table of Contents

Introduction **1**

1 Experimental Setup **3**
1.1 The HERA Collider 3
1.2 The H1 Detector 4

2 Photoproduction of Charm and Beauty **10**
2.1 Kinematics of Electron Proton Scattering 10
2.2 Weizsäcker-Williams Approximation 12
2.3 Heavy Quark Production 13
2.4 Fragmentation of Heavy Quarks 17
2.5 Semi-leptonic Decays of Heavy Quarks 19
2.6 Event Generators and MC Simulations 20

3 Muon Identification in the Barrel **23**
3.1 The Instrumented Iron Return Yoke 23
3.2 Track Reconstruction in the Instrumented Iron Return Yoke 26
3.3 Muon Track Linking 29
3.4 Background in the Muon Sample: Sources and Strategies 30
3.5 Rejection of Cosmic Muons 33
3.6 Improved Muon Identification in the Barrel 34
3.7 Parameterized Fake Muon Estimation with $P_h^\mu(p,\theta)$ 40
3.8 Comparison of P_π^μ in Data and MC Simulation 44
3.9 Fake Muons in Pure Pion and Kaon Samples 47
3.10 Estimation of Fake Muons in a General Hadron Sample 49

4 Data Selection **53**
4.1 Track Selection 53
4.2 Energy Measurement in the Calorimeters 57
4.3 Jet Reconstruction 59
4.4 Trigger Efficiencies 62
4.5 Luminosity 71
4.6 Event Selection 73

5 Measurement of $\sigma_{ep}^{c\bar{c}X}$ and $\sigma_{ep}^{b\bar{b}X}$ **76**
5.1 Separation of Beauty and Charm from Background 76
5.2 Visible Beauty and Charm Cross Section 82
5.3 Extrapolation to the Full Kinematic Range 84
5.4 Systematic Uncertainties 85

Summary and Outlook **87**

A1 Receiver Boards of the DC-$r\phi$ Trigger **88**
A1.1 The Hardware of the New Receiver Boards 89
A1.2 Controlling the Receivers 94
A1.3 Test-Pattern Runs and Self-Tests 97

Bibliography **102**

Acknowledgments **105**

Curriculum Vitae **106**

Introduction

The world's first and — up to now — only electron-proton collider HERA provides an excellent environment to study heavy quark production. The electron* beam can be considered as a source of quasi-real photons. Colliding electrons with an energy of 27.5 GeV onto protons with 820 GeV results in an average energy in the photon-proton center-of-mass system (cms) of $W_{\gamma p} \sim 200\,\mathrm{GeV}$. This is roughly an order of magnitude higher than at previous fixed target experiments.

The total photon-proton cross section amounts to $\sigma_{\gamma p}^{tot} = 165\,\mu\mathrm{b}$ (H1, 1995) and is dominated by 'soft' interactions, where the final state particles emerge with small transverse momenta. It is well described by phenomenological models (*e.g.* VDM), which do not make assumptions about the underlying partonic structure of the process.

Heavy quarks are produced in 'hard' processes, which can be described as interactions of partons. The energy in the partonic cms must be above twice the mass of the quark. This threshold serves as an infrared cutoff and provides a scale enabling perturbative QCD (pQCD) calculations of the process. The charm production cross section has been measured to be $\sigma_{\gamma p}^{c\bar{c}X} = 13.2\,\mu\mathrm{b}$ (H1, 1996), which is roughly 10% of the total cross section. The predictions of pQCD are in reasonable agreement with the data, both in absolute normalization and in the description of the shape of differential distributions. There is some room for tuning the calculations due to uncertainties in the mass of the charm quark, the choice of the renormalization and factorization scales, and the choice of the parton density functions in the proton and the photon.

In this analysis the beauty production cross section is measured. Next-to-leading order QCD calculations (Frixione *et al.*, 1994) predict it to be $\sigma_{\gamma p}^{b\bar{b}X} \sim 60\,\mathrm{nb}$, which is roughly 200 times smaller than the cross section for charm production. In combination with experimental efficiencies, this inhibits a reconstruction of a full decay chain of a meson containing a b-quark. In order to have the largest acceptance possible, this analysis employs the semi-leptonic decay channels of heavy quarks. The decay leptons typically have rather low momenta, which makes an analysis based on muons rather than on electrons and positrons preferable, as the background due to misidentified hadrons is smaller and better understood.

* During 1992 – 1994, HERA was operated with electrons in the lepton beam; since 1994 positrons are used. In the following, 'electron' will be used as a generic name for both.

Due to the large mass and hard fragmentation of the beauty quark, muons from semi-leptonic b-decays have larger momentum and larger transverse momentum with respect to the quark's direction than muons from semi-leptonic c-decays. This difference can be exploited to disentangle the measured distributions into the components due to c- and b-quarks. The quark direction is approximated with the jet axis and the transverse momentum of the muon relative to that direction is measured in the data. Monte Carlo (MC) simulations provide predictions about the shape of the distributions from c- and b-decays. The data distribution is fitted with these components resulting in the relative fractions of the components. These fractions lead to the number of muons due to c- and b-quarks, which can be converted into a cross section.

Two points have to be observed in order that this method works. The individual components should provide roughly the same amount of statistics. With one component overwhelmingly dominating the sample, the fit cannot provide an accurate disentanglement.

In addition to genuine muons from heavy quark decays, there will also be contributions from background, including hadrons traversing the detector as minimum ionizing particles, and in-flight decay of hadrons into muons. This background is extracted from data and only very basic input from Monte Carlo simulations is used: the probability that a hadron is measured as a muon. With this probability it is possible to make an estimate for the contribution from hadrons to the muon sample both in shape and in absolute normalization. Keeping this background fixed allows a two parameter fit of the data with the components of charm and beauty quarks only.

Measuring the heavy quark production cross sections with the transverse momentum of muons relative to a jet axis has never before been done at HERA. It is nevertheless a well-proven technique to tag $b\bar{b}$-events both at electron-positron machines (ALEPH, 1994; L3, 1990; and OPAL, 1991) and at hadron-hadron colliders. The first measurement of the beauty production cross section along these lines at the CERN $\bar{p}p$ collider at $\sqrt{s} = 630\,\text{GeV}$ was published in (UA1, 1988). At the Tevatron, DØ has done a similar analysis both at energies of $\sqrt{s} = 630\,\text{GeV}$ (DØ, 1997) and of $\sqrt{s} = 1.8\,\text{TeV}$ (DØ, 1995). CDF has published an analysis based on electrons (CDF, 1993). Comparisons with the prediction of a next-to-leading order pQCD calculation show a remarkable feature: The shapes of the measured distributions are well described, but the absolute normalization is not well predicted. All three experiments show a significant excess of the measured over the predicted cross sections. UA1 is at the lower end with a cross section ratio (Data/Theory) ~ 2, while some of the measurements at CDF and DØ take this ratio up to ~ 4. Extreme choices have to be taken for both renormalization and factorization scales for a reasonable prediction of the normalization.

Chapter 1

Experimental Setup

1.1 The HERA Collider

HERA, the 'Hadron-Elektron Ring Anlage', is the first electron-proton collider in the world and is shown in figure 1. It is located in Hamburg (Germany) and operated by DESY. After a construction time of eight years, data taking began in 1992. Two independent accelerators were designed to store 820 GeV protons and 30 GeV electrons. The limiting factors for the proton energy are the magnets, while synchrotron

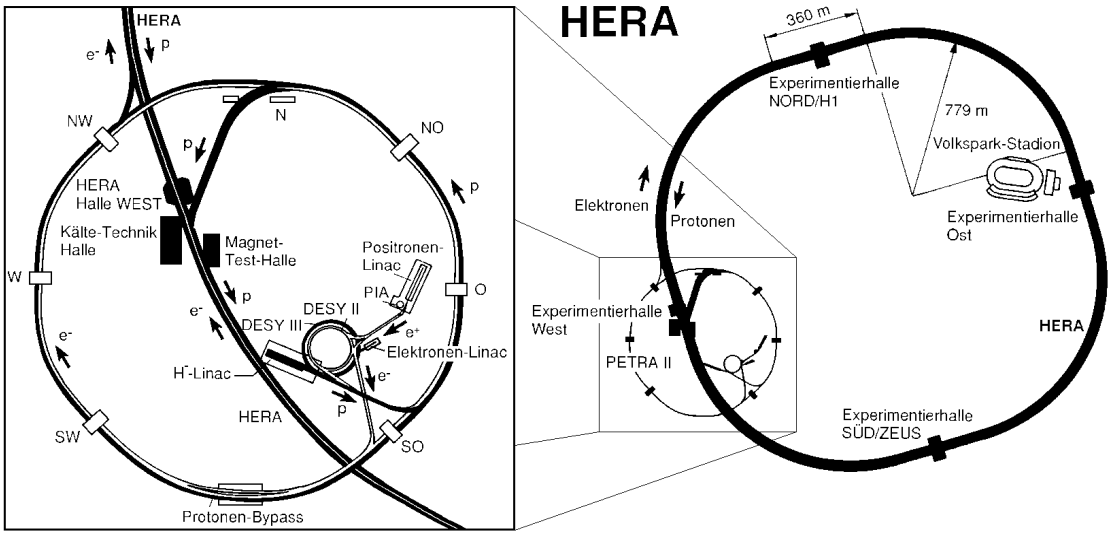

Figure 1: Layout of the electron-proton collider HERA with the injectors PETRA and DESY.

radiation constrains the electron energy. HERA uses some of the older accelerators at DESY as injectors for the proton and the electron beam. These machines preaccelerate the electrons to 14 GeV and the protons to 40 GeV. The beams are then injected into HERA and further accelerated and stored. The two counter-rotating beams are brought to collision at two interaction points spaced uniformly around its 6.3 km circumference. Two general-purpose experiments, H1 and ZEUS, are located around these interaction regions. Two further experimental sites are occupied by HERMES and HERA-B.

In order to maximize the luminosity, up to 210 bunches of protons and electrons can be stored in each beam. The time interval between two consecutive bunch crossings is 96 ns. The length of the electron bunch is $\sigma_e \sim 1$ cm and of the proton bunch $\sigma_p \sim 21$ cm. The vacuum in the beam-pipe is typically $\sim 10^{-9}$ mbar. Table 1 shows some of the design parameters of HERA.

Table 1: Summary of some HERA design parameters. Currently the electrons have an energy of 27.5 GeV yielding a cms energy of $\sqrt{s} = 300$ GeV. The currents reach roughly 60% of the values quoted in this table.

Parameter	electron ring		proton ring
Circumference		6336 m	
Luminosity		$1.5 \cdot 10^{31}\,\mathrm{cm}^{-2}\,\mathrm{s}^{-1}$	
Energy	30 GeV		820 GeV
cms energy for ep		314 GeV	
cms energy for γp		60 GeV – 280 GeV	
σ_x, σ_y at interaction point	0.26, 0.02 mm		0.29, 0.07 mm
σ_z at interaction point	8 mm		110 mm
Number of particles/beam	$0.8 \cdot 10^{13}$		$2.1 \cdot 10^{13}$
Number of bunches	210		210
Circulating currents	60 mA		160 mA
Injection energy	14 GeV		40 GeV
Energy loss per turn	127 MeV		6.2 eV
Magnetic bending field	0.164 T		4.682 T

1.2 The H1 Detector

As the electrons and protons have different momenta, the cms in an ep-collision moves relative to the laboratory frame with $\gamma_{cms} = 2.86$. This motivated the construction of

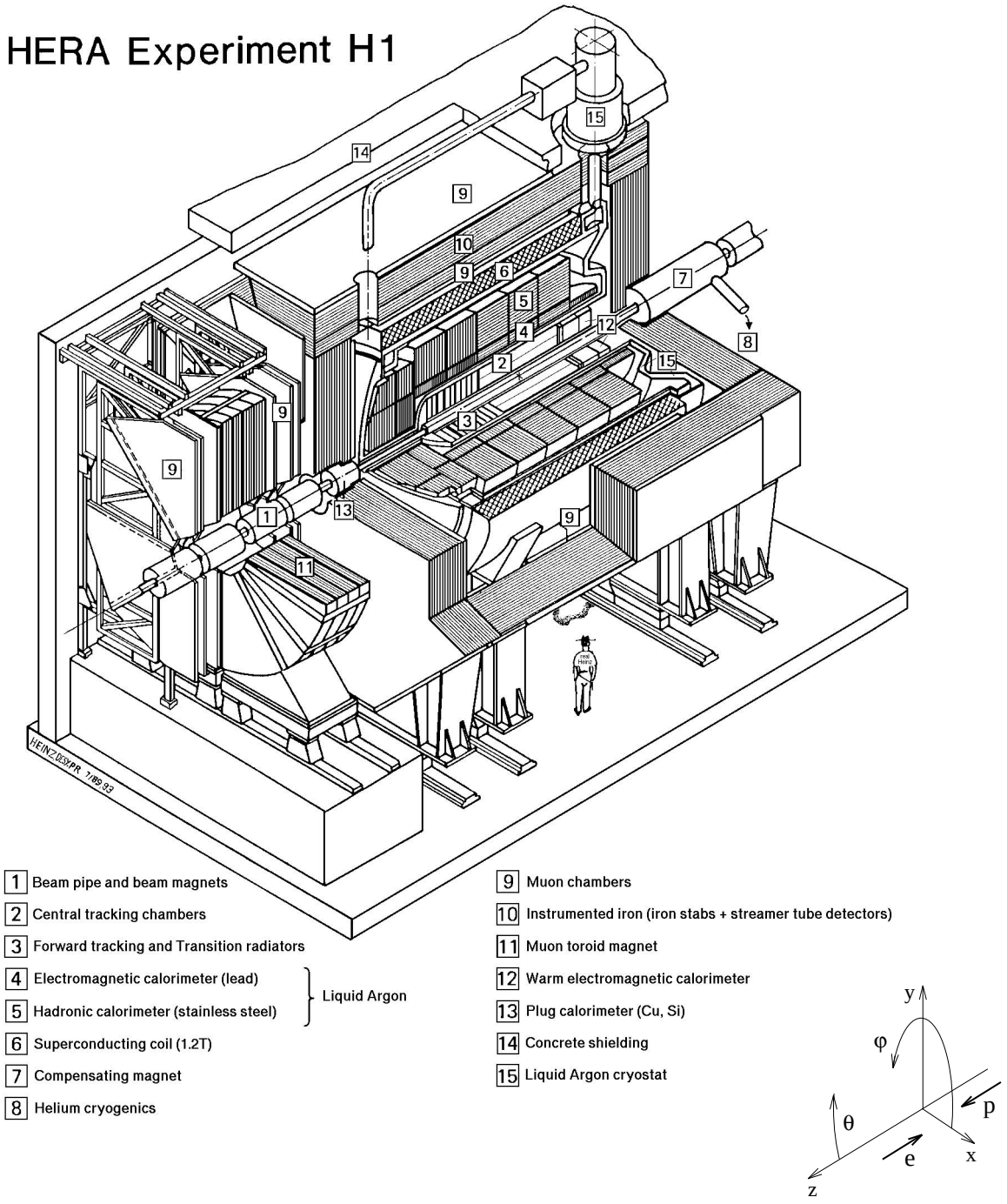

Figure 2: The H1 detector. The protons enter from the right, the electrons from the left. The main detector components are explained in the text, the co-ordinate system used in H1 is indicated in the lower right corner.

an asymmetric detector, which is considerably more massive and better instrumented in the direction of flight of the proton. The H1 detector is shown in figure 2.

The co-ordinate system of H1 has the z-axis in the direction of the proton beam. Perpendicular to it, facing upwards, is the y-axis. The x-axis complements the first two axes to a right-handed co-ordinate system. Due to the azimuthal symmetry, the xy-plane is rarely used. Instead, the radius r and the azimuth angle ϕ (with respect to the x-axis) are used as co-ordinates. The direction of flight of the proton is called the *forward* direction, while the unscattered electrons leave the detector in the *backward* direction. The latter corresponds to a polar angle of $\theta = 180°$.

In the following, a short description of the detector components used for this analysis is provided. The full information can be found in (H1, 1995a) and references given therein.

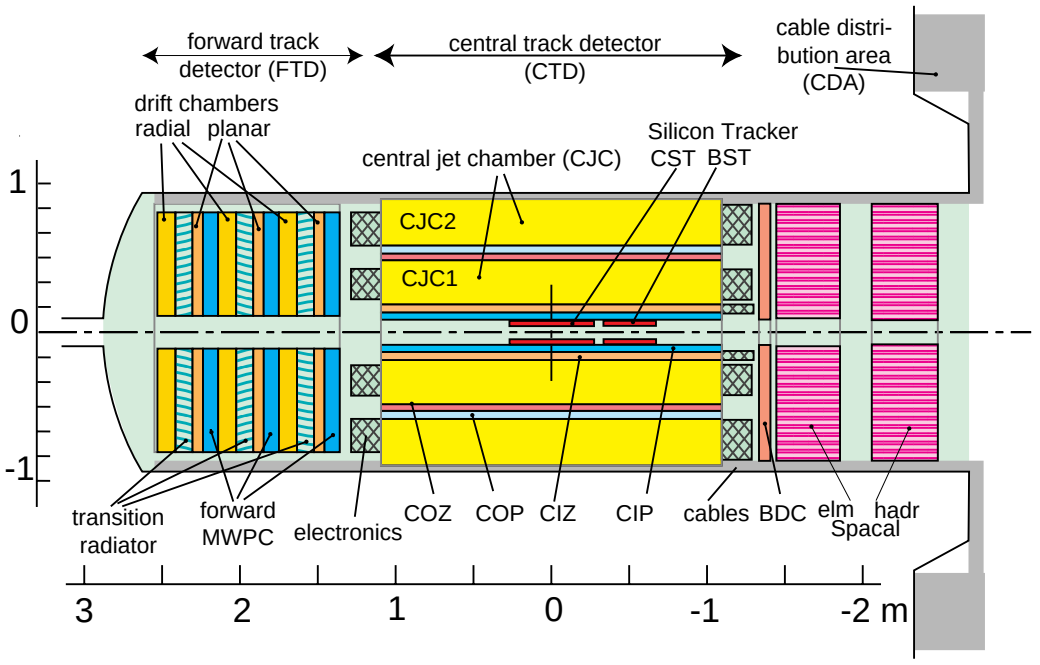

Figure 3: The tracking system of H1 as seen in the rz-projection.

Tracking

The tracking system of H1 provides simultaneous track triggering, reconstruction and particle identification and is shown in figure 3. It consists of central, forward, and backward track detectors, each containing several layers of drift chambers and multi-wire proportional chambers.

Track reconstruction in the central part is accomplished by two large concentric *central jet chambers, CJC1* and *CJC2*. These drift chambers have a very good resolution in the $r\phi$-plane: $\sigma_{r\phi} \approx 170\,\mu$m, while the resolution in z is one percent of the wire length, *i.e.* $\sigma_z \approx 2.2\,$cm. The double track resolution is $\sim 2\,$mm.

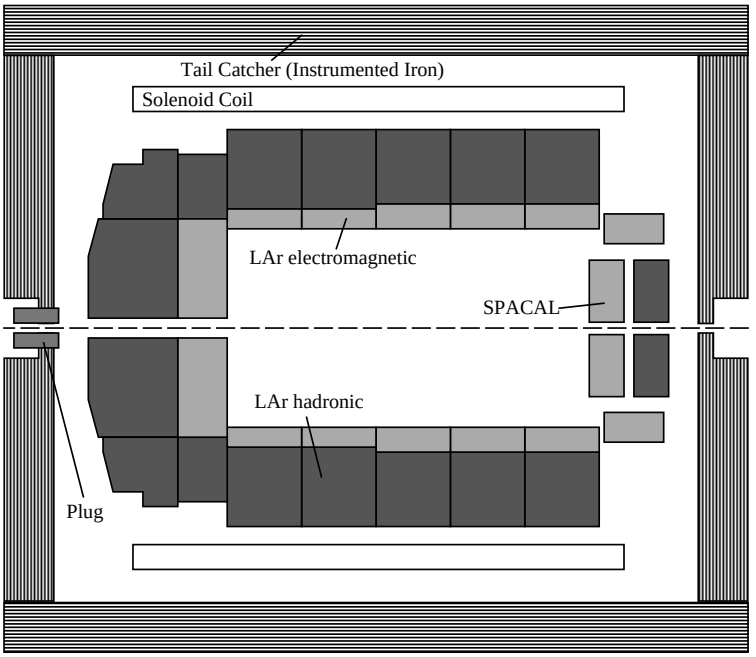

Figure 4: Schematic view of the calorimeters in the rz-plane.

In order to improve the resolution in z, two thin drift chambers, the *central inner (CIZ)* and the *central outer (COZ) z-chambers*, complement the measurement of charged tracks. The CIZ chamber fits inside CJC1, and the COZ chamber is placed between CJC1 and CJC2. Their intrinsic resolution in z is $\sigma_z \approx 300\,\mu$m, while $\sim 2\%$ of 2π in ϕ. In order to achieve this resolution in z, the wires are strung perpendicular to the beam axis and consequently a drift direction along z results. Linking track elements obtained from the jet chambers CJC1 and CJC2 with those from CIZ and COZ gives a good accuracy for the determination of the longitudinal and transverse momentum components.

The backward region of H1 is covered by the *Backward Drift Chamber (BDC)*, which is an essential device for the measurement of electrons scattered at angles of $153^\circ < \theta < 177.5^\circ$.

The *Forward Track Detector (FTD)* covers the range $5^\circ < \theta < 20^\circ$ and is built of three identical super-modules. Each consists of drift and proportional chambers, complemented by a transition radiation detector.

Calorimetry

The *liquid argon (LAr) calorimeter* surrounds the trackers and houses lead absorber plates in the electro-magnetic section and steel absorber plates in the hadronic section. It is highly segmented and features 30784 (13568) cells in the electro-magnetic (hadronic) part. The LAr calorimeter is non-compensating, *i.e.* signals from electrons are on average higher than those from pions at the same energy. The high segmentation

allows the differentiation between electro-magnetic and hadronic shower components and a good reconstruction of the hadronic energy with (off-line) weighting functions. The total thickness of the electro-magnetic calorimeter varies between 20 and 30 radiation lengths X_0. The hadronic part has a depth of $4.5 - 8$ absorption lengths λ_{abs}. The energy resolution in the electro-magnetic part is $12\%/\sqrt{E[\,\mathrm{GeV}]} \oplus 1\%$, the hadronic energy resolution amounts to $50\%/\sqrt{E[\,\mathrm{GeV}]} \oplus 2\%$. The absolute energy scale is known to 3% (4%) for the electro-magnetic (hadronic) part.

Energy flow in the backward direction is measured with a lead/scintillating-fiber calorimeter *Spacal* introduced in the shutdown of 1994/1995. It covers the polar angles of $153^\circ < \theta < 177.8^\circ$ and consists of an electro-magnetic (1192 cells) and a hadronic (136 cells) section. The energy resolutions are $7.5\%/\sqrt{E[\,\mathrm{GeV}]} \oplus 1\%$ and $\sim 30\%$, respectively. The absolute energy scales are known to 0.7% at an electron energy of 27.5 GeV degrading linearly to 3% at $E_e = 7\,\mathrm{GeV}$, while the hadronic scale is known to 7%.

Other Detector Components

Two double scintillator *veto walls* are installed at $z = -6.5\,\mathrm{m}$ and $z = -8.1\,\mathrm{m}$, respectively. They are used to identify out of time background particles produced by the proton beam upstream of the H1 detector. Two *time of flight (TOF) devices* are located in the forward direction at $z = 7.9\,\mathrm{m}$ and in the backward direction at $z = -2\,\mathrm{m}$, allowing the rejection of events which are out of time.

A cylindrical super-conducting *coil* with a diameter of 6 m and a length of 5.75 m provides a magnetic field of 1.15 T in the direction of the z-axis. The effect of the magnetic field on the beam is compensated by a small super-conducting coil with its center at $z = -4.4$ m. The 1.8 m long coil provides a longitudinal field integral $\int B_z\,dz$ equal and opposite in sign to that of the main magnet.

The *instrumented iron return yoke* of the magnet is divided into three different zones: The forward and backward *end-caps* and the central *barrel*. It is made up of 10 laminations, each with a thickness of 7.5 cm. The gaps between these layers are filled with limited streamer tubes, which measure the small fraction of hadronic energy leaking out of the calorimeter ("tail catcher"). In addition, penetrating particles (*e.g.* muons) are measured with the tracks reconstructed in the streamer tubes.

Two detector components (nearly) close the solid angle in the forward direction. Muon detection is done with the *forward muon detector* with its own toroidal magnet. Energy flow at $0.6^\circ < \theta < 6^\circ$ is measured with a silicon-copper *Plug* calorimeter.

The luminosity is determined from the rate of Bethe-Heitler events $ep \to ep\gamma$ by detecting the scattered electron and outgoing photon in coincidence with two components: An *electron tagger* and a *photon detector (PD)* located at $z = -33$ m (ET33) and $z = -105$ m, respectively. In the shutdown of 1994/95, a second electron tagger was installed at $z = -44\,\mathrm{m}$ (ET44) allowing the detection of electrons under even smaller angles.

Trigger

A trigger is a device for selecting interesting events (passing some predefined criteria) out of the large set of interactions taking place within the detector. H1 uses a multi-level trigger concept to cope with the high bunch-crossing frequency. Each level is only started when the previous level accepted the event.

The *first level (L1) trigger* creates logical combinations *(subtriggers)* of the trigger signals (*trigger elements)* provided by the subsystem triggers of various detector components. L1 is operating dead-time free with an input rate of $\sim 50\,\mathrm{kHz}$ and reaches a decision within $2.5\,\mu\mathrm{s}$. During this time, the entire event information has to be stored in pipelines. It is possible to down-scale *(prescale)* every subtrigger individually in order to adjust to different (background) conditions. The output rate of L1 is roughly $50 - 200\,\mathrm{Hz}$. Once L1 reaches a positive decision, the pipelines are stopped and dead-time (the time during which H1 cannot measure events) starts.

On the second level (L2), the output of L1 is validated by a system based on artificial neural networks and a topological trigger. A decision is reached within $20\,\mu\mathrm{s}$, after which either the readout of the event is started or the pipelines are re-enabled.

The third level trigger (L3) was planned to provide a refined decision during the readout of the event (within $\lesssim 1\,\mathrm{ms}$). It has not yet been implemented.

After an event has been accepted on L2, the full event information is read out and the *L4 filter farm*, consisting of ca. 30 processor boards, starts a preliminary reconstruction of the event. The input rate into L4 is limited by the bandwidth available for the detector readout and the computing power on the processor boards. It is usually below $50\,\mathrm{Hz}$. On L4, the trigger conditions for the L1 subtriggers are verified, background is rejected with dedicated finders, and some special physics classes are selected. In addition to all accepted events, 1% of the rejected events are written to tape for monitoring purposes.

The final trigger level works off-line and consists of the *L5 reconstruction*, where calibration and correction constants are applied to the data. The events are preselected and sorted into physics classes according to distinct signatures (*e.g.* muon in the final state, missing $p_\perp$, *etc.*). Unclassified events are rejected and end up on special tapes.

Selected Subsystem Triggers

The signals provided by the drift-chambers are used for triggering purposes as well. The *DC-$r\phi$ trigger* finds those tracks in the $r\phi$-plane, which cross the beam line. A total of 10 layers from CJC1 and the inner part of CJC2 are used for the track finding in the trigger. The DC-$r\phi$ trigger provides excellent rejection of background due to synchrotron radiation, beam-wall, and beam-gas events.

The *central inner (CIP)*, *central outer (COP)*, and *forward (FPC)* proportional chambers provide input to the *zVtx-trigger* selecting events with a vertex in the region $z = \pm 50\,\mathrm{cm}$.

Five layers (3, 4, 5, 8, 12) of the instrumented iron return yoke are used in the central muon trigger. Trigger elements in the central barrel are provided if a coincidence of two layers in a single module (*cf.* Section 3.1) is observed.

Chapter 2

Photoproduction of Charm and Beauty

2.1 Kinematics of Electron Proton Scattering

Electron proton scattering can be described at lowest order by the exchange of a single gauge boson, if the interaction is *hard*. A process is termed hard, if it involves a large momentum transfer or if the emerging particles have large transverse momentum. Such a process is sketched in figure 5, where the definitions of

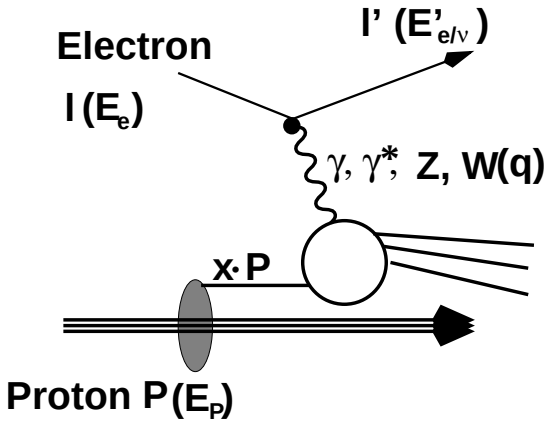

Figure 5: Kinematics of hard electron-proton scattering. An electron with 4-momentum l (energy E_e) is scattered off a proton carrying 4-momentum P by the exchange of a single gauge boson with 4-momentum q.

the particles' momenta are indicated. Three variables are sufficient to completely describe (inelastic) electron proton scattering. A possible set of variables is the cms energy, the scattering angle and energy loss of the electron. At HERA, the electron-proton cms energy is fixed at $\sqrt{s} = 300\,\mathrm{GeV}$ such that only two variables remain. Another pair of

variables, which is more commonly used, is inspired by the naïve quark-parton model: *(i)* Q^2, the negative four-momentum transfer squared of the gauge boson exchanged between the electron and the proton; *(ii)* Bjørken-x, which is — in the infinite momentum frame — the fraction of the proton's momentum carried by the struck quark. The validity of the parton model is discussed in *e.g.* (CTEQ, 1995).

Electron proton scattering can be divided into two classes depending on the value of Q^2. *Deep inelastic scattering* (DIS) is the régime of $Q^2 \gg m_p^2$ and large $W_{\gamma p}$, where $W_{\gamma p}$ is the energy in the photon-proton cms. However, the vast majority of events have small $Q^2 \sim 0$ and are termed *photoproduction*. Here, x_B can no longer be identified with the momentum fraction of the proton carried by the struck parton. This rôle is taken over by x_p. For DIS and photoproduction the exchange of photons is dominant, as the contributions from the heavy gauge bosons Z^0 and $W^\pm$ become appreciable only when $Q^2 \sim M^2_{Z^0,W^\pm}$.

It is useful to extend the description of the process from only two independent variables to a larger set. Table 2 gives an overview of the most commonly used variables, their definition in terms of four-momenta and their expression in directly measurable quantities (the electron and proton masses have been neglected in some of the expressions). The standard set of variables Q^2, s, x, y is not independent but fulfills the following relation:

$$Q^2 = s \cdot y \cdot x.$$

The experimental determination of the kinematic variables given in table 2 depends on the measurement of the electron in the final state. A large fraction of photoproduction is *untagged* in the sense that the electron is not seen in any detector component. It is still possible to determine the event kinematics from the hadronic final state with the method introduced in (Jacquet and Blondel, 1979). It makes use of the energy flow of the hadronic final state without any jet identification or assumptions about the proton structure.

With the four-momentum

$$p^H = \sum_h (E^h, \mathbf{p^h}),$$

where the sum runs over the entire hadronic final state, it follows that

$$y = \frac{P \cdot q}{P \cdot l} = \frac{P \cdot (p^H - P)}{P \cdot l} = \frac{\sum_h (E^h - p_z^h)}{2E_e} \equiv y_{JB}$$

$$Q^2 = \frac{1}{1-y} \sum_h (p_\perp^h)^2$$

Particles contribute with $E^h - p_z = E^h(1 - \cos\theta_h)$ implying that the influence of particles lost in the very forward direction is minimal. On the other hand, if the electron is misidentified and measured in the backward region, a large distortion of the measured quantities results.

Table 2: Variables used in the description of ep scattering. The formulae given in the DIS column contain the full Q^2-dependence, whereas the next column contains the approximation $Q^2 \sim 0$. Masses are neglected in some of the formulae. All energies and angles refer to the lab frame.

Variable	Definition	DIS	Photoproduction	Meaning
$\sqrt{s}$	$\sqrt{(l+P)^2}$	$\sqrt{4E_eE_p}$	$\sqrt{4E_eE_p}$	total cms energy
Q^2	$-(l-l')^2$	$4E_eE'_e\cos^2\frac{\theta_e}{2}$	~ 0	$-$(momentum transfer)^2
y	$\frac{P\cdot q}{P\cdot l}$	$1-\frac{E'_e}{E_e}\sin^2\frac{\theta_e}{2}$	$\sim 1-\frac{E'_e}{E_e}$	Inelasticity
		$=\frac{E_e-E'_e}{E_e}+\frac{Q^2}{2E_e^2}$	$\simeq \frac{E_\gamma}{E_e}$	
x_B	$\frac{Q^2}{2P\cdot q}$	$\frac{E'_eE_e\cos^2\frac{\theta_e}{2}}{E_p(E_e-E'_e\sin^2\frac{\theta_e}{2})}$		Bjørken-x
$W_{\gamma p}$	$\sqrt{(P+q)^2}$	$Q\sqrt{(1-x_B)/x_B}$	$\sim\sqrt{ys}$	hadronic cms energy
x_p	p_{parton}/P			fractional momentum of proton carried by parton
$\sqrt{\hat{s}}$	$\sqrt{(q+x_pP)^2}$	$\sqrt{x_pys-Q^2}$	$\sqrt{x_pys}$	partonic cms energy

Particles in the final state are described by their polar angle θ, azimuthal angle ϕ, and transverse momentum $p_\perp$. In addition, the pseudo-rapidity

$$\eta = -\ln\frac{|\mathbf{p}|+p_z}{|\mathbf{p}|-p_z} = -\ln(\tan\frac{\theta}{2})$$

is used. An advantageous property of η is the invariance of the difference $\Delta\eta = |\eta_1-\eta_2|$ of two particles under a Lorentz-boost along the z-axis.

2.2 Weizsäcker-Williams Approximation

In the *equivalent photon approximation*, an idea originally developed by Fermi (1924), the electro-magnetic field of a fast charged particle is similar to electro-magnetic radiation. This radiation may be interpreted as a flux of quasi-real photons with an energy distribution $f_\gamma^e(E_\gamma)$. It is therefore possible to relate the electron proton cross section σ_{ep} to the photon proton cross section $\sigma_{\gamma p}$ by folding the photon flux with $\sigma_{\gamma p}$:

$$\sigma(ep \to Q\bar{Q}X) = \int f_\gamma^e(y)\sigma(\gamma p \to Q\bar{Q}X)\, dy,$$

where the photon flux is usually calculated in the Weizsäcker-Williams approximation (Weizsäcker, 1934 and Williams, 1934):

$$f_\gamma^e = \frac{\alpha}{2\pi}\left[\frac{1+(1-y)^2}{y}\cdot \ln\frac{Q^2_{max}(y)}{Q^2_{min}(y)} - \frac{2(1-y)}{y}\cdot\left(1-\frac{Q^2_{min}(y)}{Q^2_{max}(y)}\right)\right]. \qquad (1)$$

The photon flux f_γ^e describes the probability at order α that an electron emits a quasi-real transversely polarized photon with energy fraction y. This approximation is valid — in the case of electron-proton scattering — in the domain where $|Q^2| < m_p^2$. For $E_e - E_\gamma \gg m_e$, the photon virtuality varies in the range

$$Q^2_{min}(y) = \frac{y^2 m_e^2}{(1-y)}$$
$$Q^2_{max}(y) = E_e^2 \cdot (1-y) \cdot \theta^2_{max} < 4E_e^2 \cdot (1-y),$$

where Q^2_{min} is the kinematical limit and Q^2_{max} is limited for *tagged* photoproduction by the positions of the electron taggers, given by $\theta_{max} = 5\,\mathrm{mrad}$ (3.5 mrad) for the electron taggers at 33 m (44 m). The flux is described with an accuracy of

$$\Delta f_\gamma^e / f_\gamma^e \sim (Q^2_{max}/m_p^2)\cdot(\ln\frac{Q^2_{max}}{Q^2_{min}})^{-1} \sim 0.1\%$$

for tagged electrons. In the case of untagged photoproduction, where $Q^2 < 1\,\mathrm{GeV}^2$ due to the acceptance of the Spacal, the accuracy degrades to

$$\Delta f_\gamma^e / f_\gamma^e \sim (\ln\frac{m_p^2}{Q^2_{min}})^{-1} \sim 2.9\%,$$

as discussed in detail in (Budnev, *et al.*, 1975).

2.3 Heavy Quark Production

Leading order QCD calculations for heavy quark production cross section were first performed for parton-parton scattering at hadron colliders and have been known since the late seventies. The agreement with the experimentally measured cross sections was poor in particular for the case of charm quarks. This led to a number of attempts to improve the situation with the inclusion of non-perturbative phenomena. Among these were: *(i)* Intrinsic heavy quark components in the hadron wave function, *(ii)* flavor excitation, where the hard scattering graphs include a heavy quark in the initial state, *(iii)* diffractive production of a heavy quark pair, *(iv)* recombination of a produced heavy quark with a *fast* quark from one of the beams, and *(v)* final state prebinding and distortion due to the binding of the heavy quark to a *slow* light quark.

Leading Order Calculations for Hadronic Collisions

All these hypotheses were challenged in (Collins, Soper and Sterman, 1986). Perturbative QCD was claimed to be reliable and the dominant production source for heavy quarks was attributed to the collision of light partons. Furthermore, it was argued that the cross section for heavy quark production in hadron collisions factorizes into a soft and a hard part — as had been shown for (light quark) jet as well as for $W^{\pm}$ and Z^0 production (Ellis, *et al.*, 1979):

$$d\sigma_{h1+h2}^{Q\overline{Q}X}(\sqrt{s}) = \sum_{i,j} \int dx_i\, dx_j\, d\hat{\sigma}_{ij}(x_i, x_j, M, \mu_R, \mu_F, \alpha_s(\mu_R))\, f_i^{h1}(x_i, \mu_F)\, f_j^{h2}(x_j, \mu_F)\,, \tag{2}$$

where
- $\sqrt{s}$ is the energy available in the hadronic cms,
- f_x^y is the parton density function for parton x in hadron y,
- $d\hat{\sigma}_{ij}$ is the (subtracted) partonic short distance scattering cross section,
- x_i is the momentum fraction of the hadron carried by parton i,
- M is the mass of the heavy quark Q,
- μ_R, μ_F are the renormalization and factorization scales, respectively.

Intuitively, factorization is a consequence of the fact that high-energy collisions of composite hadrons can be characterized by two time scales: *(i)* A short time-scale of the order $\min(\frac{1}{p_\perp}, \frac{1}{M})$ characterizing the hard collisions of the constituents, and *(ii)* a long time scale of the order of a typical hadron radius relevant for the binding and recombination of the partons into hadrons.

The subtracted partonic cross section $\hat{\sigma}_{ij}$ is calculable as a power series in the strong coupling constant $\alpha_s(\mu_R)$ and is given in terms of the invariant amplitude by

$$\hat{\sigma}_{ij} \propto \frac{1}{m_{12}^4} \langle \sum_{i,j} |\mathcal{M}_{ij\to Q\bar{Q}}|^2 \rangle,$$

where m_{12} is the invariant mass of the heavy quark pair and $<\ldots>$ denotes the sum over final state colors and spins and the average over initial state colors and spins.

At leading order, $\hat{\sigma}_{ij}$ is calculable and finite over the entire phase space. All mass singularities of the initial state in $\hat{\sigma}_{ij}$ are factorized into the parton density functions (PDF's). The dominating contribution to the total cross section is due to the *boson-gluon fusion* process shown in figure 6. The main conclusions of the leading order calculation are twofold:

- The largest contribution to the cross section stems from the region $|\eta_Q - \eta_{\overline{Q}}| \lesssim 1$, $|\mathbf{k}_Q - \mathbf{k}_{\overline{Q}}| \lesssim m_{12}^2$, where the invariant mass m_{12} of the heavy quark pair is not too much above threshold $m_{12} = 2M$. (η and $\mathbf{k}$ are the pseudo-rapidity and transverse momentum of the produced heavy quarks, respectively.)
- The transverse momenta of the heavy quarks are typically of the order of M and the cross section for the production of heavy quarks with high-$\mathbf{k}$ falls rapidly to zero as $\mathbf{k} \to \infty$.

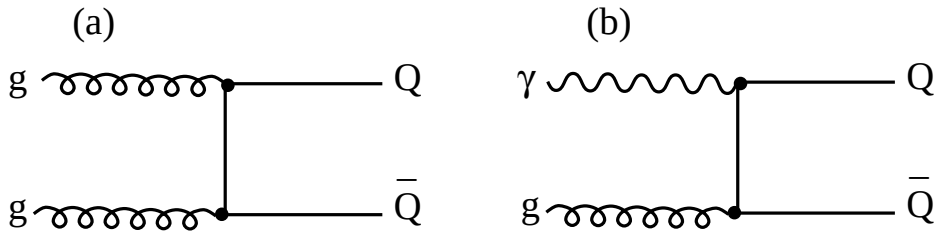

Figure 6: Heavy quark production via boson-gluon fusion. In hadron-hadron collisions the dominant part is due to gluon-gluon fusion shown in (a). The corresponding graph for direct photon-hadron collisions is shown in (b).

Next-to-leading Order Calculations

The first calculations at *next-to-leading* order in QCD for heavy quark production in hadronic collisions were done in (Nason, Dawson, and Ellis, 1988) and by Ellis and Nason (1989) for photoproduction. In hadroproduction, the general effect of the first radiative corrections is to increase the cross section by a constant factor without appreciably changing the shape of *e.g.* η_Q- or $\mathbf{k}_Q$-distributions.

The next-to-leading order corrections are found to be important in two regions:

- Production of heavy quarks at threshold $\hat{s}/4m_Q^2 < 1.1$. The order α_s correction dominates the lowest order ones, which is attributed to terms with large logarithms. These enhancements are due to initial-state gluon bremsstrahlung collinear to a gluon or (outgoing) quark line.
- Large cms energy, *i.e.* $\hat{s} > 200\,\mathrm{GeV}^2$. The cross section behavior shows a plateau as $\hat{s} \to \infty$. This is attributed to gluon exchange in the t-channel of the subprocess $g + Q^* \to g + Q^*$, where Q^* is the virtual heavy quark produced in the process $\gamma \to Q\overline{Q}$.

One of the main motivations for NLO calculations is the hope for a reduced dependence on the renormalization and factorization scales and schemes used. Unfortunately, a significant scale dependence of up to a factor of two of the NLO result remains, indicating large NNLO corrections.

Photoproduction of Heavy Quarks

The situation in photoproduction can be regarded as an extension of the hadroproduction case, as on-shell photons have a finite probability to fluctuate into a hadronic state before interacting with the proton. In addition, the photon can participate as a point-like gauge boson in the hard collision with the proton. Therefore the differential photon-proton cross section can be written as the sum of the direct (point-like) and resolved (hadronic) photon contribution:

$$
\begin{aligned}
d\sigma_{\gamma p}^{Q\overline{Q}X} &= d\sigma_{point}^{\gamma p} + d\sigma_{hadronic}^{\gamma p} \\
&= \sum_i \int dx_i \, f_i^p(x_i, \mu_F) \cdot d\hat{\sigma}_{\gamma i}(p_\gamma, x_i P, \alpha_s(\mu_R), \mu_R, M, \mu_F, \mu_\gamma) \\
&\quad + \sum_{ij} \int dx_i \, dx_j \, f_i^\gamma(x_i, \mu_\gamma) f_j^p(x_j, \mu_F) \cdot d\hat{\sigma}_{ij}(x_i p_\gamma, x_j P, \alpha_s(\mu_R), \mu_R, M, \mu_F, \mu_\gamma),
\end{aligned}
\tag{3}
$$

where, in addition to the quantities introduced for equation (2),

P is the momentum of the proton,
p_γ is the momentum of the photon,
μ_γ is the factorization scale of the electro-magnetic vertex.

Equation (3) contains two additions to equation (2): the parton density function f_i^γ in the photon, and μ_γ, the factorization scale for collinear singularities arising from the electro-magnetic vertex.

At next-to-leading order, the division of photoproduction into a direct and a resolved part is ambiguous and depends on the factorization scale μ_γ. Singularities due to the splitting of the photon into two *massless* partons with a transverse momentum less than $O(\mu_\gamma)$ are absorbed into the photon PDF of the resolved component. Contributions due to the splitting into two partons above a scale of μ_γ are attributed to the direct part. As the choice of the factorization scale (and scheme) is completely arbitrary, neither of the two components alone has any physical meaning. It is only their sum which is observable.

The sum in equation (3) runs over three light flavors only. Heavy quarks are produced exclusively by the scattering of massless partons and all effects of the heavy quark mass are therefore contained in the kernel cross sections. All mass singularities have been factorized from $d\hat{\sigma}$ and contributions by momentum scales below μ_F have been removed.

In order to calculate the cross section, both renormalization against UV and mass divergences as well as factorization against IR divergences (due to real and virtual contributions) are done at the mass scale $\mu = M_Q$. The results are usually obtained in a modified $\overline{MS}$ scheme as follows. Graphs containing a light parton loop are renormalized with the standard $\overline{MS}$ scheme, while heavy quark internal loops are subtracted at zero momentum. For external heavy quark lines, both mass renormalization and the heavy quark field renormalization are equal to zero.

Predictions for the Open b Production Cross Section

There are several predictions of massive calculations for the total $ep \to b\bar{b}X$ cross section available. The first calculation for all $2 \to 2$ and $2 \to 3$ processes in photoproduction — barring virtual corrections — was published in (Ellis and Kunszt, 1986) and integrated for HERA in (Eichler and Kunszt, 1988). The first full next-to-leading order calculation

was given in (Ellis and Nason, 1989) and was cross-checked by Smith and van Neerven (1991). Another calculation based on the work of Ellis and Nason was done by Frixione, *et al.* (1994). The predictions are given in table 3, where the expectancy of the MC event generator Aroma 2.2 (leading order with parton-showers) is given for comparison.

Table 3: Predictions for the total $ep \to b\bar{b}X$ production cross section by several next-to-leading order calculations (the calculation of Eichler and Kunszt does not contain virtual corrections, AROMA is a leading-order calculation with parton-showers). The column denoted 'Scheme' indicates the renormalization scheme used.

Reference	$\sigma_{ep}^{b\bar{b}X}$	μ_F	Scheme	μ_R	M
Eichler and Kunszt (1988)	8.0 nb	$\sqrt{\hat{s}}/2$	–		5.27 GeV/c^2
Ellis and Nason (1989)	4.9 nb	M	$\overline{MS}$	M	5.0 GeV/c^2
	7.1 nb	M	$\overline{MS}$	M	4.5 GeV/c^2
Smith and van Neerven (1991)	6.12 nb	$2M$	$\overline{MS}$	$2M$	4.75 GeV/c^2
	8.77 nb	$M/2$	DIS	$M/2$	4.75 GeV/c^2
Frixione *et al.* (1994)	4.8 nb	M	$\overline{MS}$	M	5.0 GeV/c^2
	9.9 nb	M	$\overline{MS}$	M	4.5 GeV/c^2
AROMA 2.2	3.8 nb	$\sqrt{\hat{s}}$	–		4.75 GeV/c^2

The variation given for Frixione *et al.* is due to different choices of the mass of the b-quark and contains in addition different choices for the PDF's of the proton and the photon. Table 4 provides a detailed overview of the dependence of the open b cross section on various parameters, such as the b-mass, the PDF's, and the factorization and renormalization scales (Frixione, *et al.*, 1994). The sensitivity to scale variations is in beauty production much smaller than for charm production. It should be noted that the uncertainty due to the choice of the PDF is typically smaller than that from scale variation. By far the largest dependence is observed in the variation of the b-mass.

2.4 Fragmentation of Heavy Quarks

The description of heavy quark production provided by perturbative QCD is valid at short distances only. At long distances, the effective coupling gets large and perturbation theory breaks down. In this confinement régime, the colored heavy quarks are

Table 4: Dependence of the open b production cross section [nb] on different parameters. The default parameter settings correspond to $\mu_R = \mu_F = M = 4.75\,\mathrm{GeV}$. (Frixione, *et al.*, 1994)

		μ_R		μ_F		μ_γ		M[GeV]	
	Default	$M/2$	$2M$	$M/2$	$2M$	$M/2$	$2M$	4.5	5.0
Point-like component									
MRSA	4.640	5.332	4.098	4.391	4.773			5.541	3.917
CTEQ2MF	4.814	5.469	4.283	4.554	4.958			5.720	4.079
MRSD-'	4.856	5.580	4.288	4.649	4.963			5.839	4.073
CTEQ2ML	5.123	6.110	4.418	4.728	5.290			6.113	4.325
Hadronic component (with MRSA for the proton PDF)									
GRV-HO	1.115	1.510	0.851	1.077	1.146	1.018	1.177	1.408	0.892
LAC1	2.842	3.947	2.142	2.861	2.840	3.067	2.675	3.792	2.157

transformed into colorless hadrons in a process called *fragmentation*. This process is not yet understood from first principles, but is currently described in several models.

The Lund string fragmentation model (Andersson, *et al.*, 1983), implemented in JETSET 7.4 (Sjöstrand, 1994), assumes that a color flux tube is stretched between two partons, which may be heavy, as they move apart. The energy density along the tube is assumed to be uniform, which automatically leads to a confinement picture with a linearly rising potential. As the potential energy stored in the string increases, the string may break up into a $q\overline{q}$ pair, which may attach to the original partons. If the invariant mass of either of the resulting strings is large enough, further breaks occur. This iterative process continues until only on-mass-shell hadrons (= a small piece of string with a quark and anti-quark at each end) remain.

The fraction z of the original quark's energy transferred to the (heavy) hadron in this process is given by a fragmentation function $f(z)$ which is parameterized using phenomenological models. Standard JETSET settings choose the Lund symmetric fragmentation function

$$f(z) \propto \frac{1}{z}(1-z)^a e^{-bm_\perp^2/z}.$$

This functional form is derived from the requirement that the fragmentation process as a whole should look the same, irrespective of whether the procedure is performed from the quark or the anti-quark end.

Heavy quark fragmentation is often described by the Peterson *et al.* (1983) function

$$f(z) \propto \frac{1}{z(1-\frac{1}{z}-\frac{\epsilon_Q}{1-z})^2},$$

where ϵ_Q is a free parameter expected to scale between flavors like $\epsilon_Q \propto 1/m_Q^2$. This formula can be motivated by observing that the attachment of a light anti-quark $\overline{q}$ to a heavy quark Q — forming a hadron — decelerates Q only slightly. This fragmentation function peaks at $z \sim 1 - 2\epsilon_Q$ with a width of roughly ϵ_Q. The parameters ϵ_Q are determined by fits to data measured at e^+e^- experiments (ARGUS, 1991; OPAL, 1995) and amount in leading-order analyses to

$$\epsilon_c = 0.06,$$
$$\epsilon_b = 0.008.$$

2.5 Semi-leptonic Decays of Heavy Quarks

Hadrons containing a b- or c-quark have typical lifetimes of $\sim 10^{-12}$ s. Roughly 20% of the decays of heavy quarks proceed semi-leptonically into three final-state particles. The semi-leptonic decay amplitude of a meson X into meson Y is described by the product of a leptonic and a hadronic current $< Y|J_\mu|X >< \nu|\gamma_\mu(1-\gamma_5)|\ell >$. Whereas the leptonic current is easily calculable, the hadronic piece requires modeling. The momentum transfer between X and Y, $q^2 \equiv (p_X^\mu - p_Y^\mu)^2$, is given in the rest-frame of X by

$$q^2 = (E_X - E_Y)^2 - (\mathbf{p}_X - \mathbf{p}_Y)^2 = (m_X - E_Y)^2 - \mathbf{p}_Y^2.$$

Maximum q^2 is obtained for $|\mathbf{p}_Y| = 0$, which is called "zero recoil" and corresponds to the back-to-back emission of the lepton and the neutrino. Conversely, $q^2 = 0$ occurs when Y has its maximum possible momentum.

The hadronic current is parameterized in terms of *form factors*, which are Lorentz-invariant functions of the single variable q^2. In the limit of massless leptons (which is a good approximation for electrons and muons), only one form factor $F(q^2)$ is necessary to describe the decay of a pseudo-scalar meson P into another pseudo-scalar meson. For the decay $P \to V\ell\nu$, where V is a vector meson, three form factors are needed.

Various models are used to describe the form factors, see *e.g.* Isgur *et al.* (1989), Wirbel *et al.* (1985), and Korner and Schuler (1988). Another approach is possible in the framework of Heavy Quark Effective Theory (HQET) in the limit of $m_Q \to \infty$. Here all form factors can be expressed in terms of a single form factor, the Isgur-Wise function (Isgur and Wise, 1989).

In both MC event generators used (AROMA 2.2 and HERWIG 5.9), semi-leptonic decays of heavy hadrons are simplified to the point of neglecting form factors altogether. The momenta of the decay products are distributed according to the simple $V - A$ matrix element. All lepton masses are assumed to be negligible, m_τ is accounted for by reducing the branching ratios appropriately.

2.6 Event Generators and MC Simulations

The ultimate judge for any theory remains experiment, against whose measurements the theoretical predictions have to be compared. Theoretical calculations typically provide a description for a limited part (*e.g.* the hard subprocess) of the entire ep interaction, which is measured as a whole in the detector. For a meaningful comparison, either the experimental results have to be transformed to the parton (or hadron) level described by theory, or the theoretical description must be enlarged to encompass the entire event. A possible solution is provided by Monte Carlo (MC) event generators containing a description of the underlying physical processes and a subsequent MC simulation of the detector response. The name (MC) derives from the fact that Monte Carlo techniques are used to select relevant variables (*e.g.* kinematic quantities or resolution parameters) according to the desired probability distributions.

NLO pQCD calculations can be incorporated into *event integrators* (*e.g.* Frixione, *et al.*, 1994a) providing a full next-to-leading order description of the hard subprocess and an exclusive final state where only the fragmented heavy quarks are retained. It is not yet possible to have a full event generated at next-to-leading order.

Event generators currently provide a description of the hard subprocess at leading order and embed this in a phenomenological model of the complete event. The output of such a program consists of the identity and 4-momenta of all particles (leptons and hadrons) involved. At this point, the response of the detector has to be modeled. Here geometrical acceptances, reconstruction efficiencies, *etc.* are simulated. It is only with the information provided in this step that absolute cross sections can be determined. The detector response of the H1 detector is simulated with a program based on the GEANT package (Brun, *et al.*, 1987).

In the following, two event generators used in the analysis are shortly characterized.

Aroma 2.2

The Monte Carlo event generator AROMA 2.2 (Ingelman, Rathsman and Schuler, 1996) simulates the production of heavy quarks through the (direct) boson-gluon fusion process and is based on a leading order calculation of the partonic cross section. The ep cross section for heavy quark production is given by

$$\sigma(e^{\pm}p \to Q\overline{Q}X) = \int dy \int dQ^2 \int dx_g \int dz \int d\phi \, g(x_g, \mu_F^2) \cdot \hat{\sigma}(y, Q^2, x_g, z, \phi), \quad (4)$$

where
- y, Q^2 denote the usual variables for the description of deep-inelastic scattering,
- x_g is the momentum fraction of the proton carried by the gluon (in the infinite-momentum frame),
- $z \equiv \frac{P \cdot p_Q}{P \cdot q}$ is — in the proton rest-frame — the ratio of the energy of the heavy quark and the energy of the photon,
- ϕ is the azimuthal angle around the boson axis between

	the lepton and hadron planes,
$g(x_g, \mu_F^2)$	is the gluon density at a scale μ_F^2,
$\hat{\sigma}(\ldots)$	denotes the pQCD cross section calculated at leading order.

The MC simulation proceeds along the following lines. After generating a phase space point (y, Q^2, x_g, z, ϕ) according to the differential cross section formula in equation (4), the four-momenta of all partons (particles) are calculated. The evaluation of the partonic cross section takes into account the mass of the heavy quark ($m_b = 4.75\,\mathrm{GeV}/c^2$, $m_c = 1.5\,\mathrm{GeV}/c^2$) and the complete electroweak structure for neutral and charged current processes. Both the photoproduction and deep-inelastic regions are covered. Initial state radiation off the incoming gluon is done in the "backward" evolution scheme, where the shower is constructed from the hard interaction backwards with decreasing virtualities down to on-shell partons of the incoming proton. Initial state radiation is calculated with parton showers (Sjöstrand, 1985) at a scale $\min(m_{\perp,Q}^2 + m_{\perp,\overline{Q}}^2, W^2 - \hat{s}, \hat{s} + Q^2/2)$, where $m_\perp = \sqrt{m_Q^2 + p_{\perp,Q}^2}$. The scale μ_F^2 for the determination of the gluon density and α_s is taken to be $\mu_F^2 = \hat{s} = (p_Q + p_{\overline{Q}})^2$. The parton density functions used for this analysis are the leading order parameterizations provided in MRS(G) by Martin, Roberts, and Stirling (1995). The incoming gluon may have a primordial $k_\perp$, which is generated according to a Gaussian distribution with a width of $\sigma = 0.44\,\mathrm{GeV}/c$.

A proper description of the complete event topology requires the incorporation of higher order corrections. Bremsstrahlung off the emerging heavy quarks is simulated with the parton shower algorithm (Bengtsson, *et al.*, 1987) at a scale of $(m_{\perp,Q} + m_{\perp,\overline{Q}})^2$. This provides a description to arbitrarily high orders in α_s, but only in the leading logarithm approximation. From the experience with jets in e^+e^- annihilation, it is expected that this approach describes detailed jet properties (*e.g.* energy flow within jets) better than an exact next-to-leading order calculation.

The emerging multi-parton final state is finally combined with the proton remnant. The three valence quarks of the proton are split into a di-quark and a quark, carrying a small relative transverse momentum. These spectator particles form two separate color triplet strings with the produced heavy quark and anti-quark, respectively. The strings (and all other partons) are hadronized with JETSET 7.4 (Sjöstrand, 1994).

Herwig 5.9

HERWIG 5.9 (Marchesini, *et al.*, 1992) provides a unified description of all hadron emission reactions with interfering gluons in lepton-lepton, lepton-hadron, and hadron-hadron scattering. The basic structure of the program is the same as in the case of AROMA 2.2 and assumes a factorization of the process into the following parts:

- *Initial state radiation*, where a parton constituent of an incident hadron with low space-like virtuality radiates time-like partons. In this process it decreases its energy to a fraction x of that of the hadron and increases its (space-like) virtual mass. This mass is bound in absolute value by the scale Q of the hard subprocess.

- *Hard subprocess*, which is calculated at leading-order with perturbation theory. The momentum transfer scale Q sets the boundary conditions for inital and final state parton showers.
- *Final state radiation*, which is the emission of partons with consecutively lower virtualities. The total amount of emission depends on the upper limit of the virtuality of the initiating parton.
- *Hadronization*, which converts the partons into hadrons and consequently takes place at a low momentum transfer scale. The phenomenological model used is significantly different from the string fragmentation used in AROMA 2.2 and is discussed below.

In HERWIG hadronization is done with the 'cluster-hadronization model'. After the perturbative parton branching process has ended (when the virtuality of the radiated parton drops below a cut-off value Q_0), all outgoing gluons are split into light quark-antiquark pairs. A color line can be drawn from each quark to some antiquark, thus forming a color-singlet *cluster*. These clusters have distributions of mass and spatial size that peak at low values, fall rapidly for increasing cluster masses or sizes, and are asymptotically independent of the hard subprocess ("preconfinement"). All clusters are iteratively decayed until only hadrons remain as follows:

- If the mass of a cluster is too light to decay into two hadrons, it is taken to represent the lightest hadron of its flavor. Its mass is shifted on-shell by an exchange of momentum with a neighboring cluster.
- Those clusters massive enough to decay into two hadrons, but below a fission threshold M_f, decay isotropically into pairs of hadrons. The fission threshold M_f is roughly $M_f \sim 4\,\mathrm{GeV}$.
- If the cluster mass is larger than the fission threshold M_f, the cluster decays into two daughter-clusters, moving in the direction of the original constituents.

The measured transverse energy flow cannot be reproduced without the incorporation of a "soft underlying event". This consists of an interaction of the p remnant with the partons emitted during initial state radiation.

Chapter 3

Muon Identification in the Barrel

Muons are *measured* as tracks in the inner tracking chambers and *identified* by their tracks in the dedicated muon detector incorporated into the instrumented iron return yoke. This identification requirement leads to a very small acceptance in the region of low transverse momentum $p_\perp \lesssim 2\,\mathrm{GeV}/c$. The ensemble of tracks identified as muons will be referred to as "muon sample". In this sample, a certain amount of particles will be due to hadrons faking a muon signature ("fake muons"). A thorough understanding of both muon identification and fake muon contribution to the muon sample is needed for the subsequent analysis.

This chapter starts with a description of the hard- and software used for the measurement of high-$p_\perp$ muons in the central region of H1. The identification criteria for muons are discussed and improvements are studied. The focus is then shifted to the background in the muon sample and a new method to describe this background is introduced. Section 3.4 provides an overview of the method and its experimental verification; the remaining parts of the chapter cover the details.

3.1 The Instrumented Iron Return Yoke

The detection of tracks of penetrating particles, *e.g.* muons, is done in the instrumented iron return yoke. It is divided into three sub-detectors (*cf.* figure 9): The forward and backward end-caps and the barrel surrounding the main solenoid magnet. The barrel is furthermore subdivided into a forward and backward part. Ten iron plates with a thickness of 7.5 cm are separated by slits which are on average 2.5 cm wide. Roughly 103'000 limited streamer tubes (LST) are mounted in the slits and on the inner and outer surface of the iron yoke. For safety reasons the LST are built of the halogen free plastic Luranyl. They are operated with a non-inflammable gas mixture of 88% CO_2, 9.5% isobutane, and 2.5% argon at normal pressure.

A view of the basic structure of a LST is shown in figure 7. The building block of each chamber consists of *profiles* containing eight *cells* with a size of $10 \times 10\,\mathrm{mm}^2$.

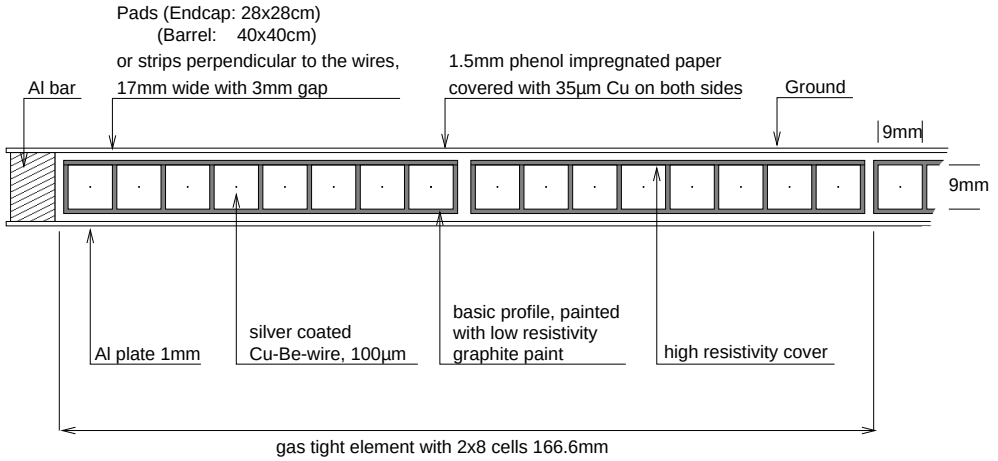

Figure 7: Structure of a limited streamer tube (LST) consisting of two profiles with eight cells each (Itterbeck, 1997).

A silver coated Cu-Be wire of $100\,\mu$m diameter occupies the center of each cell and is kept at ground potential. The cell walls are coated with graphite paint to yield a low surface resistivity of $\sim 10 - 30\,\mathrm{k}\Omega/\square$. They act as cathodes and have a high voltage of 4.5 kV applied. A Luranyl cover with high resistivity is glued to the top of the profile. Two profiles are put together into a gas tight *box* made out of Luranyl. All connections for gas, signal lines and the high voltage are provided on one end of each box. Several boxes together form a complete streamer tube layer, which is mounted on an aluminum *plate*. Either *strips* or *pads* are glued onto the high resistivity (top) side of the planes, acting as electrodes where influence charges are induced and measured. The strips are 17 mm wide with a spacing of 3 mm. The size of the pads varies from 25 cm $\times$ 25 cm in the end-caps to 50 cm $\times$ 50 cm in the barrel region. The complete LST layer has a thickness of 2.5 cm.

The wire orientation in the barrel is parallel to the z-axis, while the strips lie in the xy-plane. In the end-caps, the wires are parallel to the x-axis and the strips are oriented along the y-axis. As the strips are perpendicular to the wires, a two-dimensional space measurement can be made. Wires and strips are read out digitally. The analog signals of the 11 pad layers are added (5 inner and 6 outer layers) to form two *towers*. They are mainly used in the energy measurement of the tail catcher.

The configuration of the layers within the iron yoke is shown in figure 8. All slits contain at least one LST layer with pad electrodes. Starting from the inside, three layers (one pad and two strip layers) form a *muon-box* in front of the iron yoke. The fourth slit in the iron is 5 cm wide (twice the standard width) and contains two layers with pads and strips. On the outer side of the iron, another muon-box is mounted. There are in total 16 LST layers in depth, out of which 10 are located directly after

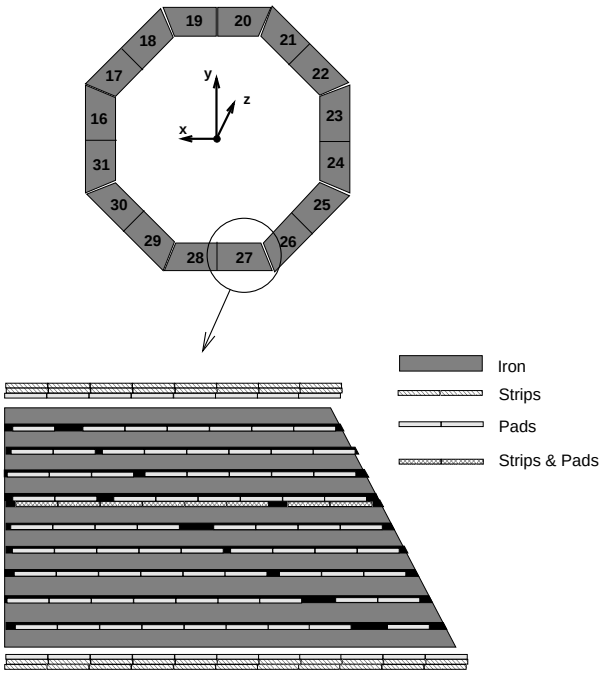

Figure 8: Configuration of the layers in the instrumented iron return yoke. The upper plot shows a cut through the backward barrel, the lower plot is an enlargement of one of the lower octants. The black areas between the iron plates are not filled by LST and limit the total muon reconstruction efficiency to $\epsilon_{rec} \sim 0.9$ in the central region. The two muon-boxes of three layers each are seen on the inside and outside of the iron return yoke (Itterbeck, 1997).

an iron plate. Only these layers are used for defining the muon quality as described in section 3.6. The energy loss of a minimum ionizing particle per iron plate is 90 MeV at perpendicular incidence, the multiple scattering angle amounts to ~ 30 mrad for a momentum of 1 GeV/c (in the iron).

Each of the four sub-detectors of the instrumented iron return yoke consists of 16 *modules* as shown in figure 9. Each module is built of seven to ten boxes in the barrel. In the end-caps five boxes make up one module. The geometrical acceptance of the instrumented iron return yoke is shown in figure 10, which also indicates the position of the modules. Several holes are visible and have the following *raisons d'être*. The hole at the bottom with $(\phi, \theta) \sim (4.6, 1.3)$ is due to a LAr transfer line of H1. The hole on top with $(\phi, \theta) \sim (1.5, 2.2)$ is occupied by the main cryogenics supply lines. The small hole visible at $(\phi, \theta) \sim (4.8, 2.1)$ is also due to cryogenics.

These holes in the instrumented iron return yoke limit the muon reconstruction efficiency to $\epsilon_{rec} = 0.89$ as plateau value for $p_\perp > 2$ GeV/c (*cf.* Section 3.6).

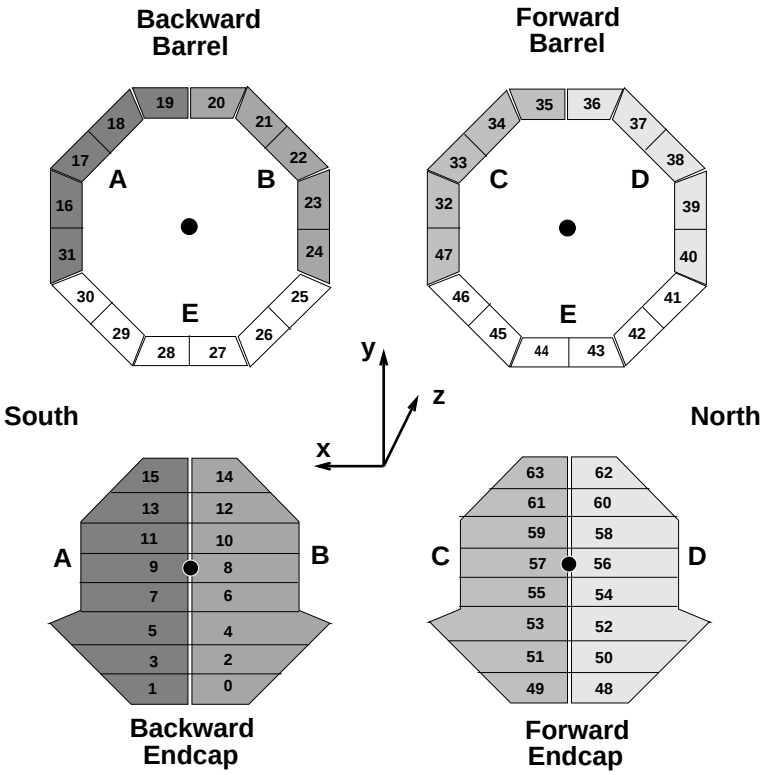

Figure 9: Overview of the arrangement of modules in the instrumented iron return yoke (Itterbeck, 1997).

3.2 Track Reconstruction in the Instrumented Iron Return Yoke

Tracks of charged particles are reconstructed in two separate steps: All hits belonging to a single track are found by the pattern recognition program. They are grouped into associations. The track parameters of associations passing basic quality criteria are determined by a fit of parabola sections through the iron hits assigned to that track. The result are the following parameters per track: space point of the first hit, the direction of flight at this point and Q/p, the ratio of charge and momentum. The last parameter is measured with an accuracy of only $\sim 30\%$ in the barrel, due to the inhomogeneities of the magnetic field in the iron.

The pattern recognition program (Kleinwort and Krüger, 1992) is running independently for the barrel and the two end-caps. Tracks crossing from the barrel into one of the end-caps are not recognized as such and are typically lost due to their short length within one sub-detector. This leads to a significant decrease of the track reconstruction efficiency in the overlap region.

A particle can produce hits on several neighboring wires depending on the angle of its direction of flight relative to the LST plane. The strip electrodes suffer from cross-talk of charge leading again to multiple hits per particle on the same plane. Therefore the first step of the reconstruction program is to group hits on neighboring

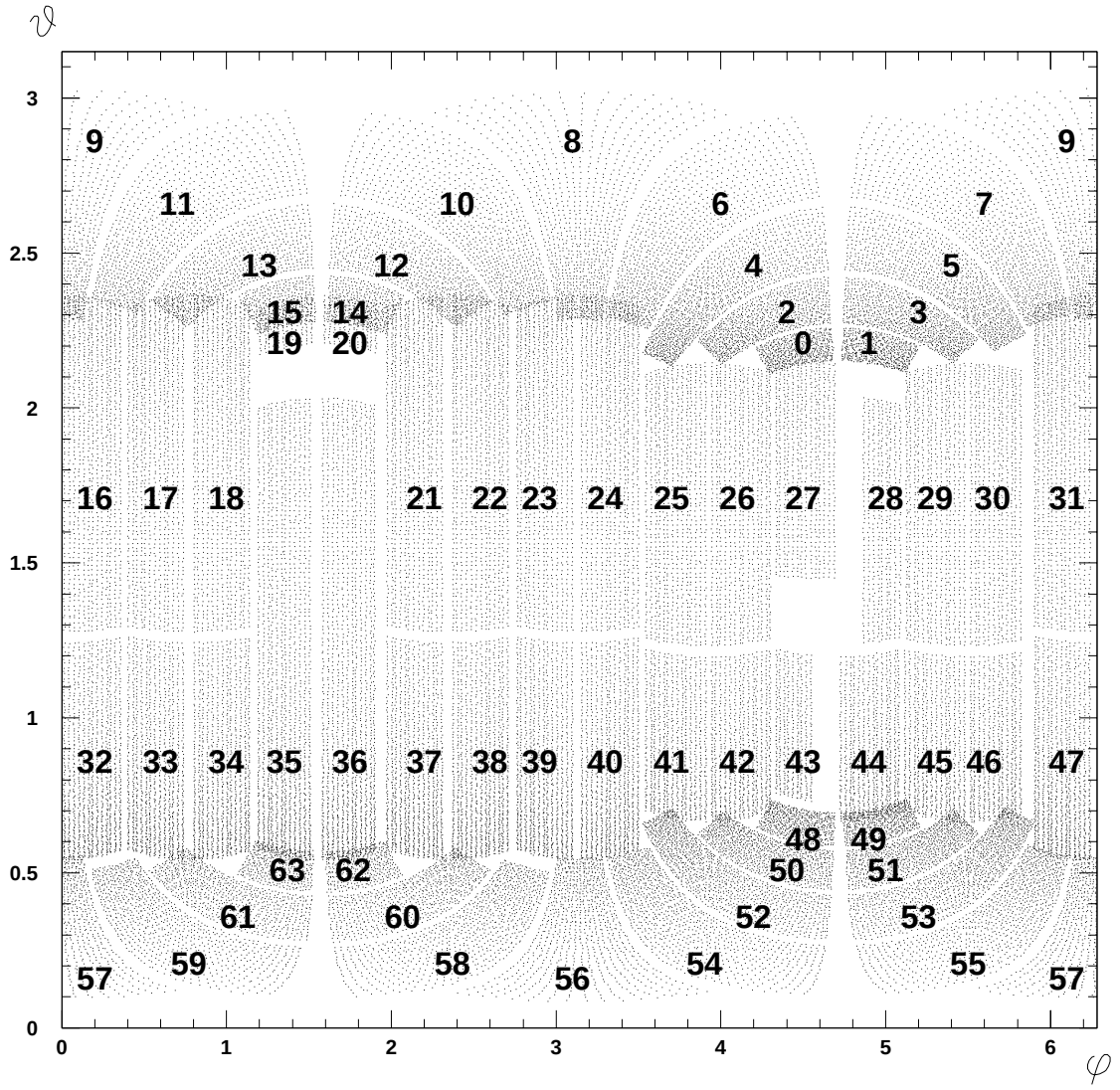

Figure 10: Acceptance of the instrumented iron return yoke. The numbers in the plot correspond to the module number as given in figure 9 (Itterbeck, 1997).

strips or wires into *super-hits*. This deteriorates the double hit resolution to 2 cm for the wires and 4 cm for the strips, but leads to a significant decrease in the combinatorial background. The grouping is done separately for wires and strips. In order to shorten the computing time, the super-hits are filtered and searched for isolated tracks where nearly all layers have a hit. In addition, shallow hit distributions measured in two neighboring layers only (indicative of a particle shower) are eliminated.

In the next step, up to four neighboring modules (in ϕ) containing a wire hit are

grouped together into *sectors*. This allows a transformation into a two-dimensional co-ordinate system such that the x-axis is perpendicular to the wires and strips. All modules with a strip hit form their own sector.

As the co-ordinates of a wire hit in the muon detector do not necessarily lie in a plane, a local two-dimensional co-ordinate system (u, v) has to be defined for each sector. The pattern recognition is done with a two-dimensional histogramming method (conformal mapping), which maps every space point (u, v) into a sine curve or straight line in a two-dimensional parameter space. All points belonging to the same straight track lead to curves intersecting in one point in the parameter space. Recognizing tracks is thus reduced to finding maxima in this parameter space. Once a maximum is found, all its hits are assigned to an *association* and removed from the sample. The search continues until no significant maxima remain. The associations are subjected to some quality checks rejecting candidates with too few hits or too many hits within the same layer.

The conformal mapping is not well suited for strongly curved tracks, as the points no longer lie close to each other in the parameter space. This is basically avoided by choosing a binning coarse enough to accommodate the largest possible curvature. In addition, associations from neighboring modules are checked for originating from the same track and combined if necessary.

Combining wire and strip associations leads to associations in three-dimensional space. Towers are used if missing strip hits prevent a reconstruction of the full three-dimensional information. The final associations are grouped into three categories:

- No association, if it consists of a single strip or wire hit or if it has been identified as a particle shower.
- Special association, if there are less than three iron plates between the first and last wire plane (except for hits in the muon boxes).
- Muon association in all other cases.

Only muon associations are used for the track fitting.

Track fitting is only done for muon associations satisfying two additional requirements: At least three wire hits and one strip or pad signal have to be present. The distance between the first and the last wire hit has to be larger than 15 cm. The co-ordinate system for track fitting is chosen as follows. The x-axis is perpendicular to the iron plates, and the y-axis is measured by the wire or strip signals. The z-axis is added such that a right-handed three-dimensional co-ordinate system results. Since the magnetic field in the return yoke is very inhomogeneous, the curvature of a track is not constant and the instrumented iron return yoke has to be divided into 21 regions (10 iron plates, 9 slits in between, and the two muon boxes on the inside and outside surface). In each region a mean magnetic field is chosen and a parabola is fitted to the wire and strip hits:

$$y_i(x_i) = a_i + b_i \cdot x_i + c_i \cdot x_i^2 \quad i = 1, \ldots 21,$$

where (x_i, y_i) are the hits in the plane co-ordinate system and (a_i, b_i, c_i) are the parameters being fitted in each of the 21 regions. Strip and wire information lead to 2×63 free parameters. 2×40 constraints arise from continuity conditions (in place and slope) between adjacent regions for both wires and hits. Parameter c_i is related to Q/p_0 of a track and the magnetic field B_i within region i via the following equation

$$c_i = const \cdot \frac{Q}{p_0} B_i \frac{p_0}{p_0 - dE_i},$$

where p_0 is the momentum of the particle at the beginning of the track and dE_i the energy loss in plate i. This relation adds another 2×21 constraints and introduces one free parameter Q/p_0. This leads to a total of $2 \times (63 - 40 - 21) + 1$ free parameters, which are determined by minimization of the following χ^2 function.

$$\chi^2 = \sum_{wires} \frac{1}{\sigma_w^2}(y_d(x_{fit}) - y_{fit})^2 + \sum_{strips} \frac{1}{\sigma_s^2}(y_s(x_{fit}) - y_{fit})^2,$$

where $\sigma_w = 0.4\,\mathrm{cm}$ and $\sigma_s = 1\,\mathrm{cm}$ are the resolutions of the wires and strips, respectively. The fitting is done in an iterative procedure taking into account the non-linear correction in Q/p_0 due to the energy loss in the iron plates. In the first iteration, the energy loss is neglected. In subsequent steps, the previously determined value of p_0 is used and the effective magnetic field B_i is recalculated.

3.3 Muon Track Linking

Tracks found in the iron return yoke ("iron tracks") are used only as a means of *identifying* tracks *measured* in the central drift chamber ("inner tracks") as penetrating particles. This section describes the linking of inner tracks to iron tracks resulting in "muon tracks".

Starting from a track in the inner tracker, iron tracks are searched and the following criteria must be fulfilled before the linking is attempted:

- The difference of the polar angles must be smaller than 12°:

$$|\theta_{inner\ tracker} - \theta_{iron\ track}| < 0.2\,\mathrm{rad}.$$

- The difference of the azimuthal angles has to be within a certain range, which is chosen asymmetrically so that an angular difference of 90° is possible in the direction of the curvature.

$$-\frac{\pi}{2} < (\phi_{inner\ tracker} - \phi_{iron\ track}) < \frac{\pi}{2} \qquad \text{if } \kappa > 0,$$
$$-\frac{\pi}{2} < (\phi_{iron\ track} - \phi_{inner\ tracker}) < \frac{\pi}{2} \qquad \text{if } \kappa < 0.$$

- The momentum p of the particle in the inner tracker must be above $p > 1\,\mathrm{GeV}/c$ in order to be able to reach the iron system.

For all track combinations passing these criteria, the inner track is extrapolated to the inner edge of the iron system. It is assumed that these particles are minimum ionizing particles, and only the energy loss according to the Bethe-Bloch equation and a multiple scattering angle $\propto p^{-1}$ are taken into account. The detector is divided into 36 different volumes. The material constants are averaged over each volume, and the particle is propagated through the entire detector stepwise.

A χ^2 is calculated with the extrapolated track according to the following equation:

$$\chi^2 = (X_E - X_I)^T V^{-1} (X_E - X_I),$$

where X_E and X_I denote a vector containing track parameters of the extrapolated and the iron track, respectively. In the barrel, X_I contains the z-co-ordinate of the first track point, the azimuthal angle ϕ_{point} of this first point in the xy-plane, and the direction of flight ϕ_{flight} at that point. The non-diagonal matrix V is the sum of the covariance matrices of the extrapolated and the iron track. With this χ^2 a confidence level is calculated, giving the *link probability*.

3.4 Background in the Muon Sample: Sources and Strategies

All tracks in the instrumented iron return yoke linked to a track in the inner tracking chambers constitute a muon candidate. This muon sample contains — apart from genuine muons originating from an ep collision — muons from cosmic rays and "fake muons" from hadrons.

This section starts with an overview on the different background sources contributing to the muon sample. In the second part, two different strategies for *(i)* suppressing and/or *(ii)* describing this background are introduced. The final subsection introduces the cross checks and verifications done. The remainder of the chapter presents the details of the strategy as summarized in this section.

Background Sources

The muon flux at sea level has a mean energy of 2 GeV with a differential spectrum falling as E^{-2}. Muons constitute approximately 75% of the entire cosmic ray particle flux. They can reach the H1 detector as penetrating particles and lead to measured muon tracks. Cosmic muons pose a problem for analysis only if they pass the detector right through the event vertex during a genuine ep interaction. The rejection of cosmic muons is described in section 3.5.

Most of the hadronic background in the muon sample is due to events where only light quarks have been produced. Hadronic decay of heavy quarks provides only a tiny contribution, as heavy quark production is strongly suppressed compared to light quark production. Hadrons can lead to a muon track in the iron system via various mechanism as discussed in the following.

- In-flight decay: Most hadrons are not stable particles, but have a finite life-time τ. The most frequent hadron emerging at ep collisions at HERA is the charged

pion, decaying after a mean life-time of $\tau = 2.6 \cdot 10^{-8}$ s into $\pi^{\pm} \to \mu^{\pm}\nu_{\mu}$ with a $c\tau = 7.8$ m. The charged kaon is the next most frequent particle at HERA. It decays dominantly into $K^{\pm} \to \mu^{\pm}\nu_{\mu}$ with $\tau = 1.2 \cdot 10^{-8}$ s, corresponding to $c\tau = 3.7$ m.
The probability for an unstable particle to decay within some distance x is given by

$$P(x) = 1 - e^{-x/\beta\gamma c\tau}, \tag{5}$$

where β is the particle velocity in units of c, and γ is the ratio of its energy and mass. This implies that roughly 0.1% of all pions and 1% of all kaons with momentum $p = 2\,\mathrm{GeV}/c$ decay into muons before entering the LAr calorimeter. The kink at the decay vertex of a pion is typically very small and not recognized by the track reconstruction program. In the case of a decaying kaon, the influence can be seen by a small deterioration of the measurement of the transverse momentum.

- Sail through: Hadrons can traverse the material in front of the instrumented iron return yoke without interacting strongly. The probability for this is given by

$$P(x) = e^{-x/\lambda},$$

where λ is the interaction length and x is the distance traversed. At H1, the material in front of the barrel muon system varies between 4.5 and 8 interaction lengths at a polar angle of $\theta = 90°$ and $\theta = 35°$, respectively. This implies a maximum probability of $\sim 0.6\%$ for a hadron to reach the iron system without strong interaction. Due to support structures, cabling, and cryogenic supplies, $\lambda(\theta)$, describing the amount of material in front of the instrumented iron return yoke as a function of the polar angle, does not follow a simple $\lambda(\theta) \propto 1/\sin(\theta)$ behavior, but rather as shown in figure 11.

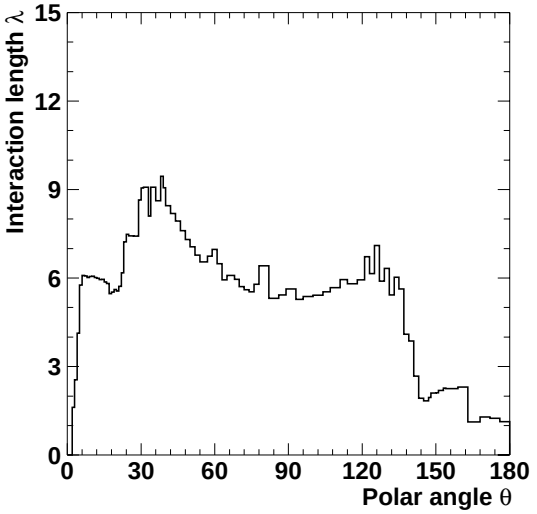

Figure 11: Material between the interaction point and the first layer of the instrumented iron return yoke as a function of the polar angle θ.

At low momentum, in-flight decay is expected to be substantial. Sail-through, once above threshold for reaching the instrumented iron return yoke, is expected to dominate in the high momentum range, where in-flight decay dies out exponentially. This is corroborated in the simulation. Up to a momentum of $p \sim 3.5\,\mathrm{GeV}/c$, in-flight decay and sail-through contribute equally to the detected background muons in the instrumented iron return yoke.

- Punch-through: Hadronic energy leaking out of the LAr calorimeter can produce showers in the instrumented iron return yoke. The shower typically shows a shallow distribution, but can nevertheless pass a few layers. The muon reconstruction program tries to identify shower candidates.

Strategies against Fake Muons

Fake muons, the contribution of hadrons to the muon sample, can be handled with at least two different methods. On the one hand, tightening the quality criteria imposed on a muon candidate will *purify* the sample. Unfortunately, this does not eliminate the background stemming from in-flight decay at low momenta (where most of the statistics is found). After all, this background consists of genuine muons. Some results of studies done along this line are presented in section 3.6.

The second approach is to *estimate* the amount of fake muons. This can be done if a precise knowledge of the misidentification probability $P_h^\mu(p,\theta)$ is available. $P_h^\mu(p,\theta)$ is the probability that a hadron h measured in the CJC with momentum p and polar angle θ is detected as a muon in the instrumented iron return yoke. Folding the hadronic particle spectrum of any variable with this probability yields the estimate of the fake muon contribution in the corresponding muon spectrum. As $P_h^\mu(p,\theta)$ is not the same for different species of hadrons, the relative contributions $f_h^{\pi,K,p}$ of pions, kaons, protons, *etc.* to the entire hadronic spectrum must be known.

Both $P_h^\mu(p,\theta)$ and the particle composition are taken from MC simulations. The misidentification probability contains no model dependency. In-flight decay is completely described by equation (5), and the interactions of hadrons (π, K, p) with nuclear matter have been well measured in the relevant energy range of $1 - 10\,\mathrm{GeV}$. A slight model dependence has to be accepted for $f_h^{\pi,K,p}$, *i.e.* the assignment of a specific type to a given hadronic track in data. The particle composition of all tracks is determined mainly by the hadronization model used. It is taken as the Lund string model as implemented in JETSET 7.4, which has been tuned to describe the data properly. Measurements at H1 (1996a), SLD (1997), and DELPHI (1997) have shown that its description is indeed good.

This approach allows a very good description of the background and is described in detail in section 3.7.

Verification of the Fake Muon Estimate

It must be verified that the misidentification probabilities (as extracted from a MC simulation) for a *single* particle type describe the data. It is furthermore mandatory to show that the *general* misidentification probability, which is no longer restricted to a

single particle type, is properly described by $f_h^{\pi,K,p} \otimes P_h^\mu$. The following first two points introduce the verifications done in the single particle case, the last point summarizes the verification done for $f_h^{\pi,K,p} \otimes P_h^\mu$.

- The direct comparison of the misidentification probabilities for a single particle type in data and MC simulation is restricted to the case of pions. A clean pion sample is selected both in data and in the MC simulation via the decay $K_S^0 \to \pi^+\pi^-$, and $P_\pi^\mu(p)$ and $P_\pi^\mu(\theta)$ are extracted and compared. A priori a similar study should be done for other particle species as well, but the statistics available in the high-$p_\perp$ region inhibit this. Section 3.8 provides the details on the pion selection and the results of the comparison.
- An indirect verification of P_h^μ is provided by the comparison of the *estimated* muon yield in a sample of pions (or kaons) with the actually *measured* muon yield. Assigning $P_h^\mu(p,\theta)$ as weight to every pion (or kaon) and summing over all particles should reproduce the fake muon yield measured in that sample. Pions are selected as above, kaons are identified via the decay $\phi \to K^+K^-$. The results of this cross check are presented in section 3.9.

  It will be seen in section 3.8 and 3.9, that the MC simulation provides a very good description of the misidentification probability for both pions and kaons.
- As the particle identity is in general not known in data, the misidentification probabilities $P_\pi^\mu(p,\theta)$, $P_K^\mu(p,\theta)$, and $P_p^\mu(p,\theta)$ have to be averaged appropriately. This averaging is done with $f_h^{\pi,K,p}$ and is cross checked with a light-quark MC event sample, where no genuine muons are present. All muons found in the simulation of this event sample are fake muons and should be reproduced by the estimate when summing over all hadrons with a weight of $f_h^{\pi,K,p} \otimes P_h^\mu$. Section 3.10 discusses the results.

3.5 Rejection of Cosmic Muons

The rejection of cosmics is done on different levels and is based on varying information provided by the muon detector and the inner trackers. A special cosmic finding algorithm is run during the event reconstruction on L5, if two iron tracks are

- successfully linked to inner tracks,
- have — within errors — the same momentum, and
- lie back-to-back in the xy-plane.

The "upper" track is reconstructed from scratch by assuming that the particle entered the detector from the outside. If the two muon tracks can be connected with a link probability $P(\chi^2) > 10^{-4}$, both tracks are masked as cosmic tracks.

Two muon tracks (as measured in the CJC) are furthermore rejected as cosmics, if they can be connected to a straight line in the rz-plane, *i.e.* if they satisfy the criterion

$$175^\circ < \theta_1 + \theta_2 < 185^\circ.$$

Another cosmic finder is run before analysis, which does not rely on the requirement of the two iron tracks being linked to inner tracks. Instead, two iron tracks are extrapolated with information obtained from the instrumented iron return yoke alone. The iron track pair is rejected for further analysis, if the opening angle between the two tracks is less than $\vartheta < 25.8°$. This finder removes cosmics where one of the two iron tracks was successfully linked to an inner track, but the second track could not be linked. (Such a case would not be tagged by the previously mentioned finder, which requires *both* iron tracks to be linked to inner tracks.)

Two further cuts are applied to exclude cosmic muons from the analysis: *(i)* As cosmics show a continuous flux with respect to the HERA clock, a strong rejection can be achieved by selecting only those muon candidates having nominal timing properties (measured in the CJC):

$$-5\,\mathrm{ns} < \mathrm{t_{CJC}} < 5\,\mathrm{ns}.$$

(ii) Muons with large distances of closest approach d_{ca} are rejected as being not related to the primary event vertex; they are effectively removed by requiring

$$|d_{ca}| < 2\,\mathrm{cm}.$$

3.6 Improved Muon Identification in the Barrel

The basic quantities* describing the quality of an iron track are given in terms of the layers where the track is measured. A layer as used below is defined as a layer *behind* an iron plate. This implies that the first three physical LST layers (in the muon-box on the inside surface of the iron return yoke) do not count. The two LST layers in slit # 4 and the muon-box on the outer surface count as one layer.

- *rlay0* gives the first layer, which measured a wire hit. This parameter is restricted to the range $rlay0 \in [3, 5]$. The lower bound is due to the missing muon-box layers, the upper bound is due to the standard cut.
- *rlayer* is the total number of layers with a hit, which is limited to $rlayer < 10$, as there are only 10 iron plates in the instrumented iron return yoke. A minimum of $rlayer > 2$ is required by the muon identification code.
- *rlay1* gives the last layer. This parameter is in the range $rlay1 \in [4, 12]$. The lower limit is a result of the default cuts on *rlay0* and *rlayer*, the upper is due to the fact, that there are no iron plates after LST layer #12.
- *rsfrac* is the fraction of layers where a hit was measured. It is defined as $rsfrac = rlayer/(rlay1 - rlay0 + 1)$.
- In the barrel the derived quantity $rlst = rlay1 \,/\, \sin\theta$ is proportional to the effective amount of iron which has been traversed.

* The nomenclature is based on the muon selection code of the Heavy Flavor Working Group (West, 1996).

rsfrac does not allow a good separation between genuine muons and hadronic background and has been listed only for the sake of completeness. It will not be used any further.

Standard Cuts

In the following, standard cuts for muon identification in the instrumented iron return yoke imply:

- The muon has to be identified in the instrumented iron return yoke. Additional identification in the LAr calorimeter is possible, but not requested.
- The iron track has to be linked to the inner track with a link probability of more than $P(\chi^2) > 10^{-3}$.
- If an iron track is linked to several inner tracks, only one link is kept. Those candidates with a lower link probability are rejected.
- A minimum of 2 layers *behind iron plates* is required, $rlayer \geq 2$.
- The innermost layer must be within the first two layers, $rlay0 \leq 3$.
- The outermost layer must be at least in the second layer, $rlay1 \geq 2$.

The muon reconstruction efficiency as obtained from a MC simulation with these standard cuts is shown in figure 12 as a function of the muon momentum p in different bins of polar angle θ. A clear threshold is visible over the entire barrel. The onset of this threshold and the value of the subsequent plateau depend (mainly) on the dead material in front of the muon system. Two further effects can be noted. The efficiency is lower in the region $70° < \theta < 80°$ due to a LAr transfer line. The forward and backward regions suffer not only from an increased amount of dead material, but also from the missing linking of tracks extending from the barrel into the end-caps.

Improved Cuts

The simulation of the instrumented iron return yoke is sufficiently accurate to allow a systematic study of the muon identification quantities for different particle samples. This has been done with a sample of 10^5 muons, $5 \cdot 10^6$ pions and $3.5 \cdot 10^6$ kaons, which were generated in single-particle events and passed through the full simulation and reconstruction chain. The simulation and reconstruction was based on the conditions of the running period 1995.

Tuning some of the cuts imposed on the muon track quantities allows a better rejection of fake muons. It will always be accompanied by a certain degradation of the muon reconstruction efficiency. The cuts applied in the following are visualized in figures 13 – 15. The cut variables are displayed in the top row for muons (a), pions (b), and kaons (c). The middle and bottom row show the muon reconstruction probability for standard cuts (solid histogram) and tightened cuts (open points) as a function of the particle's transverse momentum and polar angle, respectively. For the $p_\perp$ distributions, a cut on the polar angle of $\theta \in [30°, 140°]$ has been applied. The polar angle distributions are obtained from particles with transverse momentum $p_\perp > 1.5\,\mathrm{GeV}/c$. Note the dip at $70° < \theta < 80°$, which is due to a LAr transfer line.

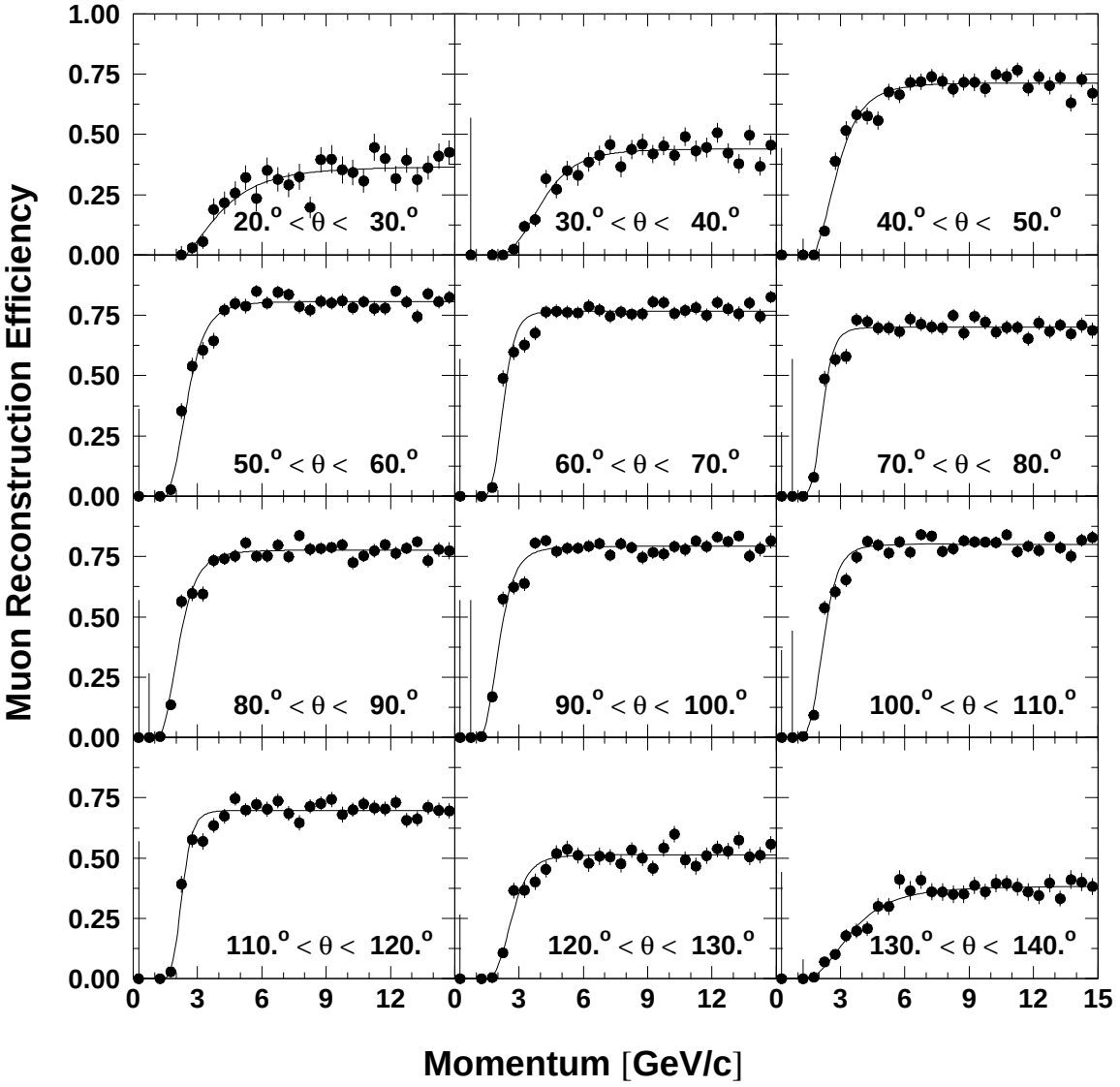

Figure 12: Reconstruction efficiency for muons identified in the instrumented iron return yoke as a function of momentum in different bins of polar angle θ. The filled points are from a MC simulation, the solid line corresponds to a fit to the points.

The following parameters for a discrimination between genuine muons and hadronic background have been studied:

- The "best" one-dimensional cut to reduce background in the *high momentum* muon sample is to tighten *rlay1* to

$$rlay1 > 10.$$

Hadrons 'sailing' through the detector and measured in the iron system have a larger probability than genuine muons of being stopped in an iron plate. This

leads to shorter tracks. It can be seen in figure 13 that this cut reduces the muon reconstruction efficiency significantly in the region where tracks from the barrel extend into the backward end-cap (at polar angles $\theta > 120°$) or from the barrel into the forward end-cap (at $\theta < 50°$). This is due to the fact that these iron track segments are not linked between the barrel and the end-caps (*cf.* section 3.2).

- *rlst* allows a finer cut definition than *rlay1*, because it includes the information about the effective path length traveled by the particle. The muon reconstruction efficiency in the forward region is kept high, but the misidentification probability for pions or kaons is not reduced (*cf.* figure 14) at that polar angle when using

$$rlst > 11.$$

This is explained by the fact that the fake muons at this polar angle are entirely due to in-flight decay, as the amount of dead material in front of the instrumented iron return yoke reaches values of $x \sim 8\lambda$, resulting in a sail-through probability of $3 \cdot 10^{-4}$.

Both of these cuts severely reduce the statistics in the low momentum range for genuine muons, which are stopped before traversing a significant part of the instrumented iron return yoke. If that part of the spectrum has to be saved, it is necessary to use two-dimensional cuts. The two most effective ones will be described in turn.

- Background of kaon in-flight decay can in principle be reduced by making use of the deterioration in the momentum measurement due to the kink in the track. As this cut has a rejection power only slightly better than the following cut and because it does not work for pions, a detailed discussion is not provided.
- The combination of *rlst* vs. transverse momentum $p_\perp$ reduces the fake muon rate with $p > 4\,\mathrm{GeV}/c$ by a factor of two to three, while the absolute muon reconstruction efficiency is lowered by not more than $\sim 5\%$. Muon tracks with

$$rlst < \frac{11}{1 + (\frac{2.5}{p_\perp})^{10}}$$

are rejected as fake muons. However, the reduction on the low-momentum fake muons is virtually negligible (*cf.* figure 15).

The reduction of the muon reconstruction probability for these cuts relative to the standard cuts is shown in figure 16 for muons (a and c) and kaons (b and d) as a function of transverse momentum and polar angle, respectively. In the high-momentum range, a reduction by a factor of two to three can be achieved without reducing the muon reconstruction efficiency significantly. It is advantageous to use the cuts on *rlst* or the two-dimensional cut in the $rlst - p_\perp$-plane, as they result in virtually the same rejection power, but retain a higher muon reconstruction efficiency than the simple cut on *rlay1*.

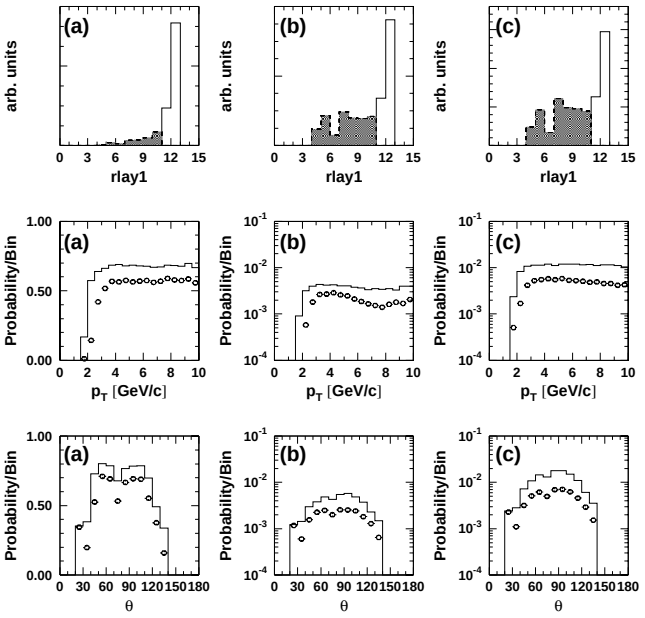

Figure 13: The top row shows the distributions of *rlay1* for muons (a), pions (b), and kaons (c). The shaded histograms indicate the rejected part based on a cut $rlay1 > 10$. The middle and bottom row display the muon reconstruction probability as a function of transverse momentum and polar angle, respectively. The solid histogram corresponds to the set of standard cuts, the open points are for $rlay1 > 10$. Note the different scales for the muons (a) and the hadrons (b) and (c).

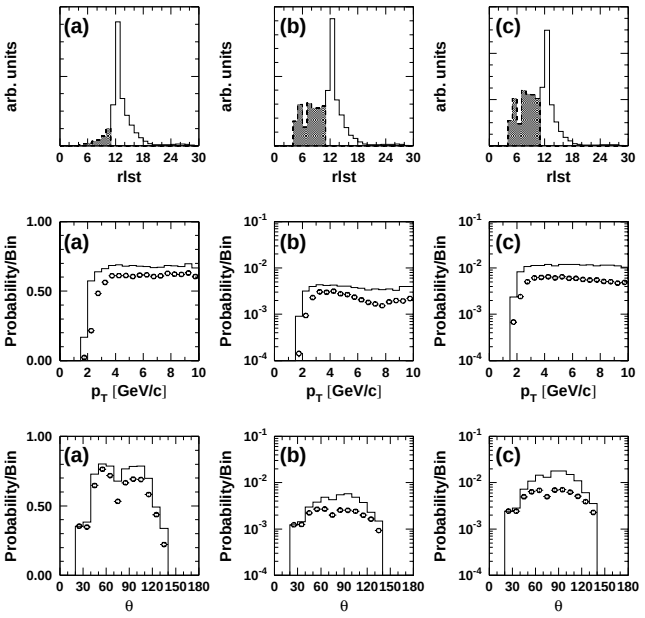

Figure 14: The top row shows the distributions of *rlst* for muons (a), pions (b), and kaons (c). The shaded histograms indicate the rejected part based on a cut $rlst > 10$. The middle and bottom row display the muon reconstruction probability as a function of transverse momentum and polar angle, respectively. The solid histogram corresponds to the set of standard cuts, the open points are for $rlst > 11$.

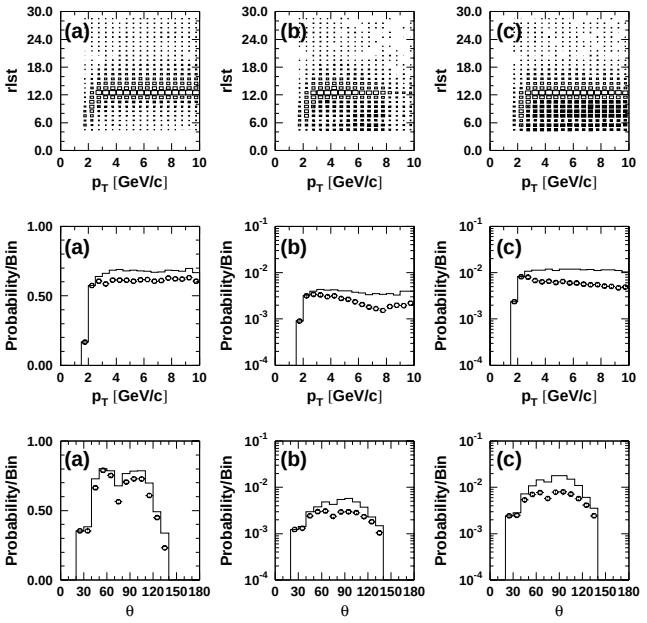

Figure 15: The top row shows the distributions of *rlay1* for muons (a), pions (b), and kaons (c). The dark histograms indicate the rejected part based on a cut in the $rlst - p_\perp$-plane as described in the text. The middle and bottom row display the muon reconstruction probability as a function of transverse momentum and polar angle, respectively. The solid histogram corresponds to the set of standard cuts, the open points are for this two-dimensional cut.

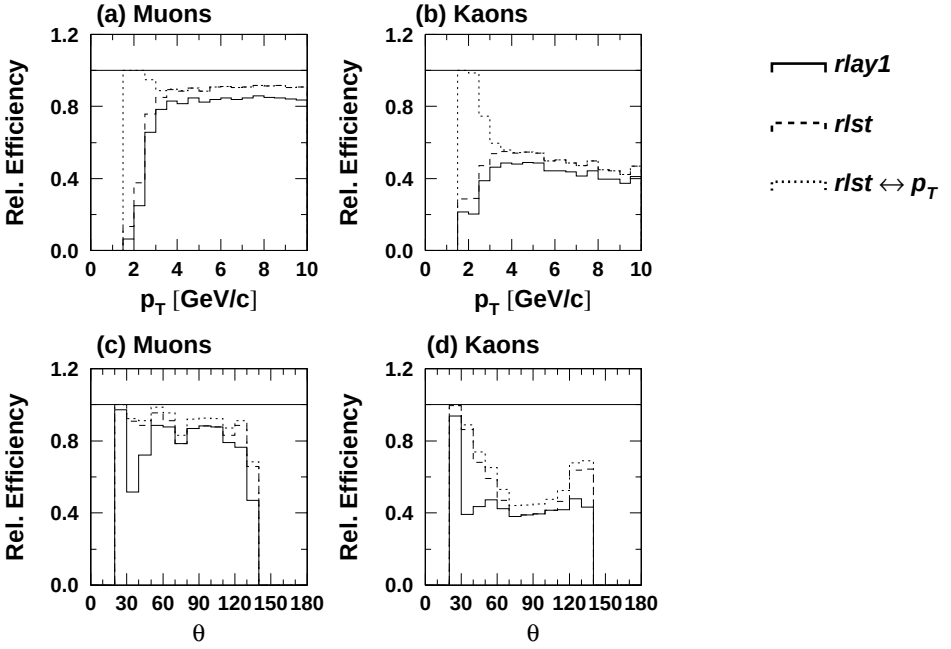

Figure 16: Relative reduction of the muon reconstruction probability compared to the standard cuts (indicated by the solid line at 1). Shown are the transverse momentum and polar angle dependencies for muons (a and c) and kaons (b and d). Three different cuts are used apart from the standard muon reconstruction: The one-dimensional cuts on *rlay1* and *rlst* as well as a two-dimensional cut in the $rlst - p_\perp$-plane, as described in the text.

Conclusion

Three cuts to improve the muon identification in the central region have been presented. They allow a reduction of the hadronic background by a factor of ~ 2, especially in the central region and at high momentum. At low momentum, the background reduction factor is related to a similar reduction of the muon reconstruction efficiency. This is due to the fact that low momentum fake muons are mostly due to in-flight decay.

As most of the decay muons of heavy quark have low momenta, the subsequent analysis will not take advantage of the improved muon identification, but stick to the standard cuts.

3.7 Parameterized Fake Muon Estimation with $P_h^\mu(p,\theta)$

The determination of $P_h^\mu(p,\theta)$ is ideally done with particles of a specific type h in data. The identification of h can be achieved with the reconstruction of particular decays. High statistics is needed for an adequately fine description of $P_h^\mu(p,\theta)$ over the entire acceptance region. As this probability is of the order of $\mathcal{O}(10^{-2})$, an accuracy of 10% requires roughly 100 misidentified hadrons in each bin, which implies a total of 10'000 hadrons per bin. As will be shown below, the binning in the polar angle θ should not exceed 2° unless the particle flux of the data is well described by the event sample used for the extraction of $P_h^\mu(p,\theta)$. These two requirements make the extraction of $P_h^\mu(p,\theta)$ as a function of two variables from data virtually impossible with the presently available luminosity.

Misidentification Probability $P_h^\mu(p,\theta)$

If MC simulations describe the situation properly, the statistics limitation can be remedied by generating large amounts of particles, and simulating and reconstructing them. The validity of the assumption must be verified by comparing partially integrated misidentification probabilities obtained from MC simulations with those from data. In the following, the extraction of $P_h^\mu(p,\theta)$ from MC simulations will be explained.

Roughly $5 \cdot 10^6$ charged pions, $3.5 \cdot 10^6$ charged kaons, and $5 \cdot 10^6$ (anti)protons were generated in events containing only one particle. In order to have enough statistics over the entire phase space, the particles were evenly distributed in $\theta \in [25°, 150°]$ and $p_\perp \in [1\,\mathrm{GeV}/c, 10\,\mathrm{GeV}/c]$. These event samples will be referred to as "toy MC".

$P_h^\mu(p,\theta)$ is obtained from the ratio

$$\frac{\#\text{tracks with } \mu \text{ identification}}{\#\text{tracks in total}} \quad \text{for each bin in } \theta \text{ and } p.$$

The bin size is 2° in polar angle and $200\,\mathrm{MeV}/c$ in momentum. A selection of the resulting probability distributions is shown in figure 17 for charged pions and in figure 18 for charged kaons. In each θ-bin, $P_h^\mu(p)$ represents the misidentification probability

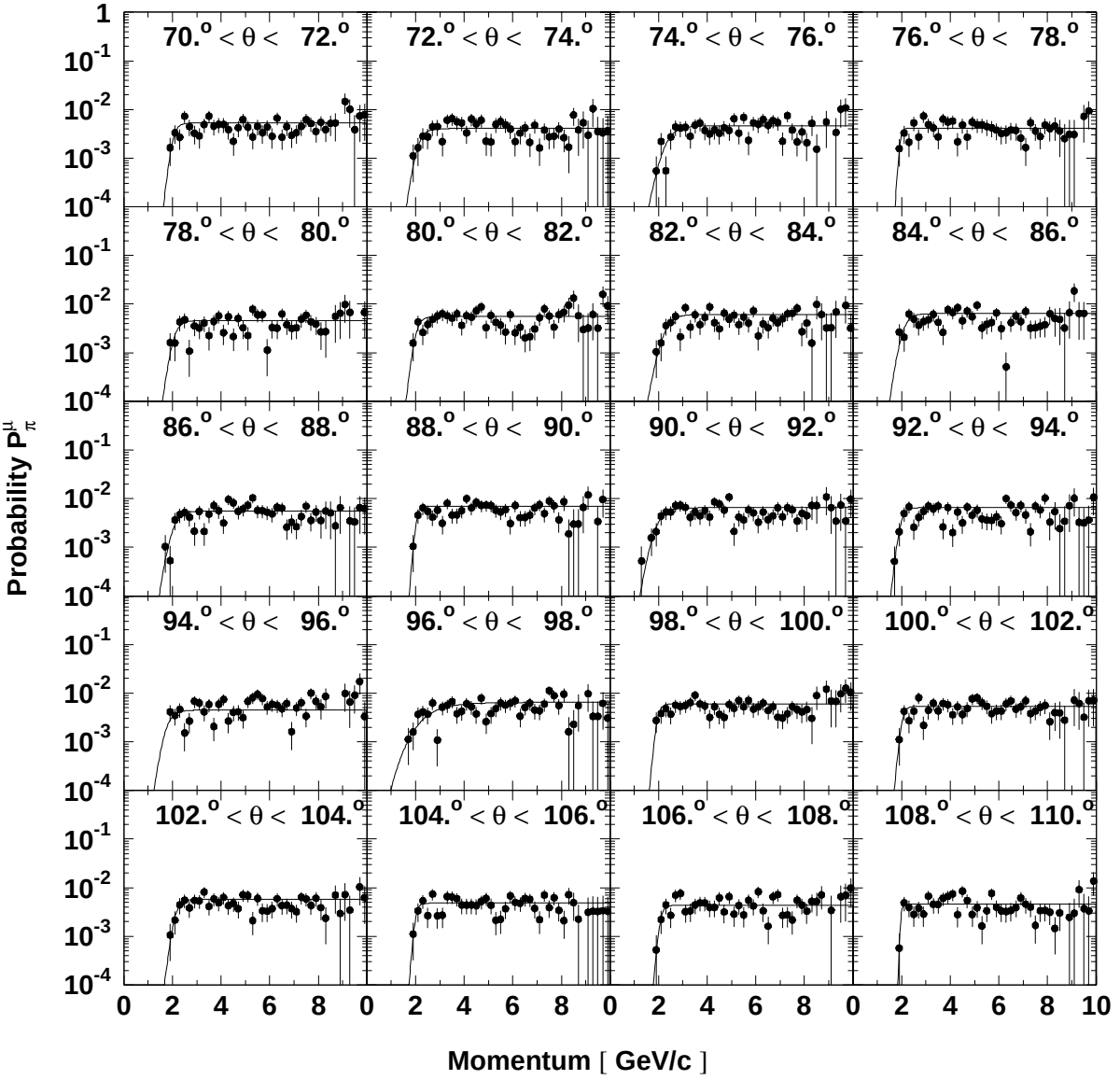

Figure 17: Probability P_π^μ for a pion to be measured as a muon in the instrumented iron return yoke. The filled points are extracted from a MC simulation, the curves correspond to a fit to the points.

evaluated at a mean polar angle. This probability depends strongly on the criteria imposed on muon candidates.

A crucial point is the choice of the bin size for θ. Bin sizes above 2° are too coarse if no assumptions on the particle spectrum are made. A large binning can only be used if the particle flux used for the determination of $P_h^\mu(p,\theta)$ closely describes the data spectrum. If, on the other hand, the particle flux in each bin in θ is different for

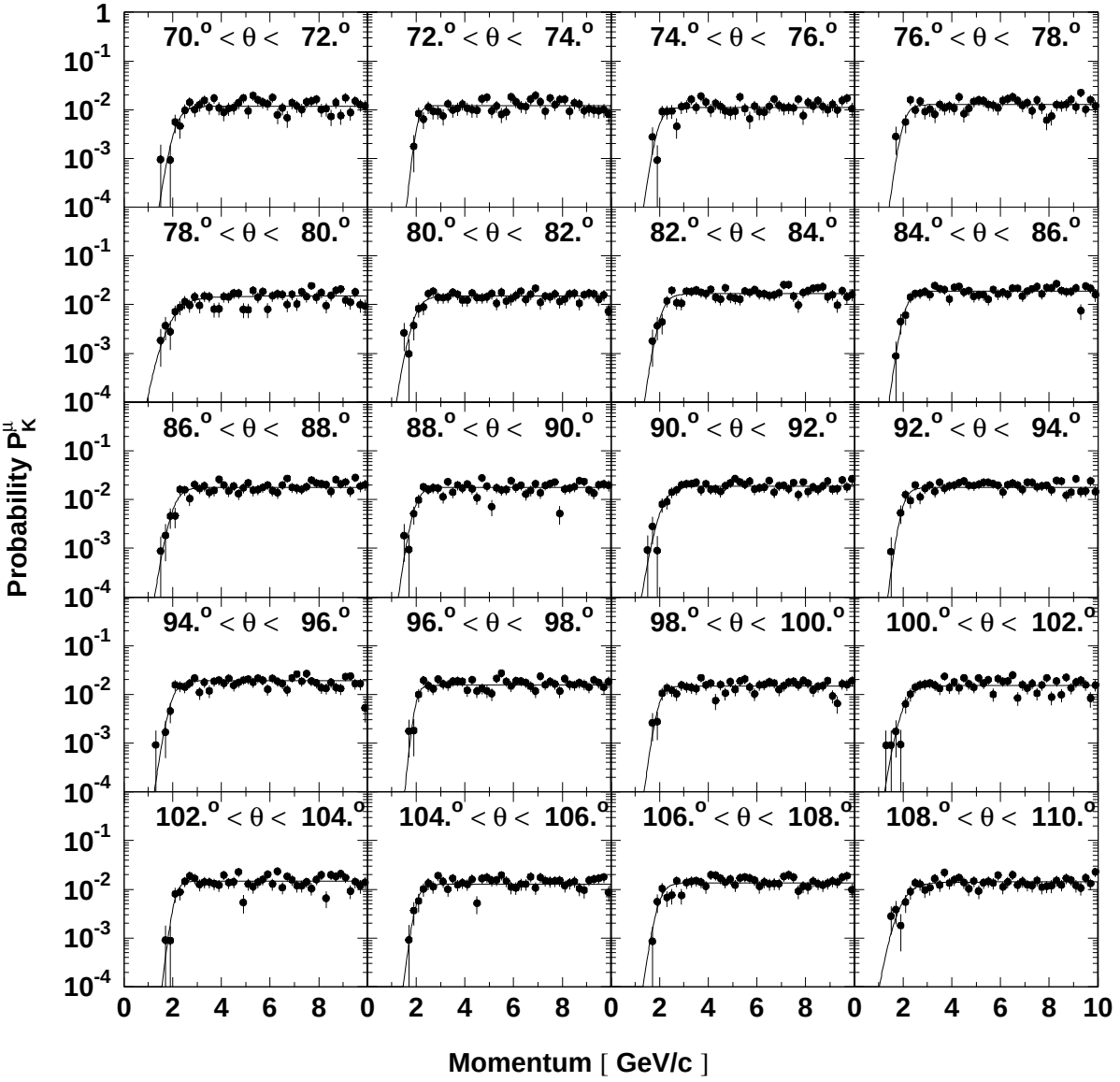

Figure 18: Probability P_K^μ for a kaon to be measured as a muon in the instrumented iron return yoke. The filled points are extracted from a MC simulation, the curves correspond to a fit to the points.

the fake muon candidates in data and in the toy MC, $P_h^\mu(p)$ will be evaluated at the wrong mean angle $<\theta>$ for the following reason. The measured particle flux shows a minimum at $\theta = 90°$. This implies that within each θ-bin, the average is slightly less central compared to a flat particle distribution (as in the toy MC). This leads to less misidentification in reality as the amount of dead material is larger on average. This effect is considerable when the bin size is above 2° and provokes a significant

overestimation of the fake muon background.

In each bin of θ the following threshold function is fitted to the histogram:

$$P_h^\mu(p) = A \cdot \left(\frac{B}{1+(\frac{C}{p})^D} - B + 1\right),$$

where

- A is the plateau value after the threshold, i.e. $P_h^\mu(p) \to A$ for $p \to \infty$.
- B is the plateau value below the threshold relative to A. $(1-B)$ is the scale factor with which A has to be multiplied to obtain $P_h^\mu(0)$, i.e. $P_h^\mu(p) \to A(1-B)$ for $p \to 0$. The fits are constrained to keep $B \in [0,1]$.
- C is the momentum where the probability $P_h^\mu(p)$ is halfway between $P_h^\mu(0)$ and $P_h^\mu(\infty)$, i.e. $P_h^\mu(C) = A \cdot (1 - B/2)$.
- D determines the steepness of the threshold.

The plateau value for $P_h^\mu(p)$ varies with θ but does not exceed $P_\pi^\mu(p,\theta) = 5.7 \cdot 10^{-3}$ in the case of pions. For kaons, $P_K^\mu(p,\theta)$ is significantly higher and reaches values of $P_K^\mu(p,\theta) = 2.0 \cdot 10^{-2}$. Protons (and anti-protons) do not decay and therefore their misidentification probability is lower at $P_p^\mu(p,\theta) < 2.6 \cdot 10^{-3}$.

Particle Type Assignment $f_h^{\pi,K,p}(p)$

In a MC simulation event sample, the identity of a particle in the final state is known, such that a decomposition of the entire hadron sample into different species of particles can be made. Three types of charged particles (and their anti-particles) are sufficient to describe the composition of the hadronic final state: pions, kaons, and protons.

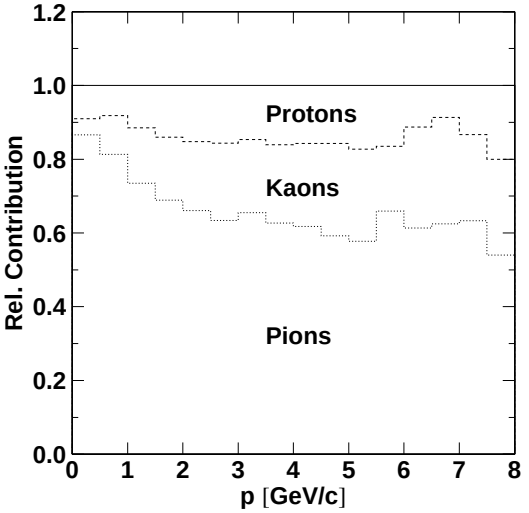

Figure 19: Relative contributions of pions, kaons and protons shown cumulatively. The contributions shown here correspond to the particle sample with polar angle $\theta \in [70°, 80°]$ as measured in the CJC. Some basic track criteria as defined in section 4.1 are applied.

For the extraction of this information, all tracks passing the track quality criteria (to be discussed in section 4.1) are checked for the particle's type. This is done as a function of the particle's momentum in bins of 10° of polar angle. In figure 19 the relative contributions of (charged) pions, kaons, and protons are shown cumulatively. The figure corresponds to particles with polar angle $\theta \in [70°, 80°]$. Similar information has been extracted in the entire acceptance region of $\theta \in [30°, 140°]$.

The assignment of a particular species to a track in data is done as follows: A random number M between 0 and 1 is generated. If this number M is — in the corresponding bins in polar angle and momentum — below the pion-curve, the track is taken to be a pion. If M is above the proton-curve, the particle is chosen to be a proton. If neither is the case, the particle is assigned to be a kaon.

The extrapolation to higher momenta is done by fitting a straight line in the range $p = 5 \ldots 7\,\mathrm{GeV}/c$ to the respective curves. The resulting value is taken for all particles with $p \geq 6\,\mathrm{GeV}/c$.

The generalization to a general hadron sample containing — apart from pions, kaons, and protons — other particle species is not expected to be influenced much by the restriction to only three particle types. On the one hand, all other hadrons contribute only very marginally to the ensemble. On the other hand, nuclear interactions of hadrons show a similar behavior for $p^h > 2\,\mathrm{GeV}/c$, as the region of resonant scattering is typically limited to $p^h \lesssim 1.5\,\mathrm{GeV}/c$.

3.8 Comparison of P_π^μ in Data and MC Simulation

If a pure sample of hadrons can be obtained in data, the misidentification probability P_h^μ can be compared for MC simulation and data. Particle identification with the energy loss dE/dx measured in the CJC is not possible, as a separation between pions and kaons is only feasible for transverse momenta up to $800\,\mathrm{MeV}/c$, well below the threshold for efficient muon detection in the instrumented iron return yoke.

Pions can nevertheless be identified via the reconstruction of the decay of a K_S^0. Kaons can be identified through the decay of $\phi \to K^+K^-$, but the statistics available prohibits a meaningful comparison in this case.

Reconstruction of K_S^0

K^0 decay in 50% as K_S^0, from which a sample of pure pions is obtained by reconstructing the decay

$$K_S^0 \to \pi^+\pi^-.$$

The branching ratio for this decay is 68.6% and the distance of flight for the K_S^0 is $c\tau = 2.68\,\mathrm{cm}$. This leads to secondary vertices, which can be resolved by the CJC.

In order to obtain enough statistics, K_S^0 have to be collected in all data from 1995 – 1997, which corresponds in total to roughly $76 \cdot 10^6$ events. No time-dependence of the misidentification probability can be observed with the (still) meager statistics

available. For a comparison with the MC simulation, roughly 10^6 K_S^0 were generated in events containing five K_S^0 each. The simulation and reconstruction of these toy events was based on the running conditions of 1995.

The analysis is identical for both data and MC simulation. K_S^0 are selected by looking for secondary vertices with two daughter tracks of unlike charge. Both tracks have to pass the basic track cuts as described in section 4.1. The invariant mass of the K_S^0 candidate is calculated by assigning m_π to each of the tracks. Several cuts have to be used in order to suppress the combinatorial background:

- The transverse momentum $p_\perp$ of at least one π candidate must be above $p_\perp^\pi > 2\,\mathrm{GeV}/c$.
- The polar angle of both daughter tracks must be in the range $\theta \in [35°, 130°]$.
- The difference $\Delta d_{ca} = d_{ca}^{\pi^+} - d_{ca}^{\pi^-}$ of the distances of closest approach* of the tracks making up the K_S^0 candidate is required to satisfy

$$|\Delta d_{ca}| > 1 + 10 \cdot e^{-p_\perp^{K_S^0}}\ \mathrm{cm}$$

  The sign of the d_{ca} of a track depends on its charge and therefore large values of $|\Delta d_{ca}|$ result from track pairs with opposite charge at a vertex remote from the primary vertex. The dependency on the transverse momentum counteracts the tendency of large $p_\perp$ to cause small values of $|d_{ca}|$ (*cf.* H1, 1996a).
- The product of the distances of closest approach must be negative, *i.e.* $d_{ca}^{\pi^+} \cdot d_{ca}^{\pi^-} < 0$. The sign of the d_{ca} is equal to that of the z-component of the angular momentum. As the K_S^0 and $\pi^\pm$ mesons are all pseudo-scalar particles, the angular momenta of the two pions have to cancel each other.
- A lifetime cut $c\tau = d/p > 1\,\mathrm{cm}$ is applied to reject false combinations in the vicinity of the primary event vertex.

In addition, the K_S^0 candidate is required not to be a Λ candidate. Assigning the proton mass to the track with the higher transverse momentum, it is requested that the invariant mass $m_{p\pi}$ of the pair satisfies $m_{p\pi} > 1.125\,\mathrm{GeV}$.

The final sample consists of 10'485 K_S^0 candidates selected by a cut on the invariant mass in the region

$$0.45 < m_{\pi\pi} < 0.55.$$

The invariant mass distribution is shown in figure 20.

The mass distributions for both data and MC simulation have been fitted with a Breit-Wigner function, where no background subtraction was done. The mean and width obtained from the fit to the data are

* See Section 4.1 for a short description of the track parameterization at H1.

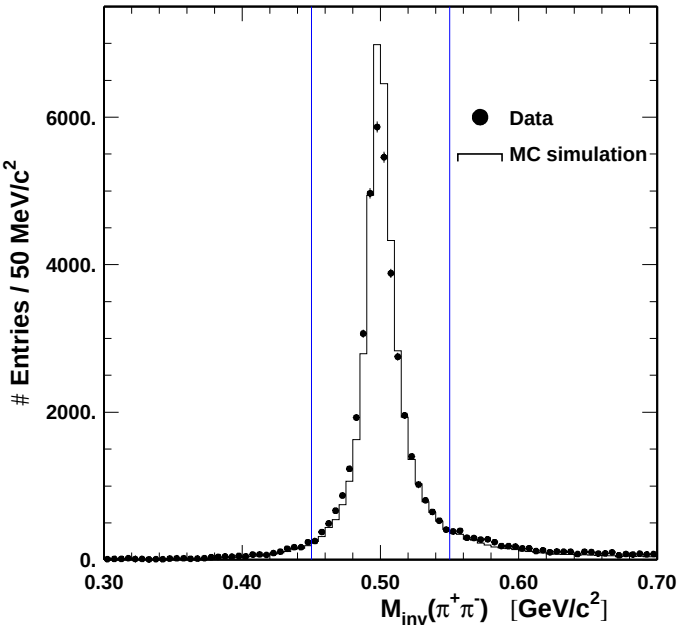

Figure 20: Invariant mass distribution of pion pairs with at least one pion having $p_\perp > 2\,\mathrm{GeV}/c$. The filled points are obtained from data, the solid histogram corresponds to a MC simulation. Both histograms are normalized to the same number of entries. The vertical lines indicate the cuts used to identify K^0_S candidates.

$$<m_{\pi^+\pi^-}>^{DATA} = 499.8\,\mathrm{MeV}/c^2 \qquad (\sigma = 23.04\,\mathrm{MeV}/c^2)$$

and for the MC simulation

$$<m_{\pi^+\pi^-}>^{MC} = 500.3\,\mathrm{MeV}/c^2 \qquad (\sigma = 19.80\,\mathrm{MeV}/c^2).$$

The yield of pions with a transverse momentum $p_\perp > 2\,\mathrm{GeV}/c$ and polar angle $\theta \in [35°, 130°]$ is $n_\pi = 10520$, out of which 39 are identified as muons in the instrumented iron return yoke .

Misidentification Probability for Pions

In figure 21 (a) and (b) the momentum and polar angle distribution of the pion sample in data are shown as full points. The open circles show the spectra for pions identified as muons in the instrumented iron return yoke. The misidentification probability is obtained by dividing the spectrum of the 'muons' by the pion spectrum

$$\mathrm{P}^{\mu}_{\pi}(\mathrm{p}|\theta) = \frac{\#\text{pions identified as muons}}{\#\text{all pions}}$$

both for the momentum and polar angle distribution.

The result is shown in figure 22 as filled points. In addition, the misidentification probability obtained from the MC toy events is shown as open points. The agreement

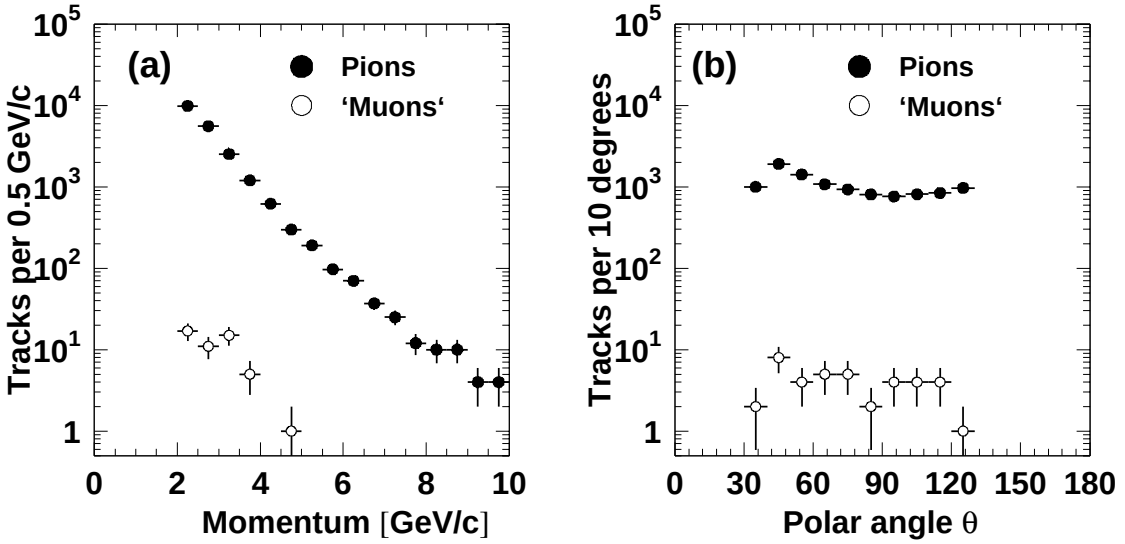

Figure 21: Momentum (a) and polar angle (b) distributions of pions in data. The pions are identified via the decay $K^0_S \to \pi^+\pi^-$. The filled points show the spectrum of the entire pion sample, the open points indicate those pions identified as muons in the instrumented iron return yoke.

between data and MC simulation is very good both for the momentum and the polar angle distributions. This corroborates the assumption that the simulation of the detector is well done as far as the misidentification of pions as muons in the instrumented iron return yoke is concerned.

3.9 Fake Muons in Pure Pion and Kaon Samples

The parameterizations of $P^\mu_\pi(p,\theta)$ and $P^\mu_K(p,\theta)$ can be further verified by comparing the yield of fake muons obtained from a sample of pions and kaons with the estimate based on these probability functions. The misidentification probability $P^\mu_h(p,\theta)$ is assigned as a weight to every hadron h, and the total fake muon yield of these hadrons is obtained by summing the weights of all hadrons. This method allows to obtain the fake muon contribution in *any* distribution, *e.g.* momentum or polar angle spectra.

Estimation of Fake Muons in a Pion Sample

The yield of muons from a pion sample is estimated by assigning $P^\mu_\pi(p,\theta)$ as the weight to every pion and summing all weights of the entire sample. This is done on the sample of pions as obtained from the K^0_S analysis, where the transverse momentum range has been extended to $p_\perp > 1.5\,\mathrm{GeV}/c$. Figure 23 shows the momentum and polar angle distributions. Pions identified as muons are shown as filled points, whereas the estimate based on $P^\mu_\pi(p,\theta)$ is shown as the solid histogram. The estimate provides a very good description of the actual muon yield in both variables. In addition, the

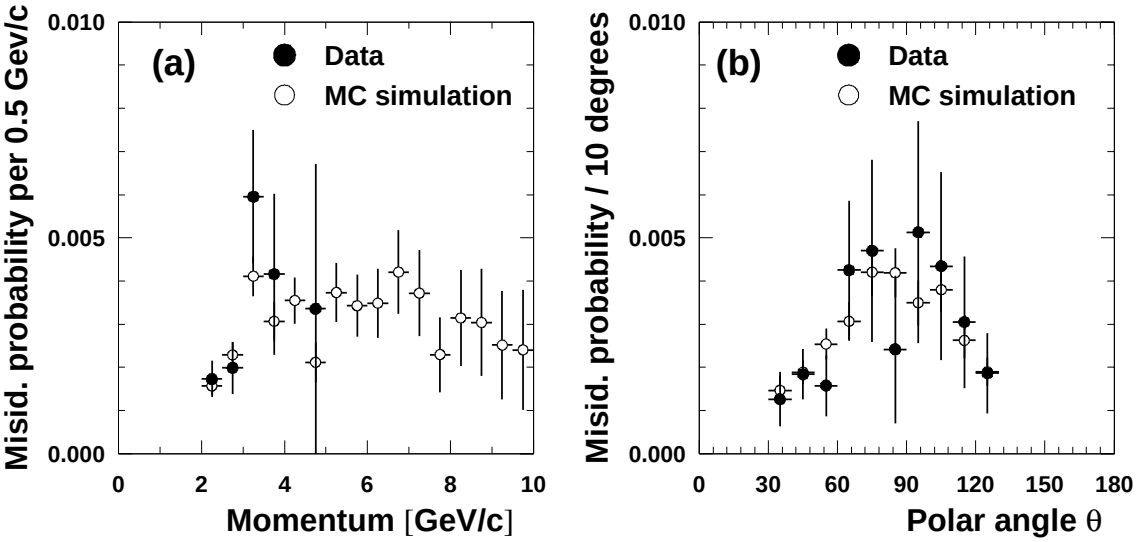

Figure 22: Misidentification probabilities $P_\pi^\mu(p)$ and $P_\pi^\mu(\theta)$ describing the probability that a pion is identified as muon in the instrumented iron return yoke. The filled points show the misidentification probability for pions obtained from data, the open points give the corresponding probability for a MC simulation.

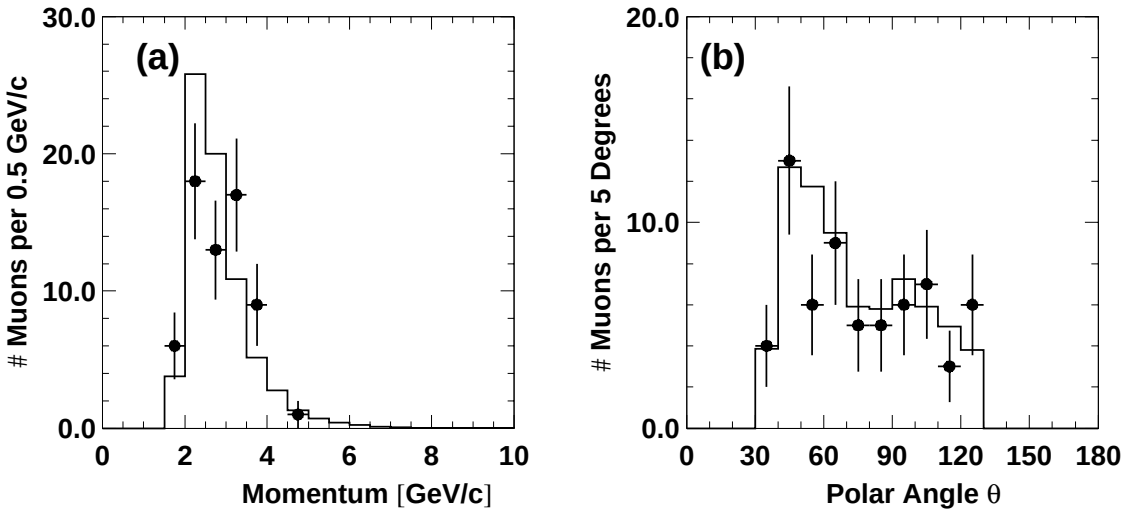

Figure 23: Momentum (a) and polar angle distributions (b) for fake muons found in a pion sample. The pions are identified via the decay $K_S^0 \to \pi^+\pi^-$. The filled points show the muon yield as measured in data. The solid histogram gives the estimate of the muon yield as obtained by assigning $P_\pi^\mu(p,\theta)$ as weight to every pion and summing the weights of the entire pion sample. The measured yield is 64 fake muons, the estimate amounts to 69.8.

absolute normalization is also well estimated: The measured yield is 64 fake muons, while the estimate amounts to 69.8.

Reconstruction of ϕ-candidates

The same comparison has been performed for a kaon sample, identified via the decay $\phi \to K^+K^-$ in elastic ϕ-production. Exactly two tracks of opposite charge were required with polar angles in the range $\theta \in [30°, 140°]$. At least one of the tracks has to have a transverse momentum $p_\perp > 1.5\,\mathrm{GeV}/c$. An invariant mass $m_{K^+K^-}$ is calculated by assigning the kaon mass $m_{K^+} = 0.493\,\mathrm{GeV}/c^2$ to both tracks. ϕ-candidates are selected by requiring the invariant mass to be in the range $m_{K^+K^-} \in [1.01\,\mathrm{GeV}/c^2, 1.03\,\mathrm{GeV}/c^2]$. The mass peak for all elastic ϕ-candidates is shown in figure 24, where the cut on $M_{K^+K^-}$ is indicated by two lines. A total of 1391 ϕ-candidates are found in the peak, resulting in 3566 kaons in the required kinematical region. (No background subtraction is done.)

Estimation of Fake Muons in a Kaon Sample

Although the entire data of 1995 – 1997 has been searched for ϕ-candidates, the statistics available in this case remain very restricted. In figure 25, a comparison of the effective muon yield as measured for the kaon sample with the estimated fake muon yield is shown. Within the large statistical uncertainties, the estimate gives a good description of the fake muons due to the kaon sample. The measured yield is 8 muons, the estimate amounts to 7.8.

3.10 Estimation of Fake Muons in a General Hadron Sample

The particle species for a general track is normally not known in data. This requires the assignment of a particle type prior to the determination of $P_h^\mu(p,\theta)$ and is obtained from $f_h^{\pi,K,p}$. The applicability of this concept is verified as follows.

The fake muons in a light-quark MC simulation event sample are obtained by removing all *genuine* muons. It is exactly the remaining sample of simulated muons which should be reproduced by the estimate of $f_h^{\pi,K,p} \otimes P_h^\mu(p)$. This has been verified by using two different MC simulations:

- 500,000 events at low Q^2 produced by DJANGO 6.0 (Charchula, Schuler, and Spiesberger, 1994).
- 560,000 resolved photoproduction events of PYTHIA 5.7 (Sjöstrand, 1994).

In the following, the comparison based on the PYTHIA sample is described. The results are the same for DJANGO.

The procedure for obtaining the estimate of the fake muon background is as follows. All tracks not identified as muons in neither the LAr calorimeter nor the instrumented iron return yoke are assigned a particle type according to $f_h^{\pi,K,p}$. The misidentification probability $P_h^\mu(p,\theta)$ is calculated accordingly and assigned as weight to the track.

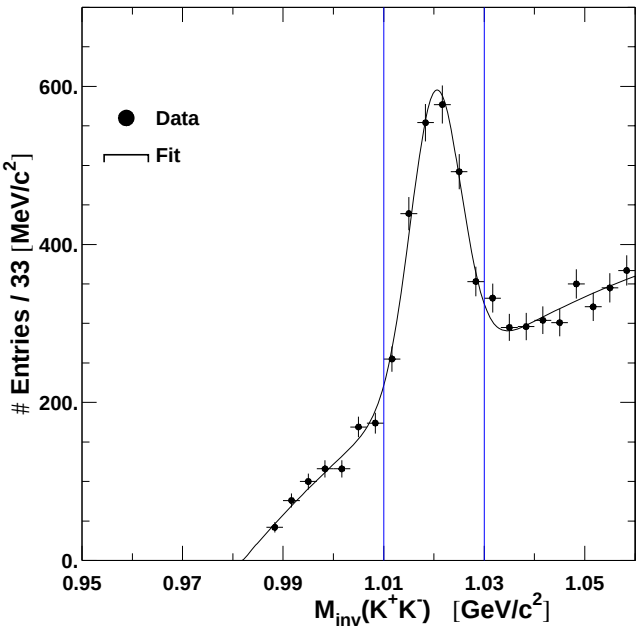

Figure 24: Invariant mass distribution of kaon pairs with at least one kaon having $p_\perp > 1.5\,\mathrm{GeV}/c$. The vertical line indicate the cuts used to select ϕ-candidates around the nominal mass of $m_\phi = 1.02\,\mathrm{GeV}/c^2$.

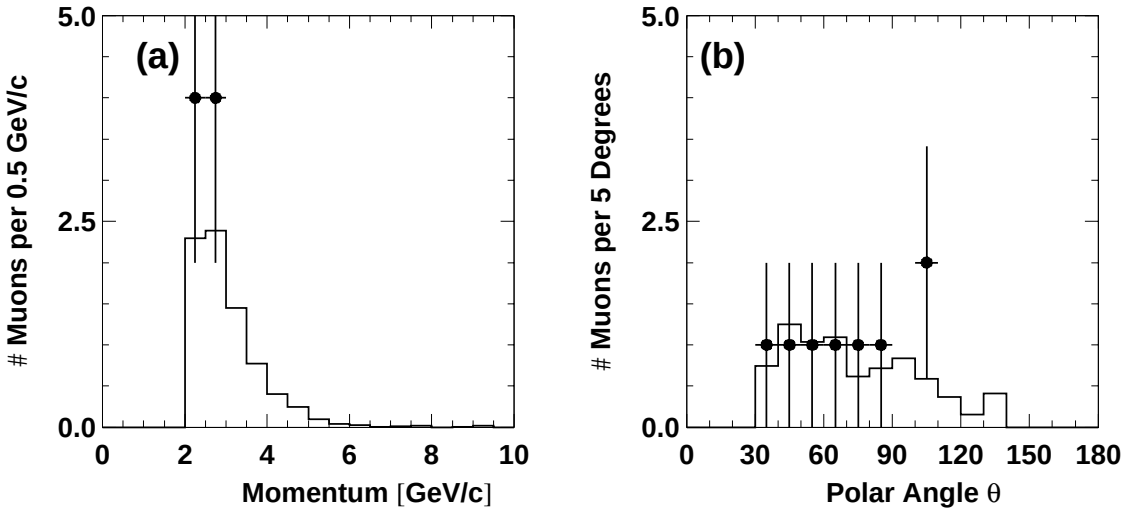

Figure 25: Momentum (a) and polar angle distributions (b) for fake muons found in a kaon sample. The kaons are identified via the decay $\phi \to K^+K^-$. The filled points show the muon yield found in data. The solid histogram gives the estimate of the muon yield as obtained by assigning $P_K^\mu(p,\theta)$ as weight to every kaon and summing over the entire kaon sample. The measured yield is 8 fake muons, the estimate amounts to 7.8.

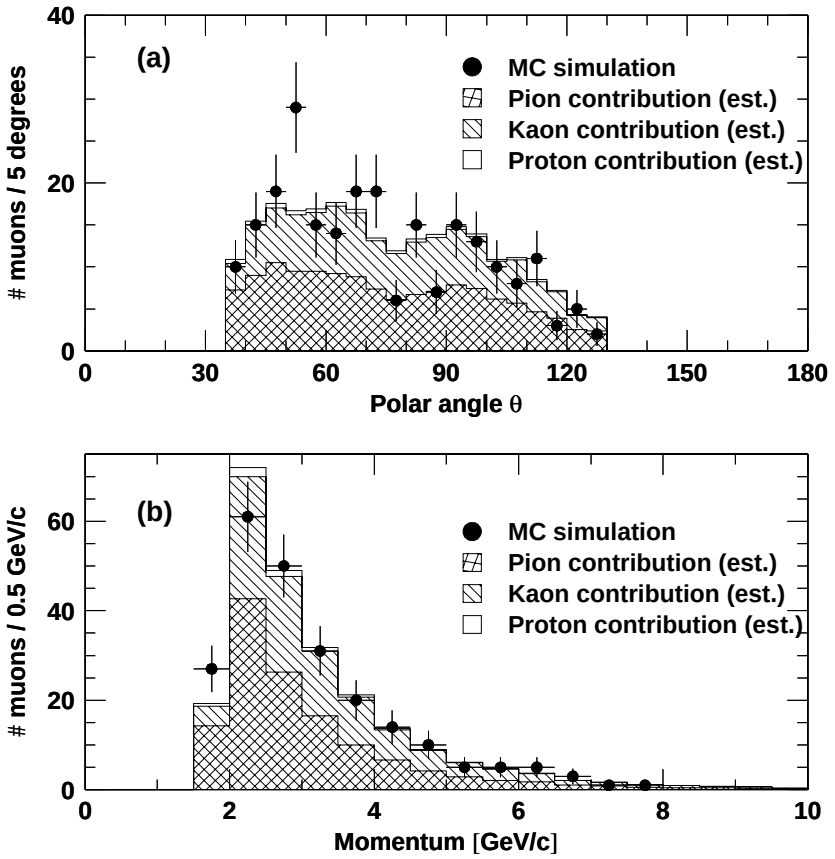

Figure 26: Polar angle (a) and momentum (b) distributions for fake muons in a MC simulation of light-quark events. The *simulated* fake muon distributions are shown as filled points, the *estimate* based on $P_h^{\mu}(p,\theta) \otimes f_h^{\pi,K,p}$ is given as histogram. The contributions of pions, kaons, and protons are separately indicated and added on top of each other. The histogram derived from the estimate is an *absolute prediction* and is seen to describe the simulated fake muons very well. The simulated fake muon sample amounts to 213 muons, the estimate predicts 217.9 muons.

With these weights, the momentum and polar angle distributions for fake muons are produced.

In figure 26 the simulated fake muons are compared to the estimate of fake muons. The estimate is split into the contributions due to pions, kaons, and protons. The agreement between simulation and estimate is seen to be good for both momentum and polar angle distributions. The simulated fake muon sample amounts to 213 muons, the estimate predicts 217.9 muons.

Although kaons constitute less than 25% of the total particle sample, their contribution to the fake muon sample is roughly the same as that for pions. This is due to their significantly larger decay rate. The contribution of protons to the fake muon sample is very small. It is nevertheless important to include protons in $f_h^{\pi,K,p}$, so that the relative composition of the particle sample is determined correctly.

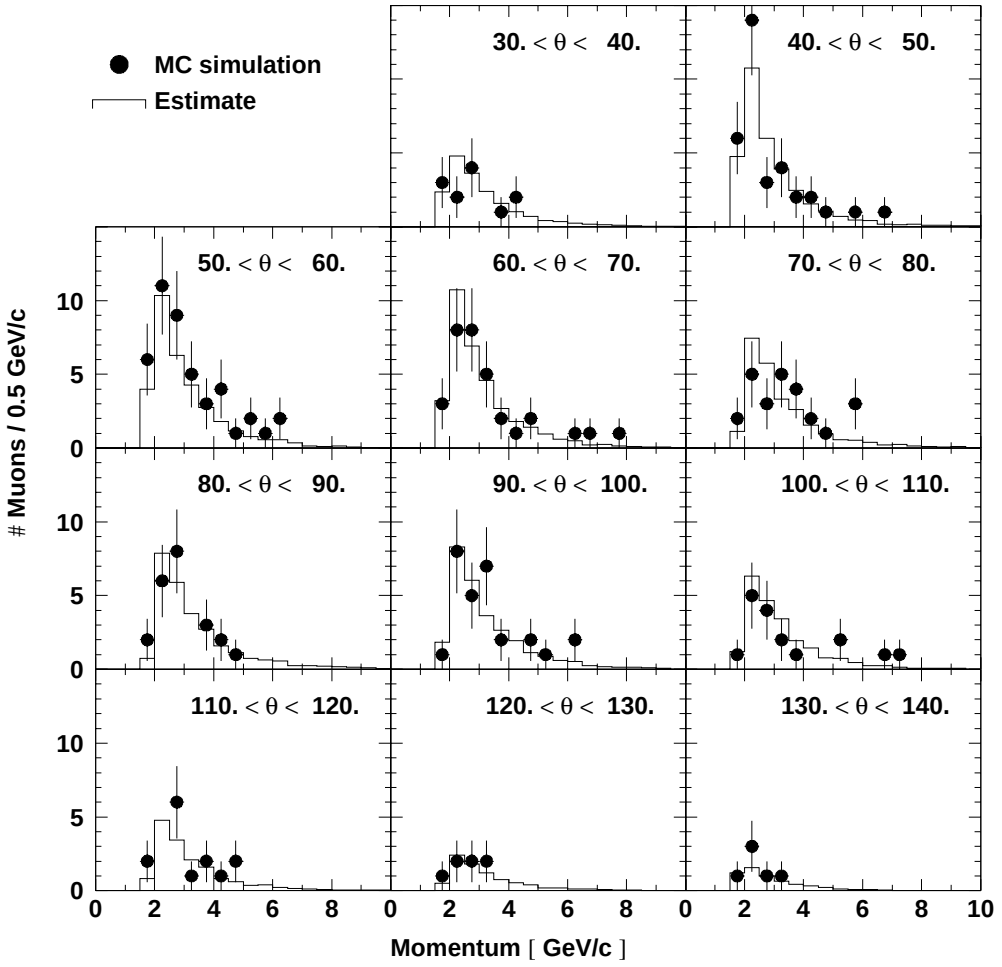

Figure 27: Comparison of the *simulated* muon yield with the *estimate* based on $P_h^{\mu}(p,\theta) \otimes f_h^{\pi,K,p}$ as a function of the particle's momentum in bins of polar angle. The event sample is taken from a MC simulation without genuine muons, *i.e.* all simulated muons are fake muons. The histogram derived from the estimate is an *absolute prediction* and is seen to describe the simulated fake muons very well.

The agreement between simulation and estimate is furthermore very good in a double-differential comparison, as shown in figure 27. In conclusion it can be stated that the estimation based on $P_h^{\mu}(p,\theta) \otimes f_h^{\pi,K,p}$ provides a very good and detailed description of the fake muon background in the barrel region of the instrumented iron return yoke.

Chapter 4

Data Selection

The topic of this chapter is the selection of *signal events* from data taken with the H1 detector in 1995 – 1996. The basic signature of such an event consists of at least two jets with $E_T > 6\,\mathrm{GeV}$ and one muon candidate with $p_\perp > 2\,\mathrm{GeV}/c$ in the central region of the detector. The muon must be part of one of the jets. These events are triggered mainly by the muon track in the instrumented iron return yoke. The estimate of the light-quark contribution to this event sample is obtained from a sample of *background events* characterized by two jets (with $E_T > 6\,\mathrm{GeV}$) and a fake muon candidate with $p_\perp > 2\,\mathrm{GeV}/c$. It is not possible to trigger these background events with the fake muon candidate alone and therefore a jet trigger is used to select this event sample. Apart from these signatures, both signal and background events are required to be "untagged" photoproduction, *i.e.* the angle of the scattered electron is required to be $\theta_e > 177.8°$ and $0.1 < y_{JB} < 0.8$.

This chapter starts with the definition of the track selection and continues with the description of the energy measurement. Jet reconstruction is discussed and the energy flow within jets is compared between data and a MC simulation. The determination of the trigger efficiency is discussed for both signal and background events separately. The luminosity measurement and all applied corrections are described. Both signal and background events must satisfy a number of technical quality criteria described in the final section 4.6, which furthermore summarizes all other cuts imposed on an event.

4.1 Track Selection

Tracks serve a two-fold purpose. First, they are one of the ingredients to build jets. Second, all information on the muon (apart from the identification) is obtained from its track measurement.

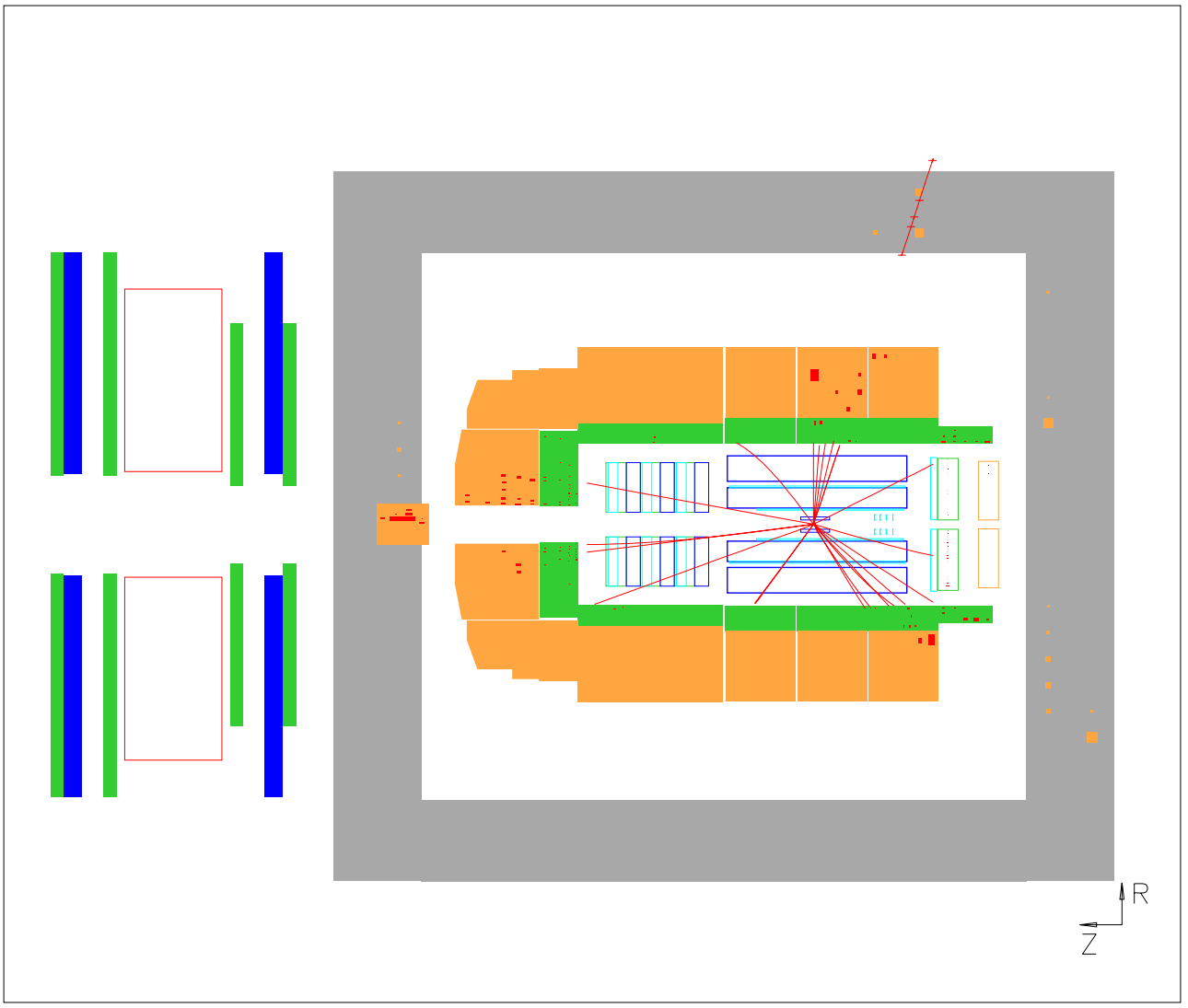

Figure 28: A signal event selected by this analysis and an analysis measuring the photoproduction of $D^{*\pm}$ mesons (Grab and Tsipolitis, 1997). The jet in the lower part of the detector contains a D^{*-}, identified via its decay $D^{*-} \to K^+\pi^-\pi_s^-$. The invariant mass of the D^0 candidate is $m_{K^+\pi^-} = 1.855\,\mathrm{GeV}/c^2$ and the mass difference between the D^{*-} and D^0 candidates is $\Delta m = 0.146\,\mathrm{GeV}$. The jet in the upper half of the detector contains a negatively charged muon μ^- with a transverse momentum of $p_\perp^\mu = 3.24\,\mathrm{GeV}/c$. The transverse momentum of the muon relative to the jet-axis is $p_{\perp,rel}^\mu = 0.98\,\mathrm{GeV}/c$. Charge correlation makes an explanation in terms of $c\overline{c}$-production very unlikely: the $\overline{c}$-quark would fragment into the D^{*-}, and the c-quark could decay semi-leptonically; the decay lepton should carry positive charge, though. The most probable explanation therefore is in terms of $b\overline{b}$-production, where the D^{*-} now is the decay product of the $\overline{b}$-quark and the μ^- originates from a decay of the b-quark. Other explanations include a misidentified muon, or (slightly exotic) $D^0\overline{D}^0$-mixing.

Track Parameterization

Tracks of charged particles measured in the central trackers are characterized by five helix parameters:

- $\pm d_{ca}$, the distance of closest approach. The sign of d_{ca} is given by the sign of the vector product $\mathbf{d}_{ca} \times \mathbf{p}_\perp$, where $\mathbf{d}_{ca}$ is the vector from the primary vertex to the point of closest approach.
- $\kappa = \pm r^{-1}$, the curvature or the inverse radius of the track in the $r\phi$-plane. The value of κ is positive if the direction ϕ coincides with a counter-clockwise propagation along the circle (viewed from the $+z$ direction). The transverse momentum of the particle is determined from κ [cm^{-1}], the magnetic field B [T], and the particle's charge $q \cdot e$ according to

$$p_\perp = \frac{0.3 \cdot q \cdot B}{\kappa}.$$

- ϕ, the azimuth at the point of closest approach, which is the angle between the transverse momentum $\mathbf{p}_\perp$ and the x-axis.
- θ, the polar angle of the momentum and the slope of the helix.
- z_0, the z-position of the point of closest approach.

The parameters κ, ϕ, and d_{ca} are determined by a circle fit to the track hits in the xy-plane, while θ and z_0 result from a linear least-squares fit in the zs-plane, where s is the track length starting with $s = 0$ at the point of closest approach.

For a track traversing both rings of the CJC, a single parameterization is usually sufficient. Due to multiple scattering between the two rings (2% X_0), two sets of parameters are determined for some tracks. The choice between these different fit hypotheses is based on the vertex type of the alternatives. Track hypotheses from the primary event vertex are preferred to hypotheses from secondary vertices, which are in turn preferred to hypotheses fitted to the origin of the co-ordinate system.

Tracks in the forward track detector are only used as input to the jet search algorithm. They do not serve as muon tracks, because muon identification is (in this analysis) limited to the barrel region, whose angular acceptance is completely covered by the CJC. Track parameterization and fitting in the forward track detector is described in detail in (Burke, *et al.*, 1995). All cuts applied to forward and combined tracks are the standard cuts given in (West, 1996).

Tracks with a polar angle of $\theta \in [10°, 25°]$ can be measured in both central and forward trackers and are linked to form "combined tracks". In case of ambiguities for a track hypothesis, combined tracks are preferred to those measured in only one detector, in which case preference to the central track hypotheses is given.

Central Track Cuts

In the following, the track cuts in the central region are given. Tracks associated with a muon candidate are subject to tighter cuts mainly for reasons of a better cosmic rejection.

- The track has to be fitted to a vertex, which can be (in order of preference) either the primary event vertex, a decay vertex of an unstable particle, or the origin of the co-ordinate system.
- The transverse momentum must satisfy $p_{\perp}^{track} > 150\,\mathrm{MeV}/c$. If the track is identified as a muon, the requirement is tightened to $p_{\perp}^{\mu} > 2\,\mathrm{GeV}/c$.
- The distance of closest approach has to be $|d_{ca}| < 2\,\mathrm{cm}$.
- The start radius of the track in the $r\phi$-plane has to be in CJC1, $r_{start} < 50\,\mathrm{cm}$.
- The polar angle is required to be in $\theta \in [20°, 160°]$; for a muon this is restricted to $\theta \in [35°, 130°]$.
- The track length has to be $l_{track} > 10(5)\,\mathrm{cm}$ for polar angles $\theta < 150°(160°)$. Tracks identified as muons are required to have $l_{track}^{\mu} > 25\,\mathrm{cm}$.
- The timing of a muon track is required to be within the nominal time-window of

$$-5\,\mathrm{ns} < \mathrm{t_{CJC}} < 5\,\mathrm{ns}.$$

In a MC simulation, a comparison of the generated and reconstructed momentum is possible. Figure 29 shows the (inverse) transverse momentum resolution obtained for muon tracks. A fit with a Gaussian yields $\sigma = 2.2\%$.

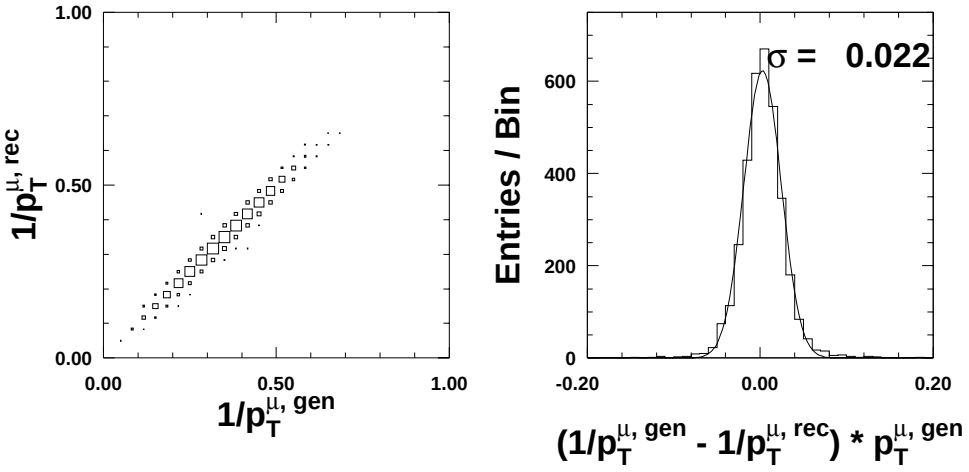

Figure 29: Resolution of the measurement of the (inverse) transverse momentum for muon tracks as obtained from a MC simulation.

4.2 Energy Measurement in the Calorimeters

Charge deposits measured in the calorimeters are converted into cell energies by dedicated software programs in the reconstruction of the event. In addition, noise suppression and corrections for inert material in front of the calorimeters are performed. Finally, the non-compensating nature of the LAr-calorimeter is accounted for. The complete energy measurement is done along the following steps.

Noise Reduction

Electronic noise of the readout electronics leads to an offset value with a width of $\sigma_{noise} \sim 10 - 30\,\mathrm{MeV}$ of the measured energy in each cell. An *online* noise suppression is performed by reading out only cells with $|E_{cell}| > f \cdot \sigma_{noise}$, where $f = 2$ in the BBE- and CB-wheels, $f = 2.5$ in the FB-wheels, and $f = 3$ in the IF-wheels. During the *off-line* reconstruction, only cells with $|E_{cell}| > 4 \cdot \sigma_{noise}$ and directly neighboring cells are kept. The inclusion of cells with negative energies partly compensates positive noise cells. Looking at randomly triggered (empty) events, the total noise contribution to an event at this stage is determined to be $< E^{tot}_{noise} >= 0.1\,\mathrm{GeV}$ with a width of $\sigma^{tot}_{noise} = 0.5\,\mathrm{GeV}$.

Dead Material Corrections

Particles must traverse material not used for the energy measurement before reaching the calorimeters. Nevertheless, energy is lost in this "dead" material. The average energy loss in the inert material is determined from a detailed simulation and added to the cell energy measured in the first layer. In addition to the dead material in front of the calorimeter, there are also inert regions between different calorimeter modules. This energy loss depends on the cell energies at the border of the modules and is added to the relevant cells.

Electro-magnetic and Hadronic Clusters

All cells with $E_{cell} > 0$ passing the noise suppression cuts are grouped into clusters in a two-step procedure. A two-dimensional clustering combines cells of so-called longitudinal calorimeter layers, *i.e.* perpendicular to the beam line in the (forward) IF-wheel and parallel elsewhere. Three-dimensional clusters are formed by combining adjacent two-dimensional clusters. Cells belonging to an electro-magnetic shower are predominantly grouped into a single cluster, while hadronic showers are typically grouped into several clusters. Cells with negative energies are added to clusters as the final step. The cluster is dropped, if its energy is negative after this step. The energies of all isolated cells not assigned to a specific cluster are reset to $E_{iso} = 1\,\mathrm{MeV}$. This leads to a further improvement of the noise suppression. Empty events now show an energy distribution with $< E^{tot}_{noise} >= 0\,\mathrm{GeV}$ and a width of $\sigma^{tot}_{noise} = 0.25\,\mathrm{GeV}$.

A cluster is called *prominent*, if

$$\sqrt{\sum_{i \in cells} \left(\frac{E_i}{\sigma_{noise}}\right)^2} \geq 8.$$

A cluster is classified as *electro-magnetic*, if it is prominent and passes the following criteria:

- The cluster energy satisfies $E_{cl} > 1\,\mathrm{GeV}$.
- At least 80% of the cluster energy is measured in the electro-magnetic part of the calorimeter.
- The cluster is not close to the border of two octants ($\delta\phi > 44\,\mathrm{mrad}$).
- The electron identification probability has to be $P(e) > 99\%$. The determination of $P(e)$ is based on the two quantities

$$\mathrm{EAK0} = \frac{E_{1^{st}\ layer}}{E_{EMC}} \qquad \text{and} \qquad \mathrm{EAH4} = \frac{E_{4\ hottest}}{E_{EMC}},$$

where

$E_{1^{st}\ layer}$ is the energy of the cluster in the first layer,
$E_{4\ hottest}$ is the energy in the four cells with the largest energy,
E_{EMC} is the cluster energy in the electro-magnetic part of the calorimeter.

A cluster is termed *hadronic*, if it is prominent and additionally characterized by the following criteria:

- If the cluster energy is $E_{cl} > 1\,\mathrm{GeV}$ the cluster is required not to be identified as electro-magnetic.
- If $E_{cl} < 1\,\mathrm{GeV}$, the cluster's energy-weighted center-of-gravity (COG) has to lie at least $\lambda_{abs}/3$ within the calorimeter.
- Alternatively, if $E_{cl} < 1\,\mathrm{GeV}$, the cluster is hadronic if $\mathrm{EAK0} \leq 0.2$ or $\mathrm{EAH4} \leq 0.6$.

If a cluster is neither electro-magnetic nor hadronic, it is called *unassigned*.

Neighboring hadronic clusters are combined to form hadronic objects. Unassigned clusters are included in a cluster if they lie in a cylinder (with the primary vertex and the cluster's COG on the cylinder axis) of radius $r = 50\ (25)\,\mathrm{cm}$ for the hadronic (electro-magnetic) part of the calorimeter.

Reweighting of Hadronic Clusters

As the LAr calorimeter is non-compensating, its hadronic clusters have to be reweighted for an optimal energy measurement. Two different methods are used:

- If the energy of the hadronic object is $E_{HO} < 7\,\mathrm{GeV}$, a linear weighting is applied. Electro-magnetic (hadronic) cell energies are scaled with $f = 1.353\ (1.608)$.
- If the energy of the hadronic object is $E_{HO} > 10\,\mathrm{GeV}$, an iterative weighting with exponential functions is done. The weight functions depend on the polar angle, the energy and the volume of the hadronic object.
- Hadronic objects with $7\,\mathrm{GeV} < \mathrm{E_{HO}} < 10\,\mathrm{GeV}$ are reweighted by linearly interpolating between the two methods.

These methods were optimized with test-beam data and a detailed simulation.

Clusters in the Tail Catcher

Due to a bug in the MC simulation of the tail catcher, energy deposits of a penetrating particle are not determined properly in the tail catcher in MC events. Therefore, clusters in the tail catcher associated to an iron track are excluded from the analysis as follows. The inner track is extrapolated as a helix to the inner edge of the calorimeter, where the tangent to the track is determined. The prolongation through the calorimeter and the coil is performed with a straight line. All clusters in the instrumented iron system found within a cylinder of radius $r = 50\,\mathrm{cm}$ around the penetrating track are locked and not used in the analysis.

4.3 Jet Reconstruction

Jets are used in two ways in this analysis. On the one hand, the light quark background can be reduced substantially by requiring two high-energetic jets. On the other hand, jets serve to define the direction of flight of the (heavy) quark.

Jets are built by using all clusters in the calorimeters and tracks in the trackers satisfying the criteria of section 4.1. Dead material in front of the calorimeter limits its acceptance to particles with a momentum $p \gtrsim 350\,\mathrm{MeV}/c$. Charged particles with $p < 350\,\mathrm{MeV}/c$ are included in the jet search by using their tracks. In order to minimize double counting of charged particles with higher energy, tracks with $p > 350\,\mathrm{MeV}/c$ are reweighted such that their momentum is rescaled to $350\,\mathrm{MeV}/c$. The value of $350\,\mathrm{MeV}/c$ has been obtained by optimizing the description of $\sum(E - p_z)$ and $p_\perp$-balance for neutral-current DIS events.

Jet Algorithm

Jets are searched with a *cone algorithm* using clusters and reweighted tracks as particle vectors. The algorithm operates on a grid in the $\eta\phi$-plane with 25 bins in the η range between $\eta = \pm 2.5$. The azimuthal segmentation is 24-fold. In a first step, the transverse momentum of each input vector is filled into the corresponding cell of the grid.

In the next step, cells with a transverse momentum $p_\perp > 100\,\mathrm{MeV}/c$ are used as *initiator cells* being at the center of a cone. The $p_\perp$ of all cells within the cone of radius

$$r = \sqrt{(\eta_{cell} - \eta_{initiator})^2 + (\phi_{cell} - \phi_{initiator})^2}$$

is summed. The variables η and ϕ for both *cell* and *initiator* are calculated at the bin center. If the transverse momentum within the cone is larger than $6\,\mathrm{GeV}/c$, the cone and initiator cell are used as a *jet candidate*. After this has been done for all initiator cells, the jet candidates are sorted in descending order according to their transverse momentum.

Jet building starts with the jet candidate having the highest transverse momentum. Every cell inside its cone is locked and no longer available for further jet candidates. After the first jet has been built, the remaining jet candidates are resummed and sorted.

This is necessary as some of their cells might have been locked during the building of the previous jet (in case of overlap). Jet building continues until no jet candidate remains.

The jet four-momentum p^{Jet} is determined from the E_T-weighted average η and ϕ of all cells within the cone:

$$\begin{aligned} E_T^{Jet} &= \sum_{cells} E_T^i \\ \eta^{Jet} &= \sum_{cells} E_T^i \eta_i / E_T^{Jet} \\ \phi^{Jet} &= \sum_{cells} E_T^i \phi_i / E_T^{Jet} \\ p^{Jet} &= E_T^{Jet} \cdot (\cos\phi^{Jet}, \sin\phi^{Jet}, \sinh\eta^{Jet}, \cosh\eta^{Jet}) \end{aligned}$$

The mass M_{Jet} of the jet is by construction $M_{Jet} = 0$. The direction of the jet is taken to be the thrust axis $\mathbf{T}_{Jet}^{w/o\ \mu}$ of all objects (except the muon) pertaining to the jet. The thrust axis is the direction maximizing the thrust

$$T = max \frac{\sum_i |p_L^i|}{\sum_i |p^i|}, \tag{6}$$

where p_L^i is the projection of the momentum of object i onto the thrust axis.

Jet Parton Correlations

In the following we compare kinematic quantities of the reconstructed jet with those of the generated heavy quark. The quark is taken directly after production and before final state radiation. The direction of the jet is taken to be the thrust axis as defined in the previous subsection.

Figure 30 shows the correlation and resolution of the polar and azimuthal angle between the heavy quark and jet. Both variables show a very strong correlation and good resolution.

Comparing the generated quark momentum with the reconstructed jet momentum shows a less satisfying picture (*cf.* figure 31). This situation is due to

- some overestimation of the jet-energy with the combination of clusters and reweighted tracks;
- energy flow not associated with the hard sub-process, *i.e.* caused by the soft underlying event;
- final state radiation;
- resolution of the calorimeters regarding the measurement of hadronic energy.

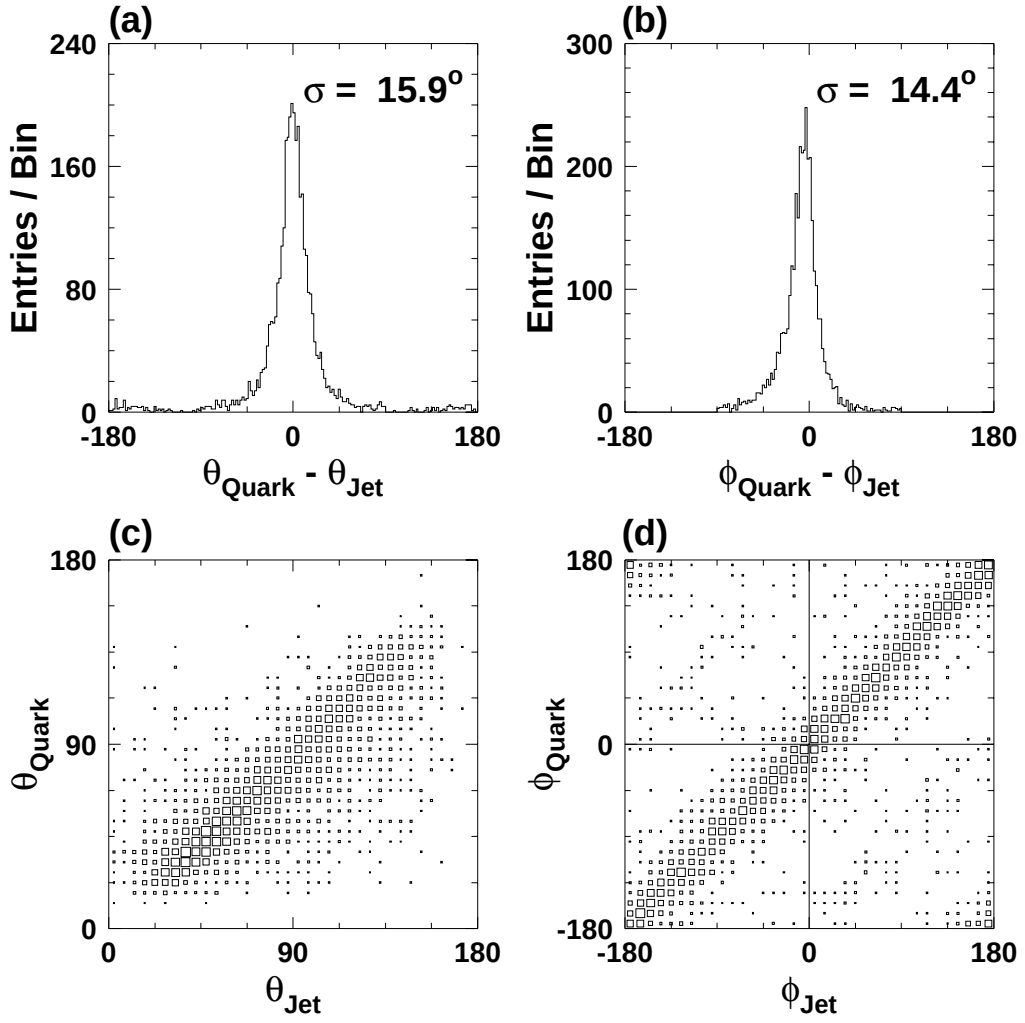

Figure 30: Comparison of the generated parton and the reconstructed jet. (a) and (c) show the resolution and correlation of the polar angle, (b) and (d) of the azimuthal angle. The jet axis is taken as the jet thrust axis (see text for details).

Energy Flow within Charm-Jets

The subsequent analysis relies on the fact that muons from decays of b-quarks have a larger transverse momentum $p^{\mu}_{\perp,rel}$ relative to the quark's direction of flight than muons from c-decays. If (hard) gluon radiation altered the direction of flight of the quark without adequate modeling in the MC simulation, the $p^{\mu}_{\perp,rel}$ distribution might be distorted and not a good variable for fitting. Here a comparison of the energy flow within jets is presented for:

- A MC simulation event sample with generated charm quarks, and
- a data sample containing identified D^* candidates. DIS events have been selected by requiring a detected electron in the Spacal ($Q^2 > 1\,\mathrm{GeV}^2$). The D^* candidate is identified via its decay $D^{*\pm} \to K^{\mp}\pi^{\pm}\pi^{\pm}_s$. In order to increase the signal-to-background ratio to 4:1, the transverse momentum of the D^* candidate has to

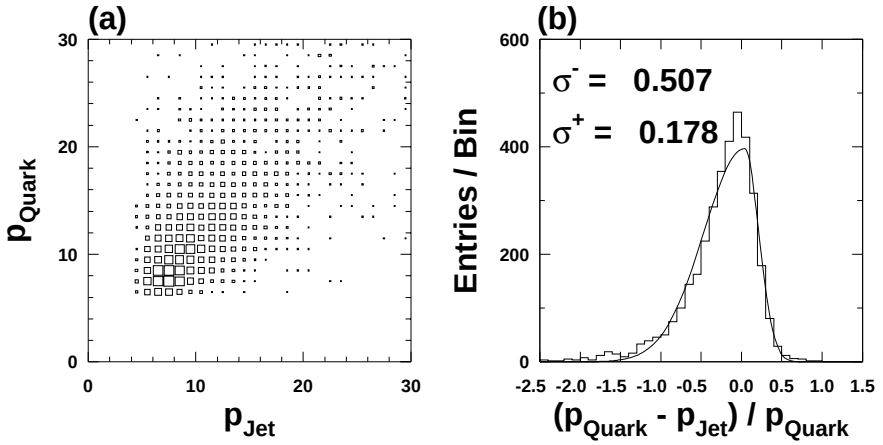

Figure 31: Comparison of the generated quark momentum and the reconstructed jet momentum. (a) shows the correlation, (b) shows the resolution fitted with a bifurcated Gaussian with a width on the right of σ^+ and on the left of σ^-.

satisfy $p_\perp^{D^*} > 1.5\,\mathrm{GeV}/c$.

Figure 32 shows the fractional energy flow within a jet as a function of the distance to the jet thrust axis. (The maximum radial distance between a jet axis and a particle belonging to the jet can be larger than $d = 1$, as only the center of the containing cells are required to have $d < 1$.) It is seen that the MC simulation provides a very good description of the energy flow within jets, at least for events containing charm quarks.

4.4 Trigger Efficiencies

H1 employs a multi-level trigger concept to reduce the rate with which events are written to tape. The probability that an interesting event survives the trigger selection has to be determined for each level. This trigger efficiency ϵ_{tr} can be obtained in several ways:

- If the simulation of the trigger system is sufficiently precise, ϵ_{tr} can be extracted from a MC simulation. Interesting events are either "triggered" or not, but they are found in the same event sample. The trigger efficiency is then determined as

$$\epsilon_{tr} = \frac{\#\text{triggered events}}{\#\text{all events}}$$

  The simulation of the L1 trigger used for both signal and background events is not reliably implemented for the years 1995 and 1996.
- The extraction of ϵ_{tr} directly from data is more subtle, as events which did not set a subtrigger on L1 are lost permanently and completely (or to 99% in the case of the triggers on L4 and L5). This loss can be circumvented by selecting an event sample triggered by a bias-free reference subtrigger. The following subsection contains a detailed description.

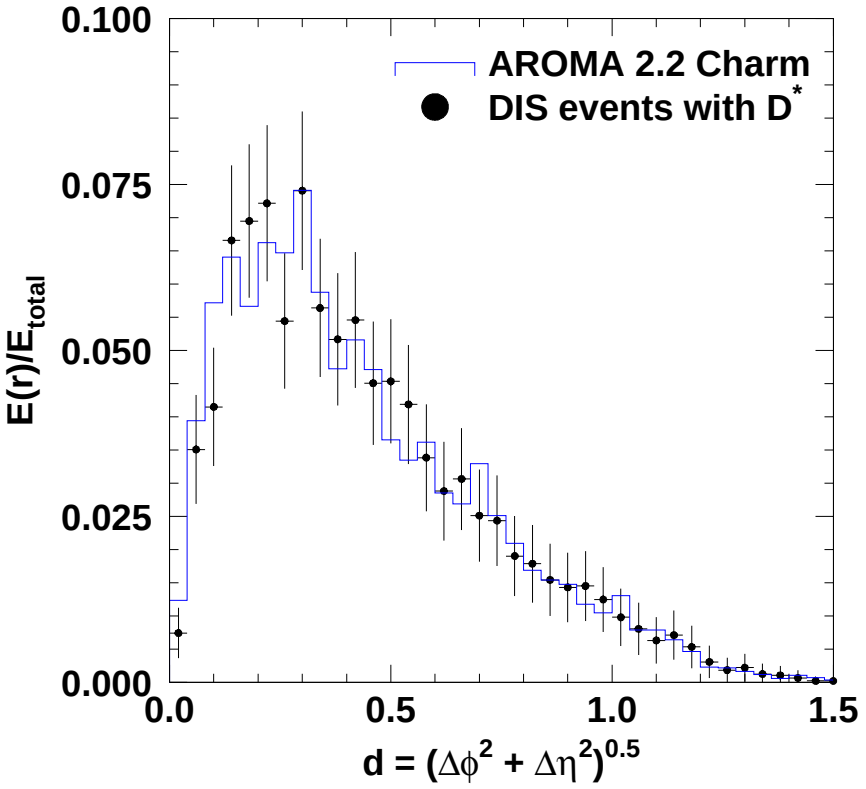

Figure 32: Fractional energy flow within jets as a function of the distance to the jet thrust axis. The data points correspond to DIS events with an identified D^* candidate as specified in the text. The histogram is obtained from a MC simulation where only charm quarks are produced in the hard subprocess.

Determination of the Trigger Efficiency from Data

If the subtrigger efficiency is to be determined from data, a problem immediately arises as the overall sample is not known. (Events which do not set an L1 subtrigger are lost.) Using a reference subtrigger, it is nevertheless possible to determine ϵ_{tr}. Let

$$\begin{aligned} N_1 &= N \cdot \epsilon_1 \\ N_2 &= N \cdot \epsilon_2 \\ N_{12} &= N \cdot \epsilon_{12} \end{aligned}$$

be the number of events — out of the (unknown) overall sample N — which have a subtrigger condition 1, 2, 1&2 set. The corresponding subtrigger efficiencies are denoted by ϵ_1, ϵ_2, and ϵ_{12}, respectively. The last equation can be rewritten as

$$\begin{aligned} N_{12} &= N_1 \cdot \tilde{\epsilon}_2 \\ &= N_2 \cdot \tilde{\epsilon}_1 , \end{aligned}$$

where $\tilde{\epsilon}_1(\tilde{\epsilon}_2)$ is the subtrigger efficiency for subtrigger 1(2) *provided that subtrigger 2(1) is set.* If the two subtriggers 1 and 2 are independent of each other and if they do not select a biased event sample, then $\epsilon_1 = \tilde{\epsilon}_1$ (and $\epsilon_2 = \tilde{\epsilon}_2$).

If a bias-free reference subtrigger 1 is found, the efficiency of subtrigger 2 is given by

$$\epsilon_2 = \tilde{\epsilon}_2 = \frac{N_{12}}{N_1},$$

where the first equality holds by virtue of the (assumed) absence of any bias in the event sample N_1.

The selection of a truly bias-free reference subtrigger is non-trivial. In order to minimize any hidden bias, several reference triggers are used in this analysis and the resulting spread of the subtrigger efficiency is used as the systematic uncertainty. As most subtriggers are subject to prescaling (which is accounted for in the luminosity measurement), the reference subtrigger 1 should be demanded on the "actual" level (after prescaling), while the "raw" (before prescaling) subtrigger 2 is used for the determination of the overlap sample N_{12}.

The trigger situation in 1995 turned out to be very complex due to the incorporation of new sub-detectors and the desire to take data with them. Many changes were made to the trigger setup resulting in fluctuations of the trigger efficiencies. This is accounted for in the rather large systematic uncertainties. In 1996, the situation showed a much more stable environment allowing a precise determination of trigger efficiencies.

The determination of a trigger efficiency always implies the definition of a final data sample, which will be described in full detail in section 4.6. This data sample consists of signal and background events, which are triggered by two different subtriggers (S19 for signal and S56 for background events, respectively).

L1 Trigger Efficiency for Signal Events

Signal events carry as characteristic signature a muon and two jets as defined in sections 4.1 and 4.3, respectively. They are triggered mainly by the muon with subtrigger S19, which is basically a muon-trigger for the central region. More specifically, it is a logical AND of the following information provided by several subsystems triggers*:

- MU_BAR provided by the central Muon Trigger: At least two of the trigger layers within one module of the instrumented iron return yoke have to be set in coincidence. This implies a penetrating particle with $p_\perp \gtrsim 1.5\,\mathrm{GeV}/c$.
- Drift-chamber $r\phi$-trigger: The trigger element provided by this trigger was tightened during the running period. Because of the fact that at least one jet is required in the central region, these changes do not influence the trigger efficiency beyond the systematic uncertainty.

* A remark about the notation is due. '&&' indicates logical AND, '||' logical OR, '!' logical NOT, '==' logical equality.

The trigger elements required were (changing definitions are indicated by the run-range in brackets)

- DCRPh_Ta, at least one charged particle with $p_\perp \gtrsim 400\,\mathrm{MeV}/c$ in the central region. (121970 – 124254)
- DCRPh_Ta&&DCRPh_THig&&DCRPh_TNeg, at least one negatively charged particle with transverse momentum $p_\perp \gtrsim 400\,\mathrm{MeV}/c$ and at least one charged particle with transverse momentum $p_\perp \gtrsim 800\,\mathrm{MeV}/c$ in the central region. (124255 – 131045)
- DCRPh_Tc&&DCRPh_TNeg&&DCRPh_THig, at least one negatively charged particle with $p_\perp \gtrsim 400\,\mathrm{MeV}/c$, at least one charged particle with transverse momentum $p_\perp \gtrsim 800\,\mathrm{MeV}/c$, and at least 3 charged particles with transverse momentum $p_\perp \gtrsim 400\,\mathrm{MeV}/c$ in the central region. (151600 – 171156)

- The $zVtx$-trigger employs signals of the central and forward proportional chambers to derive the z-position of the vertex. Activated pads of the inner and outer or forward proportional chambers are linked to form *rays*, which are extrapolated to the beam line, where the intersection is filled into a histogram with 16 bins. All active rays are grouped into *big-rays*, showing identical segmentation in polar angle as big-towers of the LAr calorimeter (see below).
  - zVtx_small||zVtx_sig1. The first condition is set if the number of entries N_{max} in the bin with most entries is in the range $1 < N_{max} < 5$ and if the remaining bins contain at most $N_{rest} < 3$ further entries. The second condition requires a "significant" peak in the histogram, defined by $(N_{max} - N_{rest}/15)/\sqrt{N_{max}} > 1.5$. (121970 – 131045)
  - zVtx_sig1&&(((zVtx_mul==0)||(zVtx_mul==3))||zVtx_sig1). The multiplicity requirements in this statement make sure that no bias with respect to the charged track multiplicity is introduced by requiring an OR of low and high multiplicity trigger elements. (121970 – 131045)

- Timing information provided by the $zVtx$-trigger and the forward proportional chambers:
  - zVtx_T0||FwdRay_T0. A minimum of one ray is required either in the central or the forward region. (121970 – 171156)

- Timing information provided by the ToF-system, the veto-walls, and — for 1996 — the Spacal:
  - FToF_IA||!FToF_BG imply a hit either during the interaction time window or not in the background time window in the forward time-of-flight system. The FToF is located within the toroidal magnet of the forward muon spectrometer and consists of scintillators. (121970 – 171156)
  - !BToF_BG &&!CIP_Backward. The first condition implies that no hit is detected in the backward time-of-flight system during the background time window. If more than three sectors in the backward part of the CIP ($z < -1\,\mathrm{m}$) are hit, CIP_Backward is set. (121970 – 124636)

- !BToF_BG &&!VETO_Inner_BG&&!VETO_Outer_BG implies — apart from the above mentioned BToF-condition — that no hits were registered in the inner and outer veto-walls in the background time-window. (124637 – 167408)
- !BToF_BG&&!VETO_Inner_BG&&!VETO_Outer_BG&&!SPCLh_AToF_E_1 has as the only new requirement a cut on the total energy measured in the hadronic part of the Spacal in the background time-window. (167409 – 171156)

The trigger efficiency for S19 is determined by using the following subtriggers as reference triggers:

- S2, which is basically a Spacal-trigger requiring a scattered electron candidate of medium energy ($E'_e > 2\,\mathrm{GeV}$).
- S7, which was for 1995 a low-threshold ($E'_e > 0.5\,\mathrm{GeV}$) Spacal-trigger with a minimal track requirement in the central region. In 1996, S7 was changed to a high-threshold ($E'_e > 5.5\,\mathrm{GeV}$) Spacal-trigger without any track requirements.
- S83, which is a subtrigger using the electron tagger ET33 in conjunction with tracks in the central region.

Figure 33 shows the trigger efficiency of S19 as a function of transverse momentum of the muon and the run-number. It is seen that ϵ_{S19} is flat to a good approximation with respect to both variables. The same is also true for the dependence on y_{JB}. The resulting mean efficiency for S19 is determined to be

$$\epsilon_{S19} = 72.0 \pm 5.1\% \qquad (1995)$$
$$\epsilon_{S19} = 85.5 \pm 1.6\% \qquad (1996).$$

The uncertainty quoted is half of the variation of ϵ_{S19}, when different reference triggers (as given above) are chosen.

L1 Trigger Efficiency for Background Events

Background events are characterized by two jets and a fake muon candidate as defined in section 4.6. They are triggered with subtrigger S56, which is basically a jet-trigger with emphasis on trigger elements provided by the LAr-calorimeter. More specifically, it consists of the logical AND of the following information (changes during the run-period are indicated in brackets):

- LAr-calorimeter trigger: All cells of the LAr calorimeter are grouped into *towers* pointing towards the nominal interaction vertex. These towers partition the calorimeter into 23 bins in polar angle and 32 azimuthal bins. A tower is activated by an energy deposition of $E \gtrsim 1\,\mathrm{GeV}$. Up to four of these towers can be combined to form *big-towers*.
  - (LAr_CB + LAr_FB) is the sum of all big-towers in the central and forward barrel. The energy deposition has to be $E \gtrsim 4.5\,\mathrm{GeV}$ in the (central) CB and $E \gtrsim 2.5\,\mathrm{GeV}$ in the (forward) FB. (121970 – 171156)

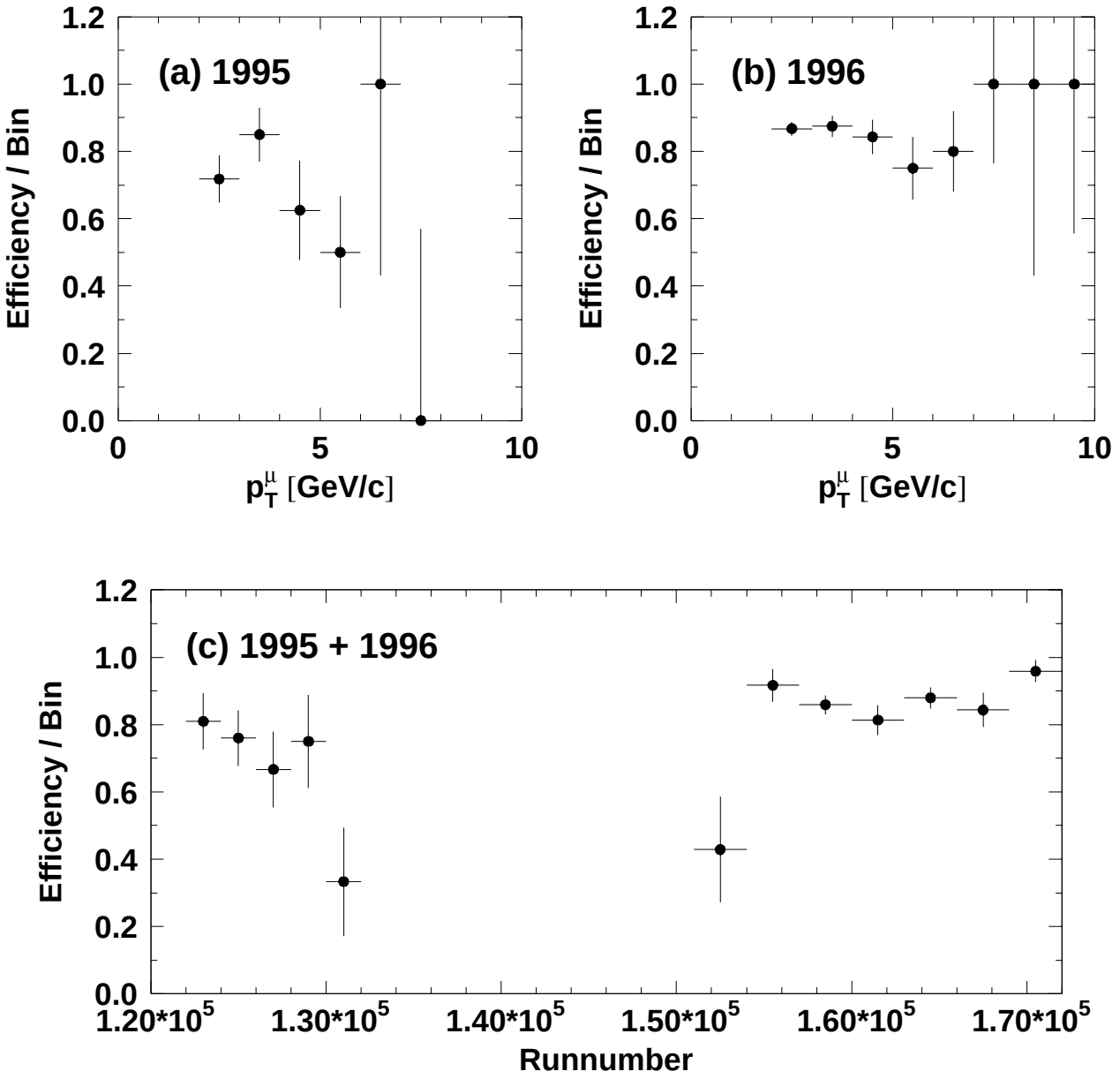

Figure 33: Trigger efficiency for S19 as a function of the muon transverse momentum for 1995 (a) and 1996 (b). The variation of ϵ_{S19} over the run-period is shown in (c) for both 1995 and 1996.

  - LAr_BR provides the spatial coincidence between a big-ray of the $zVtx$-trigger and a big-tower with energy $E > 1.5\,\mathrm{GeV}$ in the LAr calorimeter. (121970 – 171156)

- A minimal track condition from the drift-chamber $r\phi$-trigger:
  - DCRPh_TNeg, requiring a negatively charged particle with $p_\perp \gtrsim 400\,\mathrm{MeV}/c$ in the central region. (121970 – 171156)

- Timing information provided by a plethora of sub-detectors:
  - (SPCLe_IET>0)||!SPCLe_AToF_Cl1, which is basically a weak timing condition based on energy deposition measured in the electro-magnetic Spacal. (125075 – 131045)
  - !BTof_BG&&!VETO_inner_BG&&!VETO_outer_BG implies that no hits were registered in the inner and outer veto-walls in the background time-window. In addition, no hit is detected in the backward time-of-flight system during the background time window. (121970 – 171156)
  - zVtx_T0 indicates at least one ray found in the central region by the z-vertex trigger. (121970 – 171156)
  - FToF_IA || !FToF_BG implies a hit either during the interaction time window or not in the background time window in the forward time-of-flight system. (121970 – 171156)
  - !SPCLe_AToF_Etot && SPCLe_ToF_Etot is a timing requirement provided by the electro-magnetic Spacal, where the total amount of energy has to be in the interaction time-window or not in the background time-window. (121970 – 171156)
  - !RZ_non-vtx. The rz-trigger employs signals of the CIZ and COZ drift-chambers and builds a histogram analogous to the $zVtx$-trigger. The vertex histogram is centered around the nominal interaction point ($z = \pm 25\,\mathrm{cm}$), the background-sum is defined as the overflow bin with $z < -25\,\mathrm{cm}$. RZ_non-vtx is derived by applying a cut on the ratio of the number of entries in the most populated bin in the signal histogram and the background-sum. (125075 – 171156)
  - PToF_IA||!PTof_BG derived from the Plug-calorimeter. (126572 – 171156)

The trigger efficiency for S56 is determined by using the following subtriggers as reference triggers:

- A variety of Spacal triggers composed of a logical OR of all threshold triggers, *i.e.* the energy of the scattered electron candidate has to satisfy $E'_e > 0.5, 2.0, 5.5\,\mathrm{GeV}$.
- S83 and S84, which are subtriggers using some minimal track criteria in the central region in conjunction with the electron taggers ET33 and ET44.
- S19, the subtrigger for signal events as described in the previous subsection.

Due to the rather strong calorimetric requirements, S56 shows a strong dependence on the transverse energy of the central jet as shown in figures 34 and 35. The trigger

efficiency shows some variation over the run-period in 1995, but is very stable for 1996. There is no dependence on y_{JB}. The mean trigger efficiency for S56 is determined to be

$$\begin{aligned} \epsilon_{S56} &= 46.9 \pm 10.6\% \qquad (1995) \\ \epsilon_{S56} &= 56.8 \pm \ 3.7\% \qquad (1996). \end{aligned}$$

The uncertainty quoted is half of the variation of ϵ_{S56}, when different reference triggers (as given above) are chosen.

L4 Trigger Efficiency for Signal and Background Events

The decision of the online filter farm is based on *(i)* L1 trigger information, *(ii)* raw event data, and *(iii)* reconstructed event data. The main task in the years 1995 and 1996 was to *reject* background events along the following lines:

- Beam-gas or beam-wall events with interaction vertices outside the nominal interaction region are removed by requiring

$$|z_{\mathrm{Vertex}}| < 50\,\mathrm{cm}.$$

- For Beam-gas or beam-wall events originating within the nominal interaction region a few primordial track cuts have to be defined first:

$$\begin{aligned} |d_{ca}| &< 2\,\mathrm{cm} \\ p_\perp &> 200\,\mathrm{MeV}/c \end{aligned} \qquad \begin{aligned} N_{CJC} &> 15 \\ r_{start} &< 30\,\mathrm{cm} \\ l_{track} &> 15\,\mathrm{cm}. \end{aligned}$$

  Proton-induced background events show a markedly different energy flow than genuine γp events which is exploited by the following cuts using tracks as defined above and calorimeter cells (tagging background):

$$\begin{aligned} \left(\frac{y_{JB}}{0.06}\right)^2 + \left(\frac{1-(\sum p_z/\sum p)}{0.15}\right)^2 &< 1.0 \\ \sum (E - p_z) &< 1.5 \\ \sum \frac{(E+p_z)}{2E} &< 0.2 \\ \sum p_z/E &> 0. \end{aligned}$$

- Noise in the L1 subsystem triggers is suppressed by the trigger-verification, where the intended signature responsible for a subtrigger is actually checked. This implies for S19 that
  - the track requirements for the DC-$r\phi$ have to be fulfilled, *i.e.* $1-3$ particles (with at least one being negatively charged or high-$p_\perp$) have to be measured in the CJC;

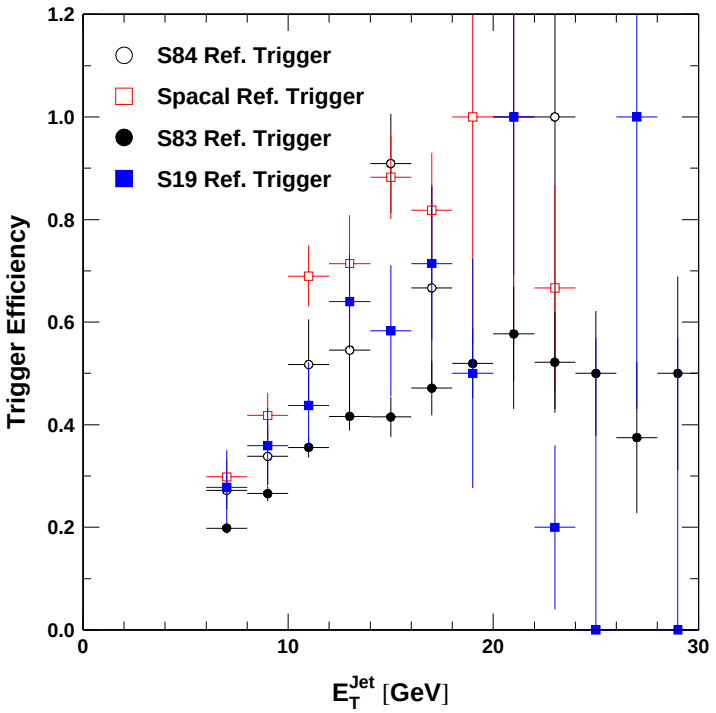

Figure 34: Trigger efficiency for S56 in 1995 as a function of the transverse energy of the jet containing the fake muon candidate. The dependence of the trigger efficiency on different reference subtriggers is shown.

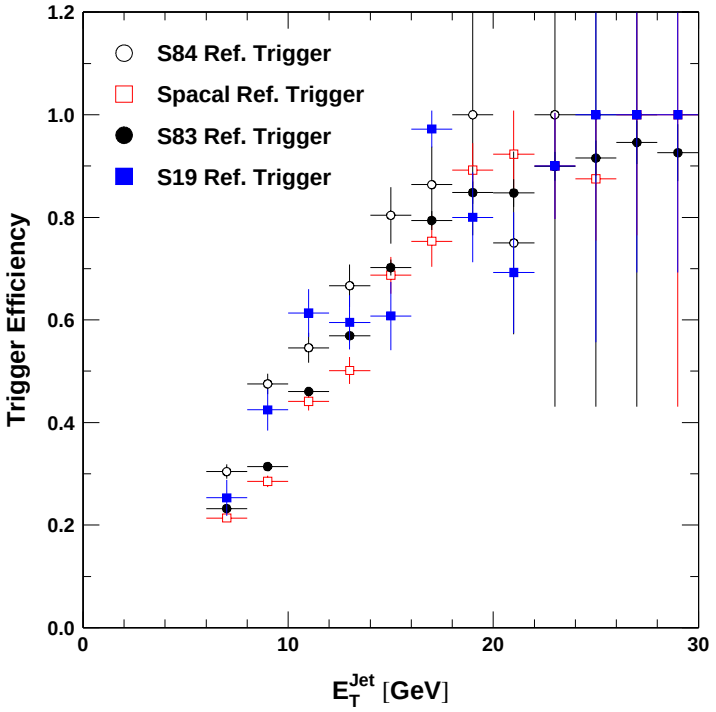

Figure 35: Trigger efficiency for S56 in 1996 as a function of the transverse energy of the jet containing the fake muon candidate. The dependence of the trigger efficiency on different reference subtriggers is shown.

- at least one iron track with basic criteria as defined in section 3.2 is measured.

- Cosmic ray induced events are rejected as discussed in section 3.5.

The trigger efficiency of L4 is estimated by analyzing events *rejected* by L4. As only 1% of the rejected events are written to tape, the estimate for $\epsilon_{\mathrm{L4}}^{\mathrm{Signal}}$ would be rather low with the statistics available. Therefore, the cuts are loosened ($N_{Jet} \geq 1$, $p_{\perp}^{\mu} > 1.5\,\mathrm{GeV}/c$) such that a total of 3062 signal events pass the selection. As no single event is found in the L4-rejected event sample, this can be translated into a lower limit on the trigger efficiency of $\epsilon_{\mathrm{L4}}^{\mathrm{Signal}} > 92.5\%$ at the 90% C.L. For the subsequent analysis, we take $\epsilon_{\mathrm{L4}}^{\mathrm{Signal}} = 100\%$.

Statistics are better for background events, where a total of 52588 events (standard cuts) are to be compared to no event found in the rejected event sample. This implies (at 90% C.L.) a lower limit of $\epsilon_{\mathrm{L4}}^{\mathrm{Bg}} > 99.6\%$, which is taken as $\epsilon_{\mathrm{L4}}^{\mathrm{Bg}} = 100\%$ for the subsequent analysis.

L5 Trigger Efficiency for Signal and Background Events

The reconstruction on L5 is not a trigger in the proper sense but only a classification. It employs the full detector information and is based on kinematic and topological quantities. For this analysis, events belonging to the "inclusive muon" class were used. This implies the following criteria:

- All cuts already done on L4 are applied with the full CJC-reconstruction and tighter cuts.
- At least one iron track linked to an inner track according to the criteria defined in section 3.3.
- Cosmic ray induced events are rejected as discussed in section 3.5.

The inefficiency of L5 is estimated by analyzing events rejected by L5 and is found to be negligible for both signal and background events.

4.5 Luminosity

The data used in this analysis was measured in 1995 and 1996 and consist of those runs with a nominal event vertex position. The specific luminosity determination is based on the rate of Bethe-Heitler events $ep \to ep\gamma$ (H1, 1995a), where the electron is measured in the electron tagger at $z = -33\,\mathrm{m}$ and the photon is detected in coincidence in the photon detector at $z = -110\,\mathrm{m}$. The main source of background is bremsstrahlung induced by the residual gas in the beam pipe, $eA \to eA\gamma$. These events contribute roughly 10% of the total bremsstrahlung event rate (at design luminosity). This contribution is subtracted on a statistical basis by using data from the electron pilot bunches. The luminosity $\mathcal{L}$ is determined according to

$$\mathcal{L} = \frac{R_{tot} - (I_{tot}/I_0)R_0}{\sigma_{vis}},$$

where R_{tot} is the total rate of the bremsstrahlung events,
R_0 is the rate due to electron pilot bunches,
I_{tot}, I_0 are the corresponding electron currents,
σ_{vis} is the visible part of the Bethe-Heitler cross section (acceptance and trigger efficiency included).

The integrated luminosity for this analysis amounts to a total of

$$\mathcal{L} = 8.31\,\mathrm{pb}^{-1}$$

and includes several corrections as discussed in the following. The total systematic uncertainty of the luminosity measurement is 1.1%, which is mainly due to the dependence of the acceptance on possible variations of the electron beam angle in the interaction region.

L1 Trigger Prescales

Due to the large specific luminosity delivered by HERA, limited computing power and (mainly) bandwidth, not all events triggered on L1 can be processed and written to tape. Many subtriggers i are prescaled by a factor k_i, such that only every $k_i' th$ event of a specific subtrigger is passed to the L4 trigger. This loss of efficiency is typically accounted for in a reduced luminosity for subtrigger i

$$\mathcal{L}_i = \sum_j \mathcal{L}_j / k_{i,j},$$

where the sum includes all runs j where subtrigger i was active. The variables $k_{i,j}$ and $\mathcal{L}_j$ are the prescale factor k_i and luminosity of run j, respectively. In 1995 (1996), the average prescale for S19 amounts to $k_{\mathrm{S19}} = 1.65$ (1.08), while the prescale for the background trigger S56 was $k_{\mathrm{S56}} = 2.79$ (1.17).

Satellite Bunch Correction

The proton beam is bundled into bunches during injection and acceleration. Protons lost from these bunches can accumulate into satellite bunches separated by $\sim 5\,\mathrm{ns}$ from the main bunches. The interactions of these bunches with the electron beam are excluded from analysis with information from the central trackers (z-position of the vertex), but the time resolution of the luminosity system is larger than 20 ns. Therefore a run-dependent correction factor of roughly 3% has to be applied to the measured luminosity.

Dead-time Correction

Events taking place during the readout of a previous event are not measured by the detector. This "dead time" is strongly dependent on the prevailing background and beam conditions. Under normal running conditions, the average readout time is roughly 1–2 ms. With an L1 input rate of $\sim 50\,\mathrm{Hz}$, this leads to a dead-time of $\lesssim 10\%$, which has to be corrected for in the luminosity measurement.

High Voltage Corrections

Some detector components may experience problems during (parts of) some runs. This information is automatically recorded with the event data, such that (parts of) runs can be excluded where detector components relevant for the analysis were not operational. Detectors required for this analysis include:

- CJC, the proportional chambers, and BDC;
- LAr calorimeter and Spacal;
- the entire instrumented iron return yoke;
- Time-of-flight, Veto, and Lumi systems.

4.6 Event Selection

Having defined all basic ingredients, we can now proceed to the description of the event selection. The analysis is done on all *signal* events passing the following cuts.

- For 1995, the run-number has to be in the range 121970 – 131045, where the shifted-vertex runs are excluded. In 1996, the run-number has to be in the range 151600 – 171156. The run-range of 168000 – 169814 has to be excluded due to problems with the central muon trigger.
- All relevant detector components (*cf.* Section 4.5) are fully operational.
- The internal data structure of the event is consistent.
- The primary event vertex is reconstructed and its z-value satisfies

  $$-50\,\mathrm{cm} < \mathrm{z_{Vertex}} < 40\,\mathrm{cm}.$$

  This cut removes events from proton satellite interactions.
- Halo muons cross the detector horizontally parallel to the beam pipe. They are rejected with a dedicated finder looking for horizontal energy-bands in the calorimeters at a fixed distance r from the beam pipe and constant azimuth ϕ.
- Coherent noise is electronic noise in the LAr calorimeter and is rejected by a special finder searching for a revealing cell pattern.
- Muons from cosmic rays (or events containing such a muon) are rejected as described in Section 3.5.
- A charged track multiplicity of $N \geq 5$ is required. As explained in Section 4.1, a single particle can lead to two sets of track parameterizations. Requiring $N \geq 5$ implies that at least three charge particles have left tracks in the inner trackers.
- Two jets, each having an energy of

  $$E_T^{Jet} \geq 6\,\mathrm{GeV}$$

  must be found by a cone algorithm using a cone radius of $R = 1$ in the $\eta\phi$-plane with $|\eta| < 2.5$. Input objects for the search algorithm are tracks and clusters as described in Section 4.3.

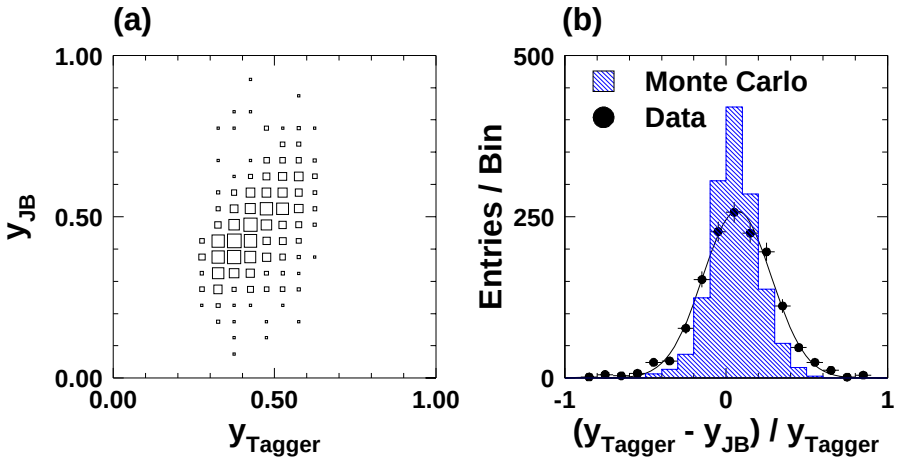

Figure 36: Correlation (a) and resolution (b) of y_{JB} determined from a comparison with y as measured in the electron tagger. The data are fitted with a Gaussian resulting in a width of $\sigma_{y_{JB}} = 21.3\%$. The shaded histogram is obtained from a AROMA 2.2 charm MC simulation.

- Untagged photoproduction events are selected by requiring that no scattered electron candidate be found with $\theta_e < 177.8°$. This eliminates DIS events with $Q^2 > 1\,\mathrm{GeV}^2$. The remaining background from DIS is suppressed by requiring

  $$0.1 < y_{JB} < 0.8,$$

  where the value of the y is determined with the method of Jacquet and Blondel (1979). The resolution in y_{JB} is determined by comparing y_{JB} with y as measured by the electron tagger at $z = -33\,\mathrm{m}$. This is shown in figure 36, where the data are fitted with a Gaussian resulting in a width of $\sigma_{y_{JB}} = 21.3\%$. In addition, the comparison as obtained from a MC simulation is shown. The resolution in y determined with the method of Jacquet-Blondel is not as good as for tagged photoproduction, but the MC simulation describes the situation adequately.
- At least one muon, identified in the instrumented iron return yoke according to Section 3.6 must be found with

  $$p_\perp^\mu > 2\,\mathrm{GeV}$$
  $$\theta^\mu \in [35°, 130°].$$

- The event must be triggered on L1 by an "actual" subtrigger S19 (subsequently verified on L4), and pass the background rejection cuts on L4 as described in Section 4.4. On L5, the event must be classified into CLASS 24.

Figure 37 shows the number of selected muons as a function of the integrated luminosity. It is compared with the number of muons accompanied by at least one jet and very loose cuts on the event quality. The data-taking period of 1995 extends over the first four bins, the remaining luminosity has been accumulated in 1996. There

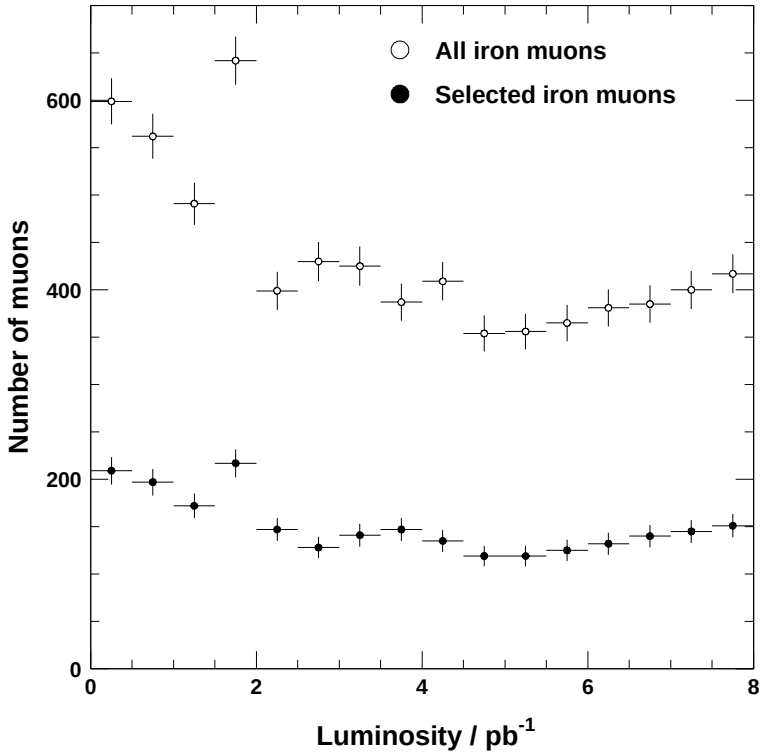

Figure 37: Number of "basic" (open circles) and final (solid circles) muon candidates found as a function of the integrated luminosity. 1995 extends over the first four bins, the remaining luminosity has been accumulated in 1996.

are some variations visible for 1995, which are due to changes in the trigger setup and varying background conditions. In 1996, the muon rate shows a remarkable stability.

For the determination of the fake muon background, a *background sample* has to be selected. The selection is identical to the signal sample except for the last two points. Instead of a muon candidate,

- a fake muon candidate is mandatory. This is defined to be a hadron passing the muon *track cuts*, *i.e.* having $p_\perp > 2\,\mathrm{GeV}/c$ and $\theta \in [35°, 130°]$.
- The event has to be triggered by an L4-verified "actual" subtrigger S56.

The final signal sample consists of 1140 events with 1156 muons. The background sample contains 52588 events and 88469 fake muon candidates.

Chapter 5

Measurement of $\sigma_{ep}^{c\bar{c}X}$ and $\sigma_{ep}^{b\bar{b}X}$

The predicted ratio of the production cross sections for light (uds), charm (c), and beauty (b) quarks is roughly $\sigma_{\gamma p}^{tot} : \sigma_{\gamma p}^{c\bar{c}X} : \sigma_{\gamma p}^{b\bar{b}X} \sim 2000 : 200 : 1$. As the primary goal of this analysis is the measurement of the open beauty production cross section, a strong suppression of both uds- and c-production is necessary. Soft processes — contributing to the bulk of the ep interactions — can be effectively eliminated by requiring two jets with $E_T > 6\,\text{GeV}$ each. Hard processes containing only light quarks are reduced by requiring a muon in one of the jets. Phase space for charm production is strongly reduced by requiring that the muon has a transverse momentum of $p_\perp^\mu > 2\,\text{GeV}/c$.

Untagged photoproduction events ($Q^2 < 1\,\text{GeV}^2$ and $0.1 < y_{JB} < 0.8$) are selected from data taken with the H1 detector in the period 1995 – 1996, corresponding to a luminosity of $\mathcal{L} = 8.31\,\text{pb}^{-1}$.

The separation of beauty and charm contributions is done on a statistical basis with the transverse momentum of the muon $p_{\perp,rel}^\mu$ relative to its jet axis. The measured $p_{\perp,rel}^\mu$ distribution is fitted with the shapes of b- and c-contributions, which are obtained from the AROMA 2.2 MC simulation. The light-quark background is taken directly from data. As the c- and uds-components show a very similar shape, the fit cannot discriminate between the two; the uds-background is therefore kept fixed. The fit results in the number of muons attributed to beauty-, charm-, and light-quark decays and allows thus a determination of the production cross sections.

5.1 Separation of Beauty and Charm from Background

The separation of beauty and charm relies on *(i)* the large mass difference of the b- and c-quarks and *(ii)* the significantly harder fragmentation in the case of b-quarks. The b-quark mass is $m_b = 4.75 \pm 0.25\,\text{GeV}/c^2$, while the mass of the c-quark is only $m_c = 1.5 \pm 0.3\,\text{GeV}/c^2$. Muons from semi-leptonic b-decays have a larger momentum along and more transverse momentum with respect to the quark direction than those

from c-decays. Requiring a transverse momentum of the muon of $p_\perp^\mu > 2\,\mathrm{GeV}/c$ reduces the *predicted* event rate with semi-leptonic b-decays by roughly a factor of four, while the corresponding reduction for charm amounts to ~ 400.

$p_{\perp,rel}^\mu$ distribution

The different physical components — beauty, charm, and light-quark background — are separated with the transverse momentum of the muon $p_{\perp,rel}^\mu$ relative to the quark direction. The direction of flight of the quark is approximated with the thrust axis of the jet containing the muon, *cf.* equation (6) in section 4.3, where the momentum of the muon is excluded in the calculation of the thrust axis. This allows a better separation of beauty and charm events. The quantity $p_{\perp,rel}^\mu$ is thus calculated as

$$p_{\perp,rel}^\mu \equiv \frac{\mathbf{p}_\mu \times \mathbf{T}_{Jet}^{w/o\ \mu}}{|\mathbf{T}_{Jet}^{w/o\ \mu}|}.$$

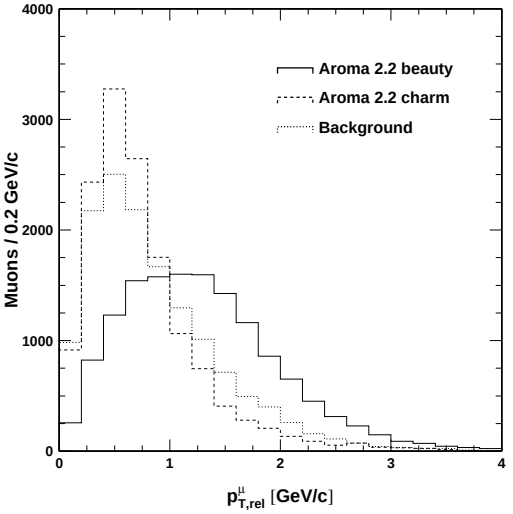

Figure 38: Comparison of the $p_{\perp,rel}^\mu$ distributions for muons due to beauty, charm, and uds-background. The predictions for the beauty and charm contributions are taken from the MC simulation AROMA 2.2, the background is extracted directly from data as explained in the text. The three histograms are normalized to the same number of entries.

In figure 38 the $p_{\perp,rel}^\mu$ distribution is shown for beauty, charm and light-quark components, all normalized to the same number of entries. The distribution for b-quarks contains both direct decays ($b \to c\mu X$) and sequential decays ($b \to c \to s\mu X, b \to \tau \to \mu X$) with the appropriate branching ratios. (The determination of the uds-background is described in the next section.) A clear difference between b-quarks on the one hand and c- as well as uds-quarks is obvious. The latter two, on the other hand, show a

very similar shape. This is analogous to the situation at other experiments, *cf. e.g.* UA1 (1988) or DØ (1995). The implication of this similarity is that any uncertainty in the uds-background will strongly influence the charm component, but will leave the beauty-component virtually unaffected.

Light-Quark Background

The background component in the $p^{\mu}_{\perp,rel}$ distribution is extracted directly from data with the knowledge about muon misidentification as described in chapter 3. A uds-background event is characterized by:

- 2 jets;
- a fake muon, which can be either a misidentified punch- or sail-through hadron, or a muon due to in flight-decay of a light hadron;
- S19 has been set by the fake muon and the event passed furthermore the relevant cuts on L4 and L5.

With the assumption that such an event is "somehow" triggered by at least one of the triggers, the total background can be accumulated by analyzing the entire event sample on tape. The uds-component in the $p^{\mu}_{\perp,rel}$ distribution is accumulated from all fake muon candidates each contributing with a weight

$$f_h^{\pi,K,p}(p) \otimes P_h^{\mu}(p,\theta) \cdot \epsilon_{S19} \cdot \frac{\mathcal{L}_{S19}}{\mathcal{L}_{tot}}, \tag{7}$$

where

$f_h^{\pi,K,p}$ is a parameterization of the relative contributions of pions, kaons, and protons to entire hadronic particle spectrum; it sets h to be either a $\pi^{\pm}$, a $K^{\pm}$, or a proton.

$P_h^{\mu}(p,\theta)$ is the misidentification probability for a hadron to be identified as a muon; depending on the value assigned to h by $f_h^{\pi,K,p}(p)$, either $P_{\pi}^{\mu}(p,\theta)$, $P_K^{\mu}(p,\theta)$ or $P_p^{\mu}(p,\theta)$ is used for the calculation of the misidentification probability.

ϵ_{S19} is the trigger efficiency for a fake muon to set subtrigger S19, which is assumed to be the same as for genuine muons. This assumption is valid because the requirement on a muon *track* in the instrumented iron return yoke is stricter than the *trigger* requirement, *i.e.* if the hadron leaves a muon signature, this signature is sufficient to set the trigger condition.

$\mathcal{L}_{S19}/\mathcal{L}_{tot}$ is the normalization of the luminosities required by the prescaling of S19.

The assumption that the overall trigger efficiency for background events is $\epsilon_{tr} = 1$ may not be true. Therefore background events are selected by the jet trigger S56 and a correction for the trigger efficiency is applied, leading to the following weight for every fake muon candidate

$$f_h^{\pi,K,p}(p) \otimes P_h^{\mu}(p,\theta) \cdot \frac{\epsilon_{S19}}{\epsilon_{S56}} \cdot \frac{\mathcal{L}_{S19}}{\mathcal{L}_{S56}}, \tag{8}$$

where

ϵ_{S56} is the trigger efficiency for subtrigger S56 to trigger a background event, and
$\mathcal{L}_{S56}$ is the prescale-corrected luminosity for the trigger used to select background events.

The largest uncertainty in the background estimate is due to the uncertainty in the trigger efficiency, which is absorbed into the systematic error. The background estimate must contain also the fake muon contributions from hadronic decays of heavy quarks. These events show an increased amount of kaons leading to a higher average misidentification probability (with respect to the normal uds-background event). This is again incorporated into the systematic uncertainty. The shape of the distribution does not need to be corrected, as it is directly extracted from data (and therefore already contains this contribution).

Composition of the Data

The composition of the data is determined on a statistical basis by fitting the measured $p^{\mu}_{\perp,rel}$ distribution with the components of beauty, charm, and uds-background. As the charm and uds-background distribution are very similar in shape, a fit cannot distinguish between the two. The uds-background is therefore fixed to the calculated number of entries and a two-parameter fit is done to determine the contributions of charm and beauty.

The relative composition of the data sample is determined with a χ^2-fit and amounts to

$$\begin{aligned} f_b &= 51.4 \pm 4.4\% \quad \text{(beauty)} \\ f_c &= 23.5 \pm 4.3\% \quad \text{(charm)} \\ f_{uds} &= 23.5\% \quad \text{(background, fixed)} \end{aligned} \tag{9}$$

with a $\chi^2/d.o.f. = 1.0$. Maximum likelihood fits result (within the statistical uncertainty) in the same relative composition. The result of the fit is shown in figures 39 (a) and (b).

Cross-checks

A good description of the data should be possible in other variables, too, by weighting beauty, charm, and background components according to the fit result in (9). This is indeed the case as shown in figures 40(a) - (d), where the measured $p^{\mu}_{\perp}$, θ^{μ}, $E_T^{\mu-Jet}$, and $\theta^{\mu-Jet}$ distributions are compared to the sum of the contributions of b-, c-, and uds-quarks. All spectra show a good agreement of the data with the sum of the components.

The y_{JB} distribution is shown in figure 41, where a clear difference between the heavy quark distributions and the background can be observed. The different shapes are due to the large contribution of *resolved processes* in light-quark production, which need a large y in order to have a $\sqrt{\hat{s}}$ large enough to produce two hard jets. This is corroborated by the MC simulation PYTHIA showing a good agreement between the MC and background y_{JB} distribution.

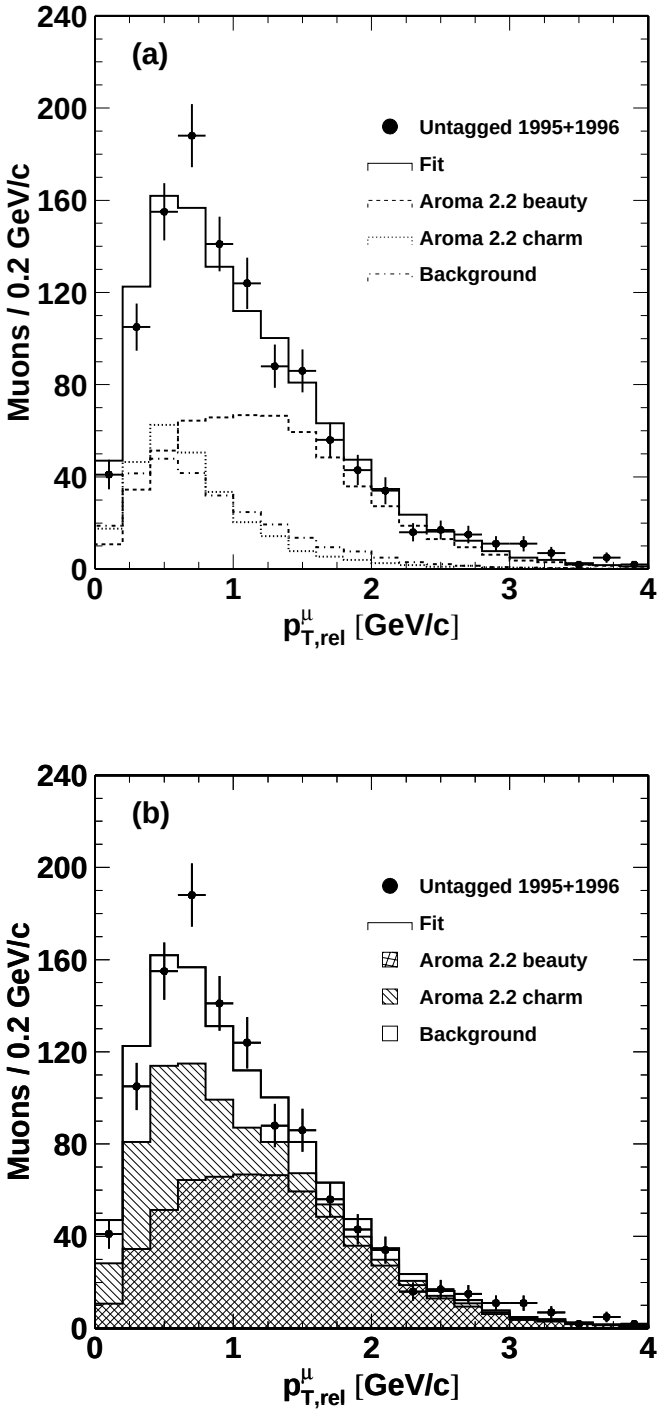

Figure 39: (a) $p_{\perp,rel}^{\mu}$ distribution for inclusive muon candidates in untagged 2-jet events, with one jet containing the muon. The data are shown as filled circles, the fit and the predictions for the various components as histograms. The heavy quark components are taken from AROMA 2.2, the background is extracted from data as described in the text. (b) shows the $p_{\perp,rel}^{\mu}$ distribution, where the components are shown cumulatively.

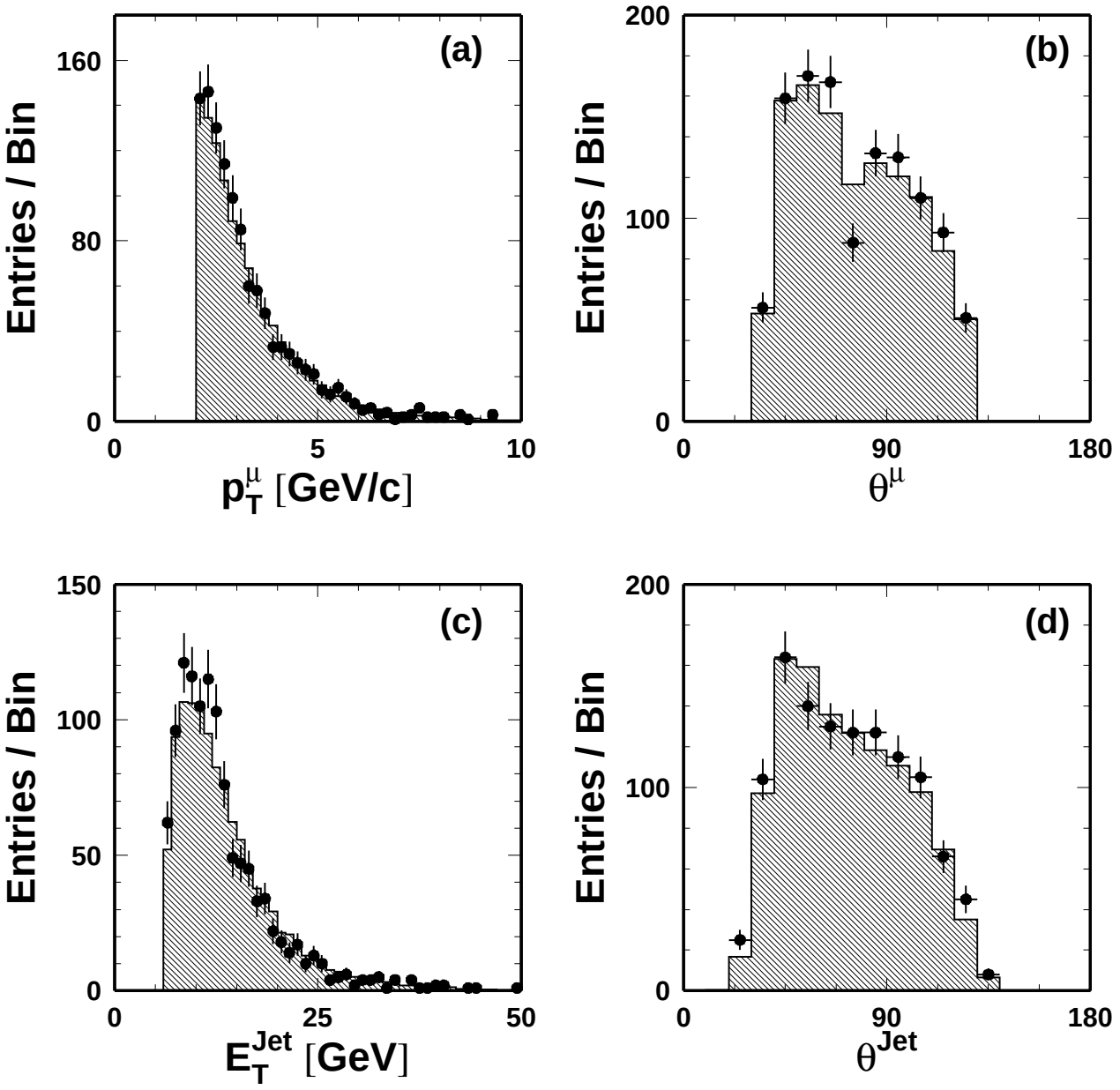

Figure 40: Comparison of measured kinematic distributions with the sum of the fitted components of beauty, charm and *uds*-background according to equation (9). (a) and (b) show the transverse momentum and polar angle distributions for muons. (c) and (d) display the transverse energy and polar angle distributions for the jet containing the muon.

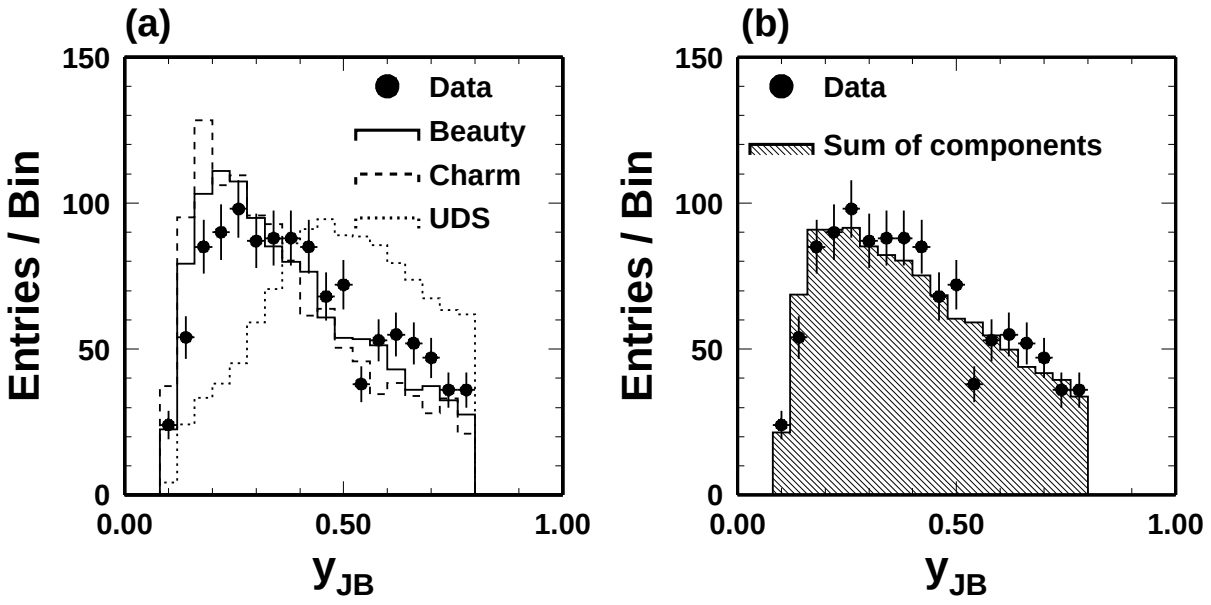

Figure 41: Comparison of the y_{JB} distributions. (a) shows the the different components (all normalized to the same number of entries), while (b) displays the sum of all components as the shaded histogram.

The pronounced difference in the y_{JB} distribution for the background and heavy quark components can be used to reduce the former significantly by restricting $0.1 < y_{JB} < 0.4$ (*cf.* figure 42). This reduces the background component to $f_{uds} = 14.4\%$, while the contributions of b and c amount to $f_b = 59.8 \pm 6.1\%$ and $f_c = 23.8 \pm 5.7\%$.

5.2 Visible Beauty and Charm Cross Section

The visible cross section is determined from the number of muons N_Q^μ attributed to either b- or c-decays by

$$\sigma_{vis}(ep \to Q\overline{Q}X) = \frac{1}{2}\frac{N_Q^\mu}{\mathcal{L} \cdot \epsilon_{tr} \cdot \mathcal{B}_Q \cdot A_Q^{vis}}, \tag{10}$$

where

- N_Q^μ is the number of muons attributed by the fit of the $p_{\perp,rel}^\mu$ distribution to the decay of the quark Q.
- $\mathcal{L}$ is the integrated luminosity and amounts to $\mathcal{L} = 8.31\,\mathrm{pb}^{-1}$ taken in the years in 1995 and 1996;
- ϵ_{tr} is the lumi-weighted mean trigger efficiency and amounts to $\epsilon_{tr} = 80.1\%$;
- $\mathcal{B}_Q$ is the (total) branching ratio for a quark Q decaying into a final state with at least one muon and amounts to $\mathcal{B}_b = 19.1\%$ for b-decays, and to $\mathcal{B}_c = 9.1\%$ for c-decays.

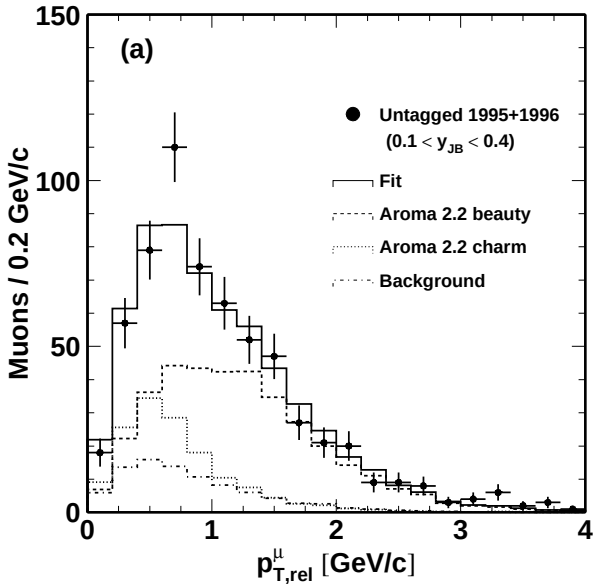

Figure 42: (a) $p^{\mu}_{\perp,rel}$ distribution for inclusive muon candidates in untagged 2-jet events with $0.1 < y_{JB} < 0.4$, where one jet contains the muon. The data are shown as filled circles, the fit and the predictions for the various components as histograms.

- A_Q^{vis} denotes the combined visible acceptance and reconstruction efficiency and is calculated from the MC simulation as

$$A_Q^{vis} = \frac{N^{rec}_{\mu(Q)}(y_{JB}, Q^2, p^{\mu}_{\perp}, \theta^{\mu})}{N^{gen}_{\mu(Q)}(y, Q^2, p^{\mu}_{\perp}, \theta^{\mu})},$$

where the numerator is the number of reconstructed muons due to the decay of quark Q in the visible range and the denominator is the corresponding number of generated muons. The visible range is defined as

$$\begin{aligned} Q^2 &< 1\,\mathrm{GeV}^2 \\ 0.1 &< y < 0.8 \\ p^{\mu}_{\perp} &> 2\,\mathrm{GeV}/c \\ 35^\circ &< \theta^{\mu} < 130^\circ. \end{aligned} \tag{11}$$

The data sample has a mean $\overline{y}_{JB} = 0.41$, corresponding to a mean photon-proton cms energy of $W_{\gamma p} = 192\,\mathrm{GeV}$.
A_Q^{vis} includes the muon reconstruction efficiency and the efficiency of the requirement to find two jets (one of them containing the muon) with $E_T > 6\,\mathrm{GeV}$ each in the event. A_Q^{vis} amounts to

$$\begin{aligned} A_b^{vis} &= 25.1\% \\ A_c^{vis} &= 18.6\%. \end{aligned}$$

- The factor $\frac{1}{2}$ quantifies the fact that the detected muon originates either from the quark or the anti-quark.

Using equation (10), the cross section for beauty and charm production in the visible range as defined in (11) is calculated to be

$$\begin{aligned} \sigma_{vis}(ep \to b\bar{b}X) &= 0.93 \pm 0.08\,^{+0.21}_{-0.12}\,\text{nb} \\ \sigma_{vis}(ep \to c\bar{c}X) &= 1.20 \pm 0.23\,^{+0.30}_{-0.38}\,\text{nb}, \end{aligned} \tag{12}$$

where the first uncertainty is statistical and the second systematic. (See section 5.4 for a discussion of the systematic error.) The measured cross sections are consistent within the statistical uncertainty when measured in 1995 alone, 1996 alone, or both years combined.

The relative error on the charm cross section is significantly larger than for the beauty cross section. This is due to the similarity of the $p^{\mu}_{\perp,rel}$ distribution for c- and uds-quarks. Every uncertainty in the background directly influences the charm cross section.

This result can be compared to the calculation of the MC simulation AROMA 2.2 predicting

$$\begin{aligned} \sigma_{vis}^{MC}(ep \to b\bar{b}X) &= 0.19\,\text{nb} \\ \sigma_{vis}^{MC}(ep \to c\bar{c}X) &= 0.99\,\text{nb}. \end{aligned}$$

The predicted charm cross section is seen to be slightly lower than the central value of the measurement, though still within the statistical uncertainty. This behavior is expected from measurements of the charm cross section based on the reconstruction of $D^{*\pm}$ (H1, 1996). The beauty cross section, on the other hand, is seen to be significantly larger than the expectation.

5.3 Extrapolation to the Full Kinematic Range

The calculation of the total cross section is done by replacing the visible acceptance A_Q^{vis} with the total acceptance A_Q, where the denominator now comprises all generated muons, in equation (10). As the dominant part of heavy quark production is at threshold, this implies a large extrapolation introducing significant uncertainties. The cross section dependence on $Q^2, y, p^{\mu}_{\perp}, \theta^{\mu}$ must be described properly by the model used for the extrapolation.

Nevertheless, an extrapolation with the leading-order MC simulation AROMA 2.2 is presented in order to compare this measurement with other measurements of the total charm production cross section (and eventually other measurements of the beauty production cross section, *e.g.* Kander (1998)). The total production cross sections amount to

$$\begin{aligned} \sigma_{tot}(ep \to b\bar{b}X) &= 18.8 \pm 1.6\,\text{nb} \\ \sigma_{tot}(ep \to c\bar{c}X) &= 735\ \ \pm 138\,\text{nb}, \end{aligned} \tag{13}$$

where only the statistical uncertainty is given. The total charm production cross section has been measured by H1 (1996) with the reconstruction of $D^{*\pm}$ decays to be $\sigma_{tot}(ep \to c\bar{c}X) = 941 \pm 160^{+142}_{-120}$ nb, which is slightly higher than this measurement. Both results are compatible within the statistical and systematic uncertainty.

5.4 Systematic Uncertainties

In the following, an overview on the various systematic uncertainties for the visible cross sections is given. All considered contributions to the total systematic error are summarized in table 5.

- MC event generator. This analysis relies to a strong degree on the validity of the correct description of the event by a (leading order) MC simulation. An indication for the uncertainty may be gained by using a completely different event generator. For this purpose, the entire analysis was redone with HERWIG 5.9. The visible beauty cross section increased slightly, which is taken into account with $\Delta\sigma/\sigma = +5.1\%$. The effect on the visible charm cross section is considerably larger with $\Delta\sigma/\sigma = -24.6\%$.
- Branching ratios. The branching ratios as extracted from (PDG, 1996) are all flawed with uncertainties. Including all cascade decays, a total uncertainty of 1.6% on the total branching ratio implies for the visible beauty cross section $\Delta\sigma/\sigma = \pm 11.4\%$ and for the visible charm cross section $\Delta\sigma/\sigma = ^{+14.4}_{-8.5}$ %.
- Absolute hadronic energy scale. All cluster energies in the MC simulation were rescaled by ± 1.04 and the entire analysis was repeated. The difference to the standard energy scale is used as systematic error and amounts for the visible beauty cross section to $\Delta\sigma/\sigma = ^{+8.9}_{-1.3}$ %, while the effect on the visible charm cross section is $\Delta\sigma/\sigma = ^{+16.1}_{-4.2}$ %.
- Luminosity. The uncertainty in the luminosity has to be considered both in the calculation of the cross section according to equation (10) and in the determination of the weighting factor for a background muon fake candidate (equation (8)). The resulting uncertainty for the visible beauty cross section amounts to $\Delta\sigma/\sigma = ^{+5.1}_{-1.3}$ % and for the visible charm cross section $\Delta\sigma/\sigma = +6.7\%$.
- Trigger efficiency. The uncertainties in ϵ_{S19} and ϵ_{S56} lead to uncertainties in the relative amount of signal to background events and thus influence the cross sections. The changes in the same direction due to $\delta\epsilon_{S19}$ and $\delta\epsilon_{S56}$ were added in quadrature and yield for the visible beauty cross section $\Delta\sigma/\sigma = ^{+5.7}_{-5.6}$ %, while the uncertainty in the visible charm cross section amount to $\Delta\sigma/\sigma = ^{+6.6}_{-9.0}$ %.
- Background shape. Using S56 as subtrigger for the background introduces a slight bias in so far as the shape of the $p^{\mu}_{\perp,rel}$ distribution is concerned. This uncertainty is accounted for by using different subtriggers for the $p^{\mu}_{\perp,rel}$ spectrum of the background and refitting. The spectrum is normalized to the same number of fake muon candidates as the sample triggered by S56. (The uncertainty in the trigger

efficiency is taken into account separately.) The effect on the visible beauty cross section is $\Delta\sigma/\sigma = ^{+7.5}_{-0.8}$ % and for the visible charm cross section $\Delta\sigma/\sigma = ^{+3.1}_{-15.9}$ %.

- Muon reconstruction. The iron track reconstruction shows differences between MC simulation and data, especially in transition regions (border region between the barrel and end-caps, support of H1 at $\theta = -90°$). The (total) overestimation of ϵ_{rec} in the MC simulation is taken into account as an estimate for this systematic uncertainty and yields for the visible cross sections $\Delta\sigma/\sigma = +6.5\%$.
- Track reconstruction. An estimate for the reconstruction efficiency of high momentum tracks in the central part is found by extrapolating iron tracks into the CJC and checking that a matching inner track is found. The (total) overestimation in the MC simulation is taken as a systematic error of $\Delta\sigma/\sigma = +5.0\%$.
- Pion:Kaon ratio. The cuts used in the event selection provide a data sample enriched with heavy quarks. They should therefore show an increased amount of kaons (relative to pions) when compared to light-quark events. As a consequence, $f_h^{\pi,K,p}$ could underestimate the kaon-contents in the data-sample and thus the mean misidentification probability $P_h^{\mu}(p)$. This uncertainty is estimated by varying the ratio of pions to kaons from the default to 1:1. The charm cross section is influenced directly by $\Delta\sigma/\sigma = 39.8\%$, while the beauty cross section is hardly touched with $\Delta\sigma/\sigma = -5.1\%$. This uncertainty is not included in the total systematic error, as the pion:kaon ratio of 1:1 is rather arbitrary and the beauty cross section shows only a weak dependence.

Table 5: Summary of the systematic uncertainties in the visible beauty and charm cross sections.

Systematics	$\Delta\sigma_{b\bar{b}}^{vis}/\sigma_{b\bar{b}}^{vis}$	$\Delta\sigma_{c\bar{c}}^{vis}/\sigma_{c\bar{c}}^{vis}$
HERWIG 5.9	+5.1 %	−24.6%
Branching ratio $\mathcal{B}_b$	±11.4%	$^{+14.4}_{-8.5}$ %
Energy Scale	$^{+8.9}_{-1.3}$ %	$^{+16.1}_{-4.2}$ %
Luminosity	$^{+5.1}_{-1.3}$ %	+6.7 %
Trigger Efficiency	$^{+5.7}_{-5.6}$ %	$^{+6.6}_{-9.0}$ %
Background Shape	$^{+7.5}_{-0.8}$ %	$^{+3.1}_{-15.9}$ %
Muon Reconstruction	+6.5 %	+6.5 %
Track Reconstruction	+5.0 %	+5.0 %
Total	$^{+20.4}_{-12.9}$ %	$^{+25.1}_{-32.1}$ %

Summary and Outlook

Open beauty and charm production has been measured with untagged photoproduction events ($Q^2 < 1\,\mathrm{GeV}^2$ and $0.1 < y_{JB} < 0.8$) taken by the H1 detector during 1995 – 1996, corresponding to an integrated luminosity of $\mathcal{L} = 8.31\,\mathrm{pb}^{-1}$. The visible production cross sections were determined in the kinematic range ($Q^2 < 1\,\mathrm{GeV}^2$, $0.1 < \mathrm{y_{JB}} < 0.8$, $p_\perp^\mu > 2\,\mathrm{GeV}/c$, $35^\circ < \theta^\mu < 130^\circ$) to be

$$\sigma_{vis}(ep \to b\bar{b}X) = 0.93 \pm 0.08\,^{+0.21}_{-0.12}\,\mathrm{nb}$$
$$\sigma_{vis}(ep \to c\bar{c}X) = 1.20 \pm 0.23\,^{+0.30}_{-0.38}\,\mathrm{nb},$$

where the first uncertainty is statistical and the second is systematic.

The visible beauty cross section was found to exceed the expectation of AROMA 2.2 by roughly a factor of five. The visible charm cross section agreed well with the prediction of AROMA 2.2. An extrapolation of the visible charm cross section to the full kinematic range resulted in a value consistent with the measurement based on the reconstruction of $D^{*\pm}$ mesons.

This analysis represents only a first step in b-physics at HERA. It will be very interesting to measure the production cross section in different kinematic régimes, *e.g.* tagged photoproduction and deep inelastic scattering, and to determine differential cross sections. Due to the large mass of the b-quark, theoretical uncertainties are much reduced in comparison with charm physics, making the extraction of *e.g.* the gluon density $xg(x)$ or the beauty contribution F_2^b to the proton structure function very promising analysis goals.

Appendix 1

Receiver Boards of the DC-$r\phi$ Trigger

The drift-chamber $r\phi$-trigger (Wolff, 1993; Bernet, 1995) finds those tracks in the $r\phi$-plane which have a distance of closest approach to the nominal beam line of $|d_{ca}| \lesssim 2\,\mathrm{cm}$ and a polar angle of $25° < \theta < 155°$. A total of 10 layers from CJC 1 and the inner part of CJC 2 are used for the track finding in the trigger. After the CJC signals are digitized by a threshold comparator, they are synchronized to the HERA clock of 10.4 MHz in the *receiver boards*. This reduces the accuracy of the drift-time measurement from 1 ns (as obtained in the drift-chamber signal processing path) to 96 ns, corresponding to about 5 mm of position resolution. This resolution is improved in 5 layers by doubling the sampling frequency to 20.8 MHz. The resulting hit pattern is transferred to the main trigger logic boards, where it is serially clocked into shift registers, where 10′000 predefined masks are compared to the hit pattern to mark active roads.

Apart from this synchronization, the receiver boards provide the facility to test the hardware of the trigger by loading the bit pattern corresponding to a mask (*test-pattern*) into on-board memories. Feeding this bit pattern into the main trigger logic should result in a trigger signal for functioning masks, whereas defective signal paths can be determined (and fixed) from the absence of a trigger signal.

The original receiver boards of the DC-$r\phi$ trigger had several shortcomings:

- The test-pattern bits were fed into the signal path only after the synchronization with the HERA clock. This had severe consequences for the timing parameters of the trigger, as the settings for data-taking were not the same as for test-pattern. The conversion between the two parameter sets was tricky and could have unforeseen side-effects due to non-linearities of various delay lines.
- Test-pattern bits were produced at a rate of 10.4 MHz, which is not sufficient for layers with a sampling frequency of 20.8 MHz. Therefore it was not possible to test the full time resolution of the trigger masks.
- The 20.8 MHz clock produced on the receiver boards was generated in a cost-effective manner. This led to an asymmetric wave form, which had a negative influence on the trigger performance.

With all these shortcomings in mind, new receiver boards were designed in 1995 and taken into operation in spring 1996.

In the following section A1.1, the hardware of the receiver boards is described. The programming of the boards (as implemented in *DcTrig*, the control program of the trigger) is described in section A1.2. The final section A1.3 reports on the first complete test of the trigger with the new boards.

A1.1 The Hardware of the New Receiver Boards

The basic structure of the receiver boards resembles the original layout and is shown in figure 44. A photograph of the receiver boards is shown in figure 43. The functionality can be divided into several modules, which shall be described in turn. All references to chips follow the naming convention of the schematics (Pollet, 1995).

Main Signal Path

Each board processes the input signals of one cell of CJC1 and two cells of CJC2, which gives a total of 29 signal lines. In addition to the layers which are used for the current L1 trigger, additional layers are handled for a possible upgrade to a L2 track trigger. The chamber signals enter the board via connectors J3 A-B/C-D, J4 A-B, and J5 A-B/C-D on the front panel. The transmission from the active shaper and discriminator 'ASD' boards is done in emitter coupled logic 'ECL' in order to achieve maximum noise immunity. Free lines on the input cables serve as transmission lines for the thresholds of the discriminators on the ASD boards.

After passing the signal lines through a set of jumpers (to be used for a possible L2 track trigger), they are converted to transistor-transistor logic 'TTL' levels in ECL/TTL converters (MC10125, chips U1 ... U8). The next step is the merging of the signal paths for chamber signals and test-pattern from on-board memories. This is achieved with two junctions (ABT32316, chips U9 and U10), which are controlled by a single signal line $\overline{\text{DIR_DATA}}$.

The output lines of these junctions are fed into the synchronization, which is implemented in a field programmable gate array 'FPGA' (Xilinx XC3030, chip U11). The programming of the FPGA is accomplished with a special 36 kbit PROM (XC1736, chip U12). XIL_RESET is used to reset the FPGA and initiate a reloading from the PROM. The basic synchronization unit has been taken over from the old design. A detailed description is given in (Wolff, 1993). It is crucial for a maximum trigger efficiency, that each signal line has the same propagation delay from the entry into the board to the first flip-flop of the synchronization circuit. The measurement of this propagation delay is done as follows. Test pulses are generated with a special test-board (Seywert, 1995), which allows to shift the pulses in steps of 1 ns relative to the HERA clock. The input signal (measured on the output pin of the ECL/TTL converter) is used as trigger for the measurement of the synchronization output. If the timing of the test pulses is such that they are on the edge of a synchronization window, some will have the minimal delay time while others only make it into the next synchronization window, producing pulses separated from the first by 96 ns (48 ns) for the 10.4 MHz (20.8 MHz)

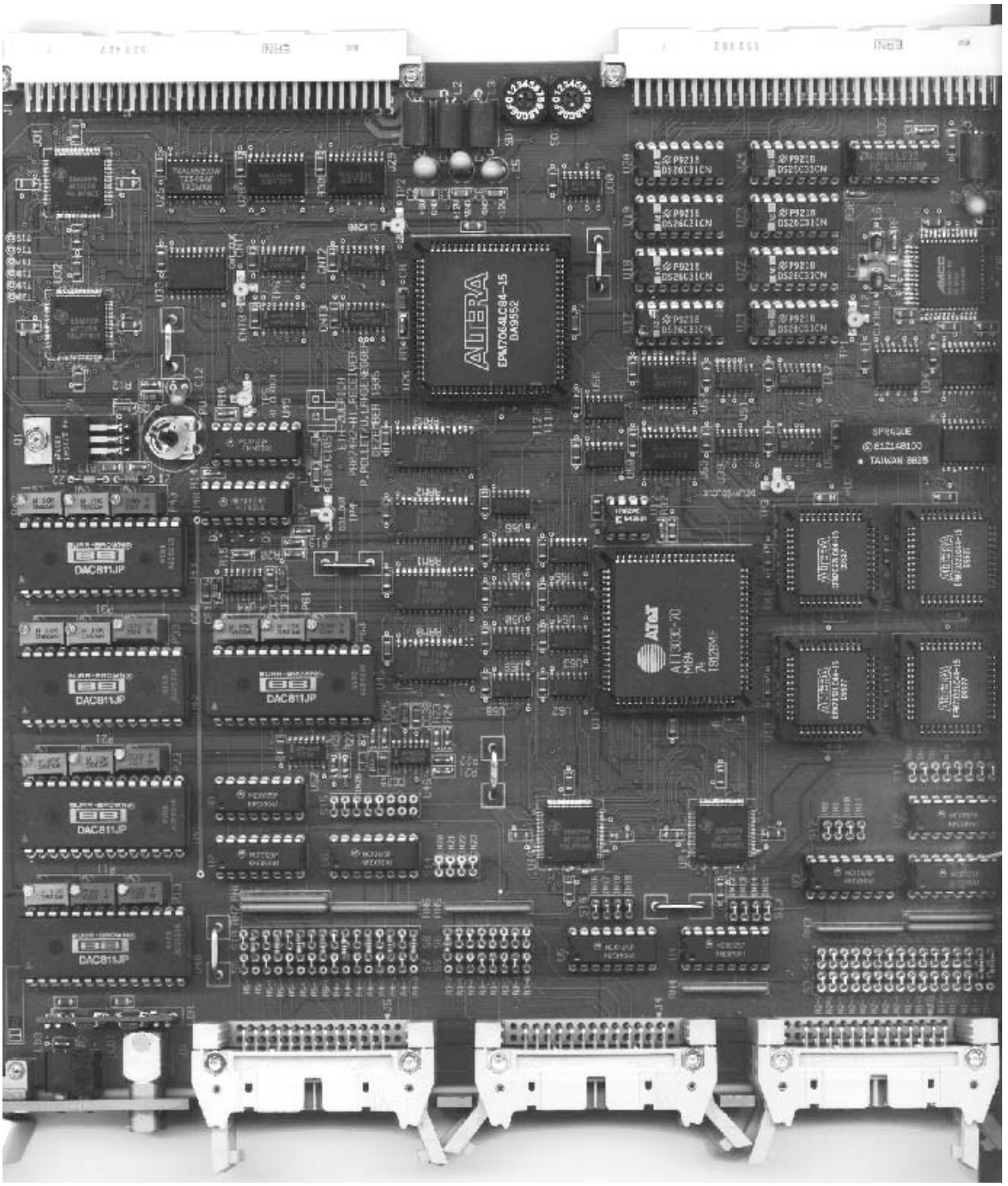

Figure 43: Photo of the new receiver boards of the drift-chamber $r\phi$-trigger at H1.

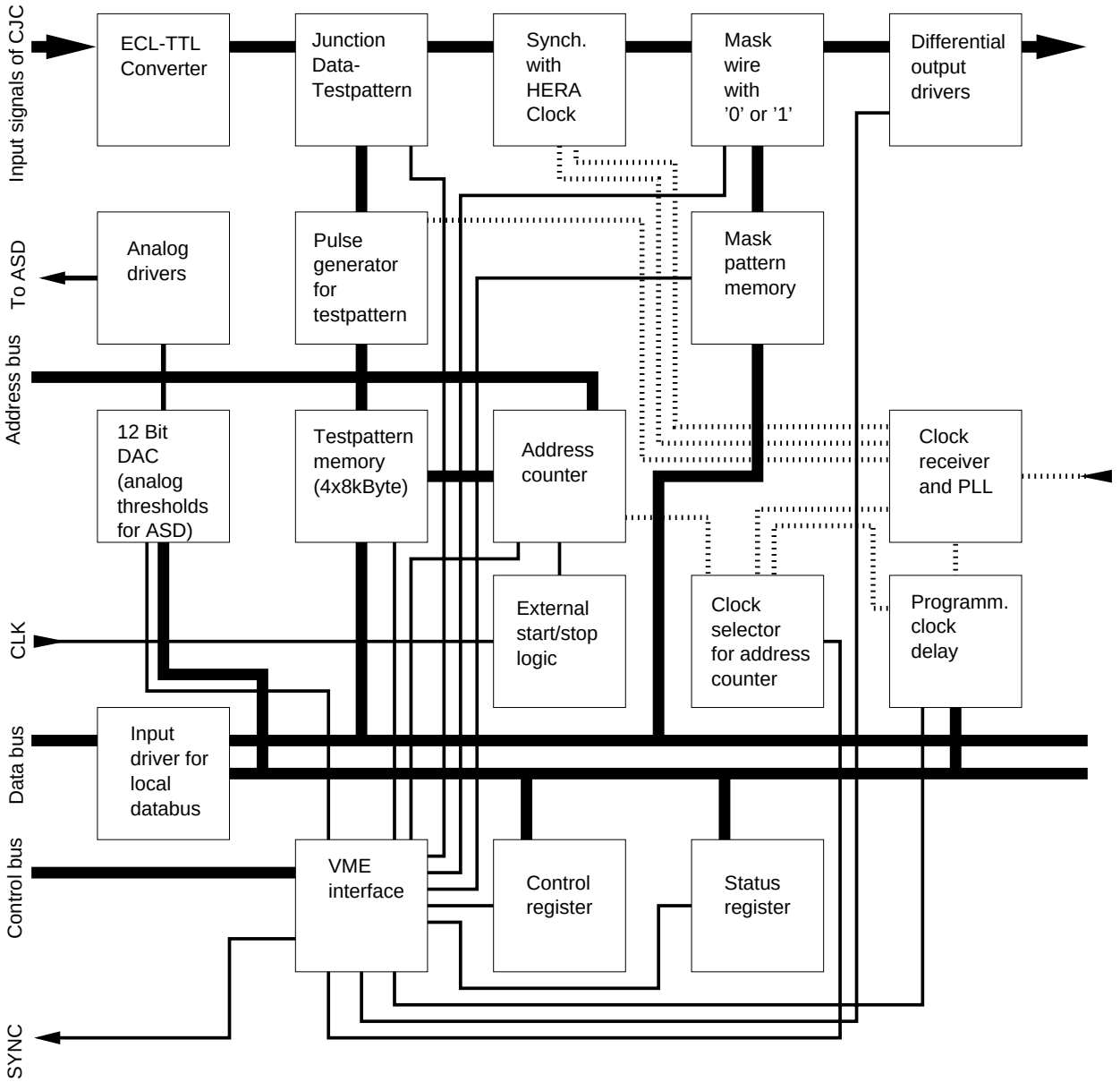

Figure 44: Block diagram of the new receiver boards. The main signal path is shown in the upper row and proceeds from the input connectors on the left to the output connectors on the right. Clock circuitry is indicated by dotted lines. Control signals propagate along solid thin lines. Solid thick lines represent buses for data, addresses and chamber signals. The control signal entering at 'CLK' is used for the synchronized start during a test-pattern run. The 'SYNC' output of a master receiver board is used to generate an external L1KEEP for the frontend-processor in order to start the readout of the trigger during a selftest.

layers, respectively. This situation is easily measured, as the early and late pulses,

leading to "double pulses", will be visible on a scope at the same time. This allows the determination of the minimal propagation time (modulo 96 ns) from the delay selected on the test-board. The propagation times of all channels are equalized by prolongation of all lines to the level of the slowest channel. This is achieved with manual routing of the pulse lines within the FPGA. Figure 45 shows a comparison of the propagation times for each channel before and after the optimization. The signals are inverted in the I/O blocks immediately before leaving the FPGA.

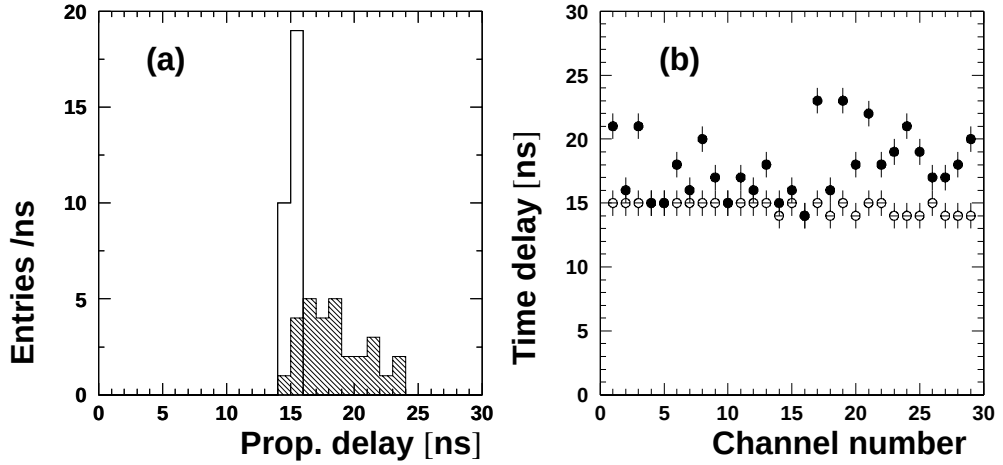

Figure 45: Timing of the individual channels on a receiver board. The distribution of the propagation delays is shown in (a); the propagation delay for every channel is displayed in (b). The hatched histogram (filled points) shows the original situation, the solid histogram (open points) after the optimization.

After the synchronization, the signal lines are passed through an array of 4 programmable logic devices 'PLD' (EM 7032, chips U13 ... U16) which can be used to mask single lines with either (logical) HIGH or LOW. This allows to defuse dead or inefficient wires in the CJC. There is a drawback, though. The time resolution of the trigger is strongly degraded when wires used for the T0 information are masked. In order to map a 16 bit wide data bus onto 29 signal channels, a minimal multiplexing has to be performed. Signal lines 0 ... 15 are grouped into the 'Low' half-word, while the remaining lines 16 ... 28 are mapped into the 'High' half-word. Selecting either Low or High half-word is done with the control signals MSKL_SEL and MSKH_SEL, respectively. The mask for either half-word is defined with WD_LATCH (as explained in the next section). Before becoming active, the masks have to be enabled with ENA_SEL, where the selection between Low and High half-words is again done with MSKL_SEL and MSKH_SEL, respectively.

The last step in the signal path is the conversion into ECL signals for maximum noise immunity during the transmission on the active backplane. This is achieved by standard output drivers (26LS31, chips U17 ... U24). The signals leave the board via

connector J2, which is a non-standard VME* connector.

Threshold Setting for the ASD's

The thresholds for the discriminators on the ASD boards are set with 5 digital to analog converters 'DAC'(12 Bit DAC 511, chips U40 ... U45), which are loaded using LAT10. The output voltage can be varied in the range of $[-8, 8]$ V. The transmission of the levels is done with lines J3/A1, J3/C1, J4/A1, J5/A1, and J5/C1, respectively. These cables have a length of ~ 30 m, which leads to some "walk" of the level once a change has been programmed. It is therefore inevitable to iterate the calibration of the threshold values until the effective value as measured on the ASD has stabilized. The threshold setting is a compromise between high efficiency and high noise suppression. It has been set to $U = -180$ mV for all wires.

Clock Circuitry

Pins A31/C31 of the non-standard VME connector J2 provide the base system clock. After conversion to TTL in a converter (26LS32, chip U35), the clock is fed into a phase-locked loop 'PLL' (S4406, chip U36) which provides a very symmetric and stable clock at 10.4 MHz and 20.8 MHz. A delayed clock is generated from this reference clock as follows. In a first step, the clock is passed through a programmable delay line (DS1020, chip U34), which allows delays in steps of 10 ns and can be programmed with WD_DELAY (writing bits 8 ... 15 of the internal data bus into a latch (ABT374, chip U37)). The output clock is passed into a second delay line (steps of 1 ns, DDU7J-10, chip U27), whose output is selected with bits 0 ... 7 of the internal data bus (again in conjunction with WD_DELAY) and three 1-out-of-4 multiplexers (AC153, chips U55 ... U57). A maximum time delay of $\Delta t = 130$ ns can be achieved.

VME Interface

The receiver boards are controlled with a custom VME interface implemented on a PLD (EM7064, chip U26). A detailed description of the programming of the VME chip will be given in the next section. All control signals of the VME bus are fed directly into the PLD, while the data lines are split with two selectors (ABT32316, chips U31 and U32) into two buses: the memory data bus (lines D0 ... D31) and the control bus (lines DI0 ... DI15). The latter is used to load the DAC's and to propagate control signals into the control register (ABT273, chip U33). The address lines of the VME bus are held in two latches (ABT373, chips U28 and U29), which are activated when the PLD detects a match with the comparator (74ALS520, chip U25) between the board address (set by jumpers SD1 and SD2) and address lines VA16 ... VA23 on the VME bus.

---

* The term VME stands for Versa Module Eurocard.

On-board Memory and Pulse Generation

The on-board memory consists of four static RAM's (MS6264A, chips RAM0 ... RAM3) with a response time of 20 ns. The addressing is accomplished with four counters (ACT161, chips CNT0 ... CNT3), which are preloaded with the address and enabled with a single pulse CNT_UP transmitted from the PLD via multiplexer U39 into the clock input of the counters.

Test-pattern bits have to be generated every 48 ns, where an *ascending* flank is required within that time interval. This means that the static level of the memory output has to be transformed into a pulse, which is accomplished by gating the data bits with CNT_CLK2 in eight logical-AND chips U58 ... U65. The resulting pulses have a length of 24 ns. This procedure is only active during a test-pattern run, which is controlled via FREE_RUN and chip U66.

Status Displays

The status of the boards is displayed with three LED's on the front panel. LD1 shows on two LED's the level of the signals $\overline{\text{BOARD_RESET}}$ and DP9 (which is active if the XILINX is loaded). LD3 is on when all voltage levels are at their nominal values.

External Connectors

Two LEMO connectors on the front panel are needed for self-testing the trigger. CLK serves as input for the synchronized release of CNT_RESET initiated by the master board and distributed by the two clock boards (*cf.* the detailed description of test-pattern runs in section A1.3). SYNC provides a NIM output (with chips U48 and U49 and a collection of resistors and diodes) for D31 from RAM0. This serves as an external L1KEEP and invokes the readout of the trigger. As no inversion on the board is provided, this signal has to be *programmed* in negative logic.

A1.2 Controlling the Receivers

A total of 30 receivers are distributed in two crates with 15 boards each. Access to the receiver boards is handled by the custom VME interface. The following operations are implemented in the control program *DcTrig* running on a Macintosh computer:

- Writing to and reading from a control register, which actually controls the operation of the receiver board.
- Setting and reading a delay value for the counter clock.
- Loading a threshold voltage into the DAC's.
- Masking wires with HIGH or LOW and enabling or disabling the masks wire by wire.
- Writing to and reading from the main memory.

On-board Addresses

The distinction between the various operations is done by different on-board addresses. The overall address used to communicate with a specific receiver is obtained from its crate number in the VMV bus, the board address within the crate, and finally the on-board address according to the following scheme*.

$$\text{address} = \text{V X YY ZZZZ}$$

where V = slot number of the MACVEE board inside the Mac (*0x*C);
X = crate number within the VMV bus (2 or 3 for receiver crates);
YY = board address within the receiver crate (*0x*C0 ... *0x*DD);
ZZZZ = on-board address (*0x*0 ... *0x*8052).

The following on-board addresses are recognized by the VME interface.

Table 6: On-board addresses of the receivers.

Address	Functionality	Address	Functionality
*0x*0 ... *0x* 7FFE	Main memory		
*0x*8000	Control register	*0x*8040	Low 16 bit mask
*0x*8010	Counter clock delay	*0x*8042	Low mask enabler
*0x*8012	DAC 1 voltage offset	*0x*8050	High 16 bit mask
*0x*8020	DAC 2 voltage offset	*0x*8052	High mask enabler
*0x*8022	DAC 3 voltage offset		
*0x*8030	DAC 4 voltage offset		
*0x*8032	DAC 5 voltage offset		

All addresses given in terms of four digits represent on-board addresses.

Memory

The on-board memory is 32 bits wide as needed for the 29 data lines. VME access is only 16 bits wide, and therefore two cycles are required to read or write an entire *word*. RAM0 and RAM1 contain the high part (bits 16 ... 31) and are addressed with $4 \cdot x$, while RAM2 and RAM3 hold the low part (bits 0 ... 15) and correspond to addresses $4 \cdot x + 2$. Only even addresses are possible. Two examples might help.

$*0x$C2'C0'0000 = 1 → Bit 1 on RAM0 and data line 18 of receiver *0x*C0 in crate 2.
$*0x$C2'C0'0006 = 1 → Bit 1 on RAM2 and data line 1 of the same receiver, but with 48 ns delay relative to the first example

* Numbers preceded by '*0x*' are hexadecimal.

Registers

The following on-board registers are available.

- The *control register* at *0x*8000 is used to control the boards and is described in detail below.
- The *delay for the counter clock* is set by writing a specific value into *0x*8010. The delay line is only guaranteed to be monotone, but not linear. A typical delay value of 0.5 ns is achieved by one bit, i.e. writing *0x*10 into *0x*8010 results in a delay of ~ 8 ns.
- Setting the *discriminator thresholds* is done by loading a specific value into the corresponding registers *0x*8012 ... *0x*8032. A value of 0 corresponds to a threshold of $U \sim -8\,\mathrm{V}$, *0x*800 yields roughly $U \sim 0\,\mathrm{V}$, and $U \sim +8\,\mathrm{V}$ is achieved with *0x*FFF.
- Loading a *mask* is done in two steps. First, a mask is defined with a bit pattern of either '0' or '1' for each data line (addresses *0x*8040 and *0x*8050 masking lines 0 ... 15 and 16 ... 29, respectively). Second, the mask for the relevant channel has to be enabled in *0x*8042 and *0x*8052, again with a bit pattern.

The Control Register

The control register at address *0x*8000 has 16 bits, out of which 10 are used and described in table 7.

Table 7: Control register. Entries marked with a * are write-only, whereas ** indicates a read-only register bit.

Bit	Function	Signal name	
0	Board reset	BRD_RST	*
1	Counter reset	CNT_RST	*
2	FPGA reset	XIL_RST	*
3	Mask reset	MSK_RST	*
4	Data direction	DIR_DATA	
5	Clock delay	CLK_DEL	
6	Free run	FREERUN	
7	Mode 3	MODE3	
8	$\overline{\text{Board_Reset}}$		**
9	DP9		**

All *reset signals* are generated from the corresponding bits latched into chip U33. Apart from the FPGA reset, all signals are set and cleared via the VME bus. XIL_RST is set via VME, but cleared on-board after 8 μs. This time delay is required for a

successful loading of the PROM into the FPGA. DIR_DATA controls the data flow through chips U9 and U10 and is set automatically with FREERUN. This signal is used to disable input from CJC and enables the data flow from the memories into the synchronization ("test-pattern run"). CLK_DEL does not enter the PLD but is routed directly to the multiplexer U39, where a selection between three different clocks (pulses) for memory I/O is done. Doing a test-pattern run with a delayed clock requires both bits to be set, i.e. *0x*60 should be loaded into the control register. Mode3 controls the Output Enable of the differential output drivers U17 ... U24.

A1.3 Test-Pattern Runs and Self-Tests

Testing the DC-$r\phi$ trigger is a non-trivial task, as most of the trigger logic is hidden inside the FPGA's on the SRL1 boards. It is possible to determine the single track efficiency with off-line monitoring, but that gives only a crude impression of the detailed hardware performance. This is achieved with *test-pattern runs* and *self-tests*.

Test-Pattern Runs

A test-pattern consists of the bit pattern of a single mask and is loaded into the memories of the appropriate receivers. The position of every bit in a word corresponds to a specific layer in either CJC1 or CJC2. The time structure of a mask is preserved by storing all delayed bits into memory locations with suitable address offsets relative to the prompt (first) bit.

The simultaneous starting of all CNT_CLK's on all relevant receivers is non-trivial, because the PLL's clock is of a fixed frequency only after it has locked into the feedback loop. The locking process is not identical for different boards, which prevents a start of all counters by means of switching off and on the master clock on the 'Delay board'. Therefore the following procedure has to be adopted (*cf.* figure 46).

A value of *0x*62 is loaded into the control registers of all receivers: CNT_RESET is activated on all receivers, thus disabling the counters. Furthermore, the boards are then in FREERUN mode with the delayed counter clock active. One master receiver (#1, determined by the jumper T11-T12 next to the PLD) is subsequently addressed and *0x*60 is written into its control register, releasing its CNT_RESET. This signal is broadcast to all other boards via the two 'Clock boards' and 29 LEMO cables (linking the CLK input of the receivers to one of the output connectors of the Clock boards). The master's CLK LEMO connector has to be linked to the IN connectors on both clock cards. Synchronization of the CNT_RESET signal on all boards is ensured by passing it through a D-type flip-flop (chip U51), where it is clocked by the 10.4 MHz HERA clock. Stopping a test-pattern run is done in an analogous way by activating CNT_RESET on the master.

Self-Test of the Trigger

masks on all SRL1 boards, test-patterns are concatenated and down-loaded sequentially into all 30 receiver boards. The resulting procedure is termed *self-test*. Apart from the basic cabling used for a test-pattern run, one additional cable has to connect

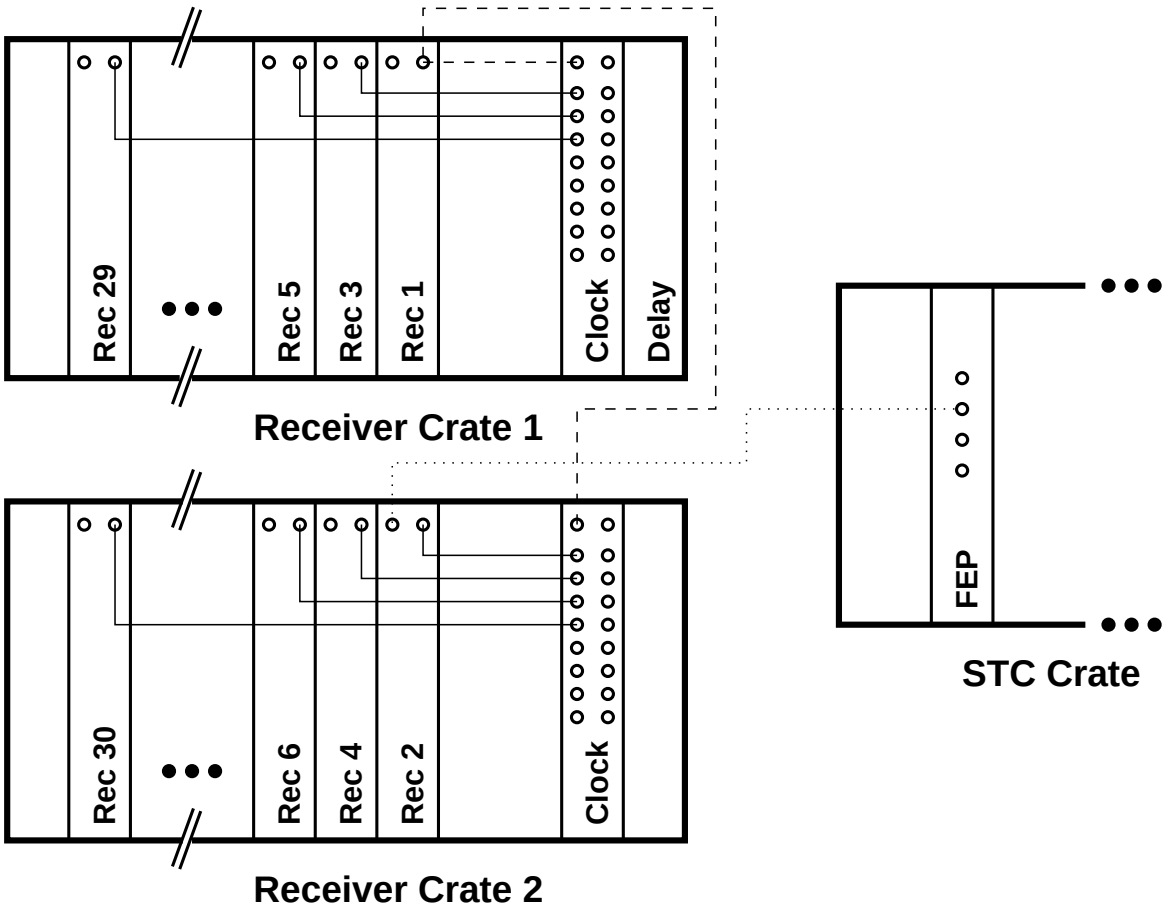

Figure 46: Overview of the cabling needed for a self-test. The solid lines connect the CLK input of the receiver boards to the output connectors on the two clock boards. The dashed lines connect the CLK output of the master receiver to the input connector of the two clock boards. The dotted line connects the SYNC output of receiver #2 to the SYNC EVT input connector of the FEP in the STC crate.

the 'SYNC' output of receiver #2 with the input 'SYNC EVT' of the 'Fast card' in the STC crate. The memory contents of receiver #2 are filled in such a way that data line D31 will generate a TTL pulse of 48 ns width in negative logic, which is translated into NIM levels. This pulse is used as an external L1KEEP signal for the front-end processor FIC, initiating a local readout of the trigger into a log-file onto the hard-disk of Macintosh.

Figure 47 shows the efficiency of the trigger as a function of the mask number (averaged over all receiver boards) for both standard masks (a) and T0-validated masks (b). The average efficiency is $<\epsilon>_{TA}= 97.8\%$ in the first case and $<\epsilon>_{T0}= 92.7\%$ for the validated masks.

Figure 48 shows the performance for each mask and for every receiver board.

Inefficient masks show up as white spots in figure 48 and have the following reasons:

- The holes around masks 100 and 115 are due to wrongly connected circuit lines to a Xilinx FPGA on the SRL1 boards.
- The regular pattern visible at mask 295 stems from timing problems within the trigger logic implementation in the Xilinx FPGA's.
- Isolated inefficient masks have their origin in broken chips in the signal path between the synchronization and the final trigger logic.
- The reason for the large efficiency loss in the T0-validated masks in the mask range 25 ... 40 is due to a faulty VME-connection in the VIC in receiver crate #2. It has been fixed in the meantime.

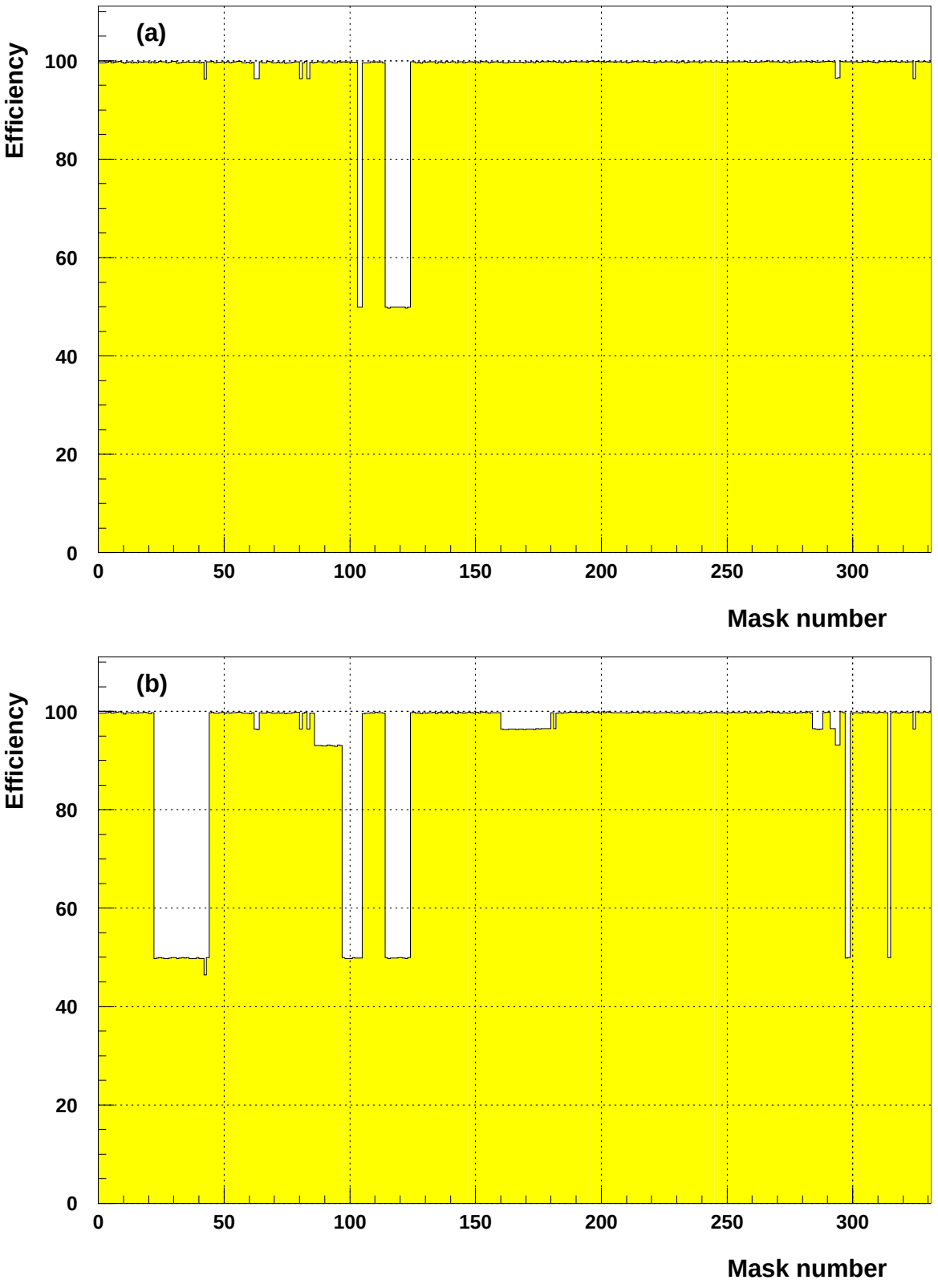

Figure 47: Average efficiency of TA (a) and T0-validated (b) masks in the nominal bunch-crossing. The efficiency is obtained by averaging over all receiver boards.

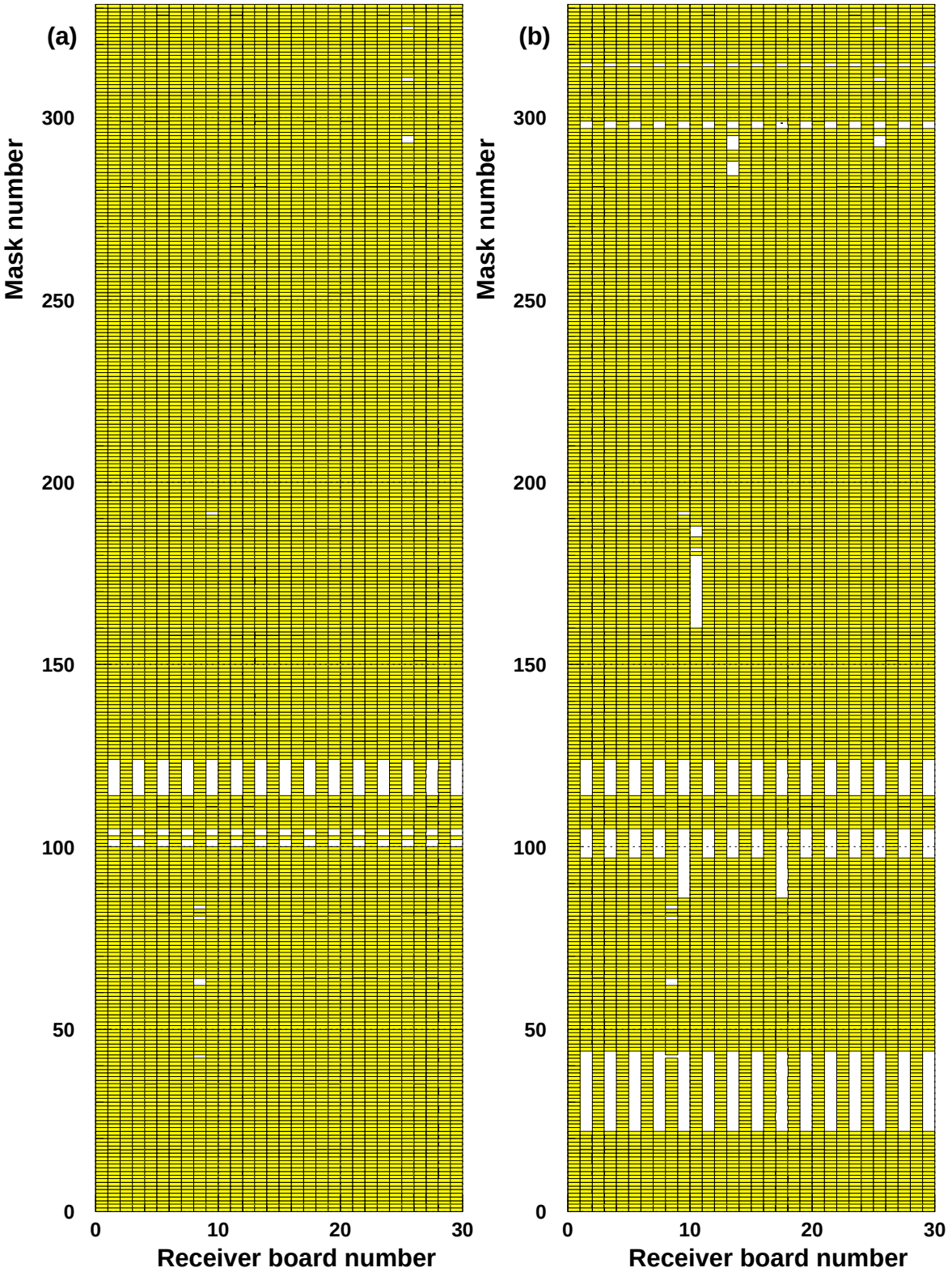

Figure 48: Efficiency of TA (a) and T0-validated (b) masks in the nominal bunch-crossing for all receiver boards. Fully operational masks are displayed as shaded rectangles, defective masks show up as white holes.

Bibliography

Aleph Collaboration (1994), Nucl. Instrum. Meth. **A346**, 461.

Andersson, B., *et al.* (1983), Phys. Rep. **97**, 31.

ARGUS Collaboration (1991), Z. Phys. **C52**, 353.

Bengtsson, H.-U., and T. Söstrand (1987), Computer Physics Commun. **46**, 43.

Bernet, R. (1995), *Production of $D^{*\pm}$ Mesons Measured with the H1 Detector at HERA*, Ph. D. thesis No. 11041, ETH Zurich.

Brun, R., *et al.* (1987), GEANT3, CERN DD/EE/84-1.

Budnev, V. M., *et al.* (1975), Phys. Rep. **C15**, 181.

Burke, S., *et al.* (1995), DESY 95-132.

CDF Collaboration (1993), Phys. Rev. Lett. **71**, 500.

Charchula, K., G. A. Schuler, and H. Spiesberger (1994), CERN-TH 7133/94.

Collins, J. C., D. E. Soper, and G. Sterman (1986), Nucl. Phys. **B263**, 37.

CTEQ Collaboration (1995), Rev. Mod. Phys. **67**, 157.

DØ Collaboration (1995), Phys. Rev. Lett., **74**, 3548.

DØ Collaboration (1997), *Determination of the b-Quark Production Cross Section in $p\overline{p}$ Collisions at 630 GeV*, Abstract submitted to the *XVIII International Symposium on Lepton Photon Interactions*, July 28 – August 1, 1997, Hamburg, Germany.

DELPHI Collaboration (1997), *$\pi^{\pm}$, $K^{\pm}$, p and $\overline{p}$ production in $Z^0 \to b\overline{b}$ and $Z^0 \to u\overline{u}d\overline{d}s\overline{s}$*, Contributed paper #541 to the *International Europhysics Conference on High Energy Physics*, August 19 – 26, 1997, Jerusalem, Israel.

Eichler, R. A., and Z. Kunszt (1989), Nucl. Phys. **B308**, 791.

Ellis, R. K., *et al.* (1979), Nucl. Phys. **B152**, 285.

Ellis, R. K., and Z. Kunszt (1988), Nucl. Phys. **B303**, 653.

Ellis, R. K., and P. Nason (1989), Nucl. Phys. **B312**, 551.

Fermi, E. (1924), Z. Phys. **29**, 315.

Frixione, S., *et al.* (1994), Phys. Lett. **B348**, 633.

Frixione, S., *et al.* (1994a), Phys. Lett. **B412**, 225.

Grab, C., and G. Tsipolitis (1997), private communication.

H1 Collaboration (1995), Z. Phys. **C69**, 27.

H1 Collaboration (1995a), Z. Phys. **C66**, 529.

H1 Collaboration (1996), Nucl. Phys. **B472**, 32.

H1 Collaboration (1996a), Nucl. Phys. **B480**, 3.

H1 Collaboration (1997), Nucl. Instrum. Meth. **A386**, 310.

Ingelman, G., J. Rathsman, and G. A. Schuler (1996), DESY 96–058.

Isgur, N., *et al.* (1989), Phys. Rev. **D39**, 799.

Isgur, N., and M. B. Wise (1989), Phys. Lett. **B232**, 113.

Itterbeck, H. (1997), *Techniques and Physics of the Central–μ–Trigger System of the H1–Detector at HERA*, Ph. D. thesis, Universität Aachen.

Jacquet, F., and A. Blondel (1979), in *Proceedings of the Study of an ep facility for Europe*, Ed. U. Amaldi, DESY 79/48, 391.

Kander, M. (1998), *Bestimmung des ep-Wirkungsquerschnittes von Beauty-Quarks durch ihren semileptonischen Zerfall in Myonen mit dem H1-Detektor bei HERA.*, Ph. D. thesis, Universität Hamburg.

Kleinwort, C., and U. Krüger (1992), *Iron muon track reconstruction*, H1-software note 92-034.

Korner, J. G., and G. A. Schuler (1988), Z. Phys. **C38**, 511.

L3 Collaboration (1990), Phys. Lett. **B252**, 703.

Marchesini, G., *et al.* (1992), Computer Physics Commun. **67**, 465.

Martin, A. D., R. G. Roberts, and W. J. Stirling (1995), Phys. Lett. **B354**, 155.

Nason, P., S. Dawson, and R. K. Ellis (1988), Nucl. Phys. **B303**, 607.

OPAL Collaboration (1991), Phys. Lett. **B263**, 311.

OPAL Collaboration (1995), Phys. Lett. **B364**, 93.

PDG, Particle Data Group (1996), Phys. Rev. **D54**.

Peterson, C., *et al.* (1983), Phys. Rev. **D27**, 105.

Pollet, P. (1995), *Schematics to the Receiver Boards of the DC-rϕ Trigger*, unpublished.

RSV (1952), *Revised Standard Version* of the translation of the Bible.

Seywert, C. (1996), *Untersuchungen zur Zeitauflösung des DC-rϕ Triggers bei H1*, Diploma thesis, ETH Zurich.

Sjöstrand, T. (1985), Phys. Lett. **157B**, 321.

Sjöstrand, T. (1994), Computer Physics Commun. **82**, 74.

SLD Collaboration (1997), *Production of $\pi^{\pm}$, $K^{\pm}$, K^0, K^{*0}, ϕ, p and Λ^0 in Hadronic Z decays*, contributed paper # 287 to the *International Europhysics Conference on High Energy Physics*, August 19 – 26, 1997, Jerusalem, Israel.

Smith, J., and W. L. van Neerven (1992), Nucl. Phys. **B374**, 36.

UA1 Collaboration (1988), Z. Phys. **C37**, 489.

Weizsäcker, C. F. (1934), Z. Phys. **88**, 612.

West, L. (1996), *Heavy Flavor Working Group Track, Muon and Electron Selection Code*, Version 1.00/12.

Williams, E. J. (1934), Phys. Rev. **45**, 729.

Wirbel, M., *et al.* (1985), Z. Phys. **C29**, 637.

Wolff, T. (1993), *Entwicklung, Bau und erste Ergebnisse eines totzeitfreien Spurfinders als Trigger für das H1-Experiment am HERA Speicherring*, Ph. D. thesis No. 10408, ETH Zurich.

Acknowledgments

It is a pleasure to thank Ralph Eichler for the possibility to do this thesis under his supervision. He provided steady guidance with ample of freedom and never failed to ask the relevant questions. I thoroughly enjoyed my time in his group.

Felicitas Pauss readily accepted to be co-examiner: Thank you!

I profited a lot from the experience of Georgios Tsipolitis in matters of analysis. Christoph Grab always had an open ear and good advice for all kind of problems.

The recitation sessions of Marco Arpagaus and Christoph Grab had a significant responsibility for seriously getting into particle physics at all.

Patrick Pollet and the entire team of the electronics lab patiently helped and bore me during the design and testing of the receiver boards of the DC-$r\phi$ trigger. Roland Bernet kindly introduced me to the simulation and hardware of the DC-$r\phi$ trigger while finishing *his* thesis. Hans-Christian Kästli took over the responsibility for the trigger and helped to get the test-pattern runs running.

The entire Zurich-group (at DESY), David Müller, Katharina Müller, Stefano Passaggio, Stefan Hengstmann, Monika Wagener, Daniel Pitzl, and Johannes Gassner, kept creativity on a high level with regular coffee-breaks and sharing interesting evenings.

Martin zur Nedden shared inspiring evenings with me while listening to old and *new* music. Brilliant days were spent with Hubert Niggli on hard rock. Bruno Grünenfelder deserves a special thanks for innumerable days on steep rock, ice and snow.

An indispensable reference frame outside of high-energy physics was provided by Dani, Housi, Roger, Stefan, and Thomas in Zurich and by Tini, Torsten, Martin, and the rest of the KJE Bahrenfeld in Hamburg. Karin and Dietmar were never far away on the other side of the Elbe.

A big hug goes to my dad for reading the entire thesis, my mom for all her sweet support in times of pressure, and my brother Thomas and his family for the moral assistance in times of troubles.

My final acknowledgments are best expressed in the words of David,

Blessed be the LORD*! For he has heard the voice of my supplications.*
The LORD *is my strength and my shield; in him my heart trusts;*
so I am helped, and my heart exults, and with my song I give thanks to him.
(Psalms 28:6-7, RSV)

Curriculum Vitae

Personal Data

Name	Urs Langenegger
Date of Birth	May 14, 1968
Place of Birth	Recklinghausen (Germany)
Nationality	Swiss (from Bühler, Appenzell Ausserrhoden)

Education

1974 – 1976	Primary School in Addis Abeba (Ethiopia)
1976 – 1979	Primary School in Uttwil (Switzerland)
1979 – 1981	Secondary School in Accra (Ghana)
1981 – 1983	High School in Washington, D.C. (USA)
1983 – 1985	Gymnasium Untere Waid in Mörschwil (Switzerland)
1985 – 1987	Gymnasium Friedberg in Gossau (Switzerland)
1987	Kantonale Matura Typus B, Gossau
1987 – 1989	On service in the Swiss Army
1989 – 1994	Study of physics at the Swiss Federal Institute of Technology Zurich in Zürich (Switzerland)
October 1994	Diploma in Experimental Physics at the Swiss Federal Institute of Technology Zurich. ("Multiplicity Distributions of Charged Particles in Photon Proton Scattering at HERA")
1994 – 1998	Graduate education in Experimental High Energy Physics at the Swiss Federal Institute of Technology Zurich.